



RETURNING MATERIALS:

Place in book drop to
remove this checkout from
your record. FINES will
be charged if book is
returned after the date
stamped below.

<p>SEP 27 '88 K 256 A 271</p>		
---------------------------------------	--	--

DEVELOPMENT OF A MICROWAVE ION
AND PLASMA SOURCE IMMERSSED IN A MULTICUSP
ELECTRON CYCLOTRON RESONANT
MAGNETIC FIELD

By

Mahmoud Dahimene

A DISSERTATION

Submitted to
Michigan State University
in partial fulfillment of the requirements
for the degree of

DOCTOR OF PHILOSOPHY

Department of Electrical Engineering and System Science

1987

ABSTRACT

DEVELOPMENT OF A MICROWAVE ION AND PLASMA SOURCE IMMERSSED IN A MULTICUSP ELECTRON CYCLOTRON RESONANT MAGNETIC FIELD

By

Mahmoud Dahimene

This dissertation presents the experimental development and test of an electrodeless microwave (2.45 GHz) generated plasma and ion source in a discharge pressure range of 6×10^{-4} - 5×10^{-1} Torr and relatively low power (80 - 350 W CW). Also presented is a semi-empirical model applicable to low pressure microwave discharges with no static magnetic field. Initial experiments studied the properties of variable diffusion length (0.43 - 1.22 cm) disk shaped discharges generated and maintained in a cylindrical microwave resonant cavity applicator for argon and oxygen gases without static magnetic field. These discharges were characterized by measuring plasma densities and electron temperatures using a Langmuir double probe for different experimental conditions. The measured plasma densities and electron temperatures ranged from 8×10^{10} to 5×10^{11} cm^{-3} and 2×10^4 to 8×10^4 $^{\circ}\text{K}$ respectively. The ion temperature was less than 500 $^{\circ}\text{K}$. Ion beams were extracted from these discharges using single and double grids. Argon ion beam currents densities were measured to be 3.0 mA/cm^2 for the single grid and 5.8 mA/cm^2 for the double grids with a maximum extraction voltage of 1.7 KV. This applicator was then retrofitted with magnets to study the effect of a multicusp static magnetic field. Using this concept, a new cylindrical microwave applicator was designed and tested. In this new

applicator, seventeen pairs of samarium-cobalt magnets generated a multicusp static magnetic field surrounding the discharge chamber and produced an electron cyclotron resonant (ECR) surface (875 G) inside the discharge region. Experimental tests of this (ECR) applicator showed substantial improvements of the discharge and ion beam stability at discharge pressures as low as 6×10^{-4} Torr. An argon ion beam current density of 6 mA/cm^2 was obtained using the double grids at a discharge pressure of 1×10^{-3} Torr corresponding to an ion mass utilization of 34%. The model developed in this dissertation is based on the fluid equations and ambipolar diffusion theory. Despite its simplicity, it was found that the model is in good agreement with the experimental measurements. It is expected that the results of this investigation can be used to develop more efficient microwave ion and plasma sources.

ACKNOWLEDGEMENTS

The author is thankful for the guidance received from Dr. Jes Asmussen throughout this investigation. Additional thanks are given to Mr. Leonard Mahoney for his valuable contribution in the experimental research, to Mr. Ben Boyle for his help in the magnetic field mapping and to Mr. Jeff Hopwood for writing the Langmuir data processing computer program. Special thanks to Dr. Stanley Whitehair for his friendship, encouragement and help in completing this dissertation.

This research was supported in part by grants from the National Science Foundation and Optics Electronics.

TABLE OF CONTENTS

LIST OF FIGURES.....	viii
LIST OF TABLES.....	xi
CHAPTER I INTRODUCTION	
1.1 <u>INTRODUCTION</u>	1
1.2 <u>RESEARCH</u>	3
1.3 <u>THESIS OBJECTIVES</u>	4
1.4 <u>THESIS OUTLINE</u>	4
CHAPTER II REVIEW OF PLASMA AND ION SOURCES	
2.1 <u>INTRODUCTION</u>	6
2.2 <u>DC PLASMA AND ION SOURCES</u>	7
2.2.1 <u>AXIAL FIELD</u>	8
2.2.2 <u>MULTIPOLE FIELD</u>	11
2.2.3 <u>RADIAL FIELD</u>	13
2.3 <u>RF DISCHARGES</u>	15
2.3.1 <u>CAPACITIVELY COUPLED DISCHARGES</u>	16
2.3.1.1 <u>DESCRIPTION</u>	16
2.3.1.2 <u>SELF BIAS</u>	18
2.3.1.3 <u>PLASMA PARAMETERS</u>	19
2.3.1.4 <u>RF PLASMA RESONANCE</u>	21
2.3.1.5 <u>EFFICIENCY</u>	22
2.3.2 <u>INDUCTIVELY COUPLED DISCHARGES</u>	23
2.4 <u>MICROWAVE DISCHARGES</u>	26
2.4.1 <u>THE PROPAGATION WAVE APPLICATORS</u> ..	26
2.4.2 <u>RESONANT APPLICATORS</u>	29
2.4.3 <u>ECR SOURCES</u>	30
2.5 <u>ION SOURCE PERFORMANCE EQUATIONS</u>	31
2.6 <u>REVIEW OF RF AND MICROWAVE ION SOURCES</u>	33

CHAPTER III DEVELOPMENT OF A SIMPLE MODEL

3.1	<u>INTRODUCTION</u>	36
3.2	<u>DERIVATION OF THE FLUID EQUATIONS</u>	37
	3.2.1 THE PARTICLES CONSERVATION EQUATION.....	39
	3.2.2 THE MOMENTUM TRANSFER EQUATION.....	43
	3.2.3 THE ENERGY CONSERVATION EQUATION...	46
	3.2.4 MAXWELL'S EQUATIONS.....	47
3.3	<u>SIMPLIFYING ASSUMPTIONS</u>	47
	3.3.1 ASSUMPTIONS.....	48
	3.3.2 PRACTICAL SIMPLIFICATION OF THE BASIC EQUATIONS.....	53
3.4	<u>RF PLASMA MODEL</u>	56
3.5	<u>THE AMBIPOLAR DIFFUSION MODEL FOR A CYLINDRICAL GEOMETRY</u>	59
3.6	<u>POSSIBLE IMPROVEMENT OF THIS MODEL</u>	71

CHAPTER IV EXPERIMENTAL SYSTEMS

4.1	<u>INTRODUCTION</u>	75
4.2	<u>DESCRIPTION OF THE MICROWAVE ION SOURCES</u>	76
	4.2.1 MICROWAVE PLASMA DISK ION SOURCE, APPLICATION I.....	76
	4.2.1.1 THE CAVITY APPLICATOR DESCRIPTION.....	76
	4.2.1.2 APPLICATOR OPERATION.....	79
	4.2.2 APPLICATOR I RETROFITTED WITH A MULTICUSP MAGNETIC FIELD.....	85
	4.2.3 MULTICUSP-MICROWAVE ION SOURCE.....	91
4.3	<u>GENERAL EXPERIMENTAL SYSTEM</u>	98
	4.3.1 VACUUM AND GAS FLOW SYSTEMS.....	98
	4.3.2 MICROWAVE SYSTEM.....	101
	4.3.3 ELECTRON DENSITY AND TEMPERATURE MEASUREMENTS.....	103
	4.3.4 EXTRACTION GRIDS.....	113
	4.3.5 VOLTAGE EXTRACTION SYSTEM.....	120
	4.3.6 FARADAY CUP.....	126

CHAPTER V EXPERIMENTAL MEASUREMENTS

5.1 INTRODUCTION.....130
5.2 APPLICATOR I WITHOUT STATIC FIELD.....131
 5.2.1 EXPERIMENTAL DISCHARGE CONDITIONS..131
 5.2.2 EXPERIMENTAL RESULTS OF ELECTRON
 DENSITY AND ELECTRON TEMPERATURE
 MEASUREMENTS.....132
 5.2.3 ION BEAM EXTRACTION.....149
 5.2.3.1 SINGLE GRID.....149
 5.2.3.2 DOUBLE GRIDS.....154
 5.2.3.3 OXYGEN ION BEAM
 EXTRACTION.....158
5.3 APPLICATOR I RETROFITTED.....161
5.4 ECR APPLICATOR.....165
 5.4.1 PRELIMINARY CALIBRATIONS.....165
 5.4.2 ELECTRON DENSITY AND TEMPERATURE
 MEASUREMENTS.....168
 5.4.3 ION EXTRACTION.....168

CHAPTER VI COMPARISON OF THE EXPERIMENTAL RESULTS
WITH THE THEORETICAL DISCHARGE MODEL

6.1 INTRODUCTION.....177
6.2 MEASURED QUANTITIES.....177
6.3 CALCULATION OF THE DISCHARGE ELECTRIC FIELD.179
6.4 ION MOBILITY.....188
6.5 ELECTRON TEMPERATURE.....189
6.6 ION CURRENT AVAILABLE FOR BEAM EXTRACTION 192

CHAPTER VII SUMMARY AND CONCLUSIONS

7.1 INTRODUCTION.....196
7.2 COMPARISON BETWEEN THE THREE APPLICATORS
TESTED IN THIS THESIS.....197
7.3 COMPARISON OF THE THREE APPLICATORS AND
OTHER RF AND MICROWAVE ION SOURCES.....200
7.4 CONCLUSIONS.....202
7.5 FURTHER RESEARCH.....203

APPENDIX A STATIC MAGNETIC FIELD MAPPING

INTRODUCTION.....205
DESCRIPTION OF THE METHOD.....205

REFERENCES.....209

LIST OF FIGURES

Figure 2.1	DC Ion Source with Axial Magnetic Field.....	9
Figure 2.2	DC Ion Source with Multipole Magnetic Field..	12
Figure 2.3	DC Ion Source with Radial Magnetic Field.....	14
Figure 2.4	Capacitively Coupled RF Plasma Source.....	17
Figure 2.5	Inductively Coupled RF Plasma Source.....	24
Figure 2.6	Surface Wave Microwave Applicator.....	28
Figure 3.1	Discharge Geometry.....	60
Figure 3.2	Superposition of the Electron Distribution and the Ionization Frequency.....	65
Figure 3.3	Linear Approximation of the Ionization Cross Section.....	65
Figure 4.1	Cross Section of Applicator I.....	77
Figure 4.2	Cross Section of Cavity Mode.....	82
Figure 4.3	Three Dimensional View of the Electromagnetic Cavity Resonant Fields for the TE_{211} Mode....	83
Figure 4.4	Cross Section of Applicator I Retrofitted with Rare Earth Magnets.....	88
Figure 4.5	Magnetic Field Lines in Applicator I Retrofitted.....	90
Figure 4.6	Cross Section of ECR Applicator.....	92
Figure 4.7	Photograph of Assembled ECR Applicator.....	93
Figure 4.8	Photograph of the ECR Applicator Disassembled.....	94
Figure 4.9	Radial Magnetic Field Lines in the ECR Applicator.....	96
Figure 4.10	Cross Sectional View Showing the Static Magnetic Field Lines in the ECR Applicator...	97
Figure 4.11	Gas Flow and Vacuum Systems.....	100
Figure 4.12	Microwave System.....	102
Figure 4.13	Langmuir Double Probe System.....	104
Figure 4.14	Langmuir Probe and Electrical Circuit.....	106
Figure 4.15	Typical Langmuir Probe Current-Voltage Characteristics.....	109
Figure 4.16	Single Grid.....	114
Figure 4.17	Double Grid Assembly.....	116
Figure 4.18	Plasma and Ion Sheath Near the Grids Apertures.....	117

Figure 4.19	Double Grids Dimensions and Potential.....	118
Figure 4.20	Electrical Circuit for Ion Beam Extraction.....	121
Figure 4.21	Electron and Ion Currents Involved in Ion Beam Extraction.....	123
Figure 4.22	Cross Sectional View Showing the Double Grid Assembly and the Shielding Metal Screen.....	125
Figure 4.23	Faraday Cup.....	127
Figure 5.1	Electron Density Versus Discharge Pressure...	135
Figure 5.2	Electron Temperature Versus Discharge Pressure for two Disk Sizes.....	136
Figure 5.3	Electron Density Versus Input Power for Three Disk Sizes.....	137
Figure 5.4	Electron Temperature Versus Input Power for Three Disk Sizes.....	138
Figure 5.5	Electron Density Versus Input Power Density for Three Disk Sizes.....	140
Figure 5.6	Electron Temperature Versus Input Power Density for Three Disk Sizes.....	141
Figure 5.7	(a) Cross Sectional View of the Two Double Probes Positions.....	142
Figure 5.7	(b) Top View Showing the Orientation of Both Probes Relative to the Coupling Antenna.....	142
Figure 5.8	Electron density Versus Discharge Pressure in Two Probes Locations.....	144
Figure 5.9	Electron Temperature Versus Discharge Pressure for Two Probes Locations.....	145
Figure 5.10	Electron Density Versus Discharge Pressure for Oxygen Gas.....	147
Figure 5.11	Electron Temperature Versus Discharge Pressure for Oxygen Gas.....	148
Figure 5.12	Ion Beam Current Versus Extraction Voltage for Different Powers.....	150
Figure 5.13	Ion Beam Current Versus Extraction Voltage With the 4.0 cm Disk.....	152
Figure 5.14	Ion Beam Current Versus Extraction Voltage When the Cavity Is Not Perfectly Tuned.....	153
Figure 5.15	Ion Beam Current Versus Extraction Voltage for Different Acceleration Voltages..	156
Figure 5.16	Ion Beam Current Versus Extraction Voltage for Low Gas Flow Rates.....	157
Figure 5.17	Ion Beam Current Versus Extraction Voltage for Oxygen Gas.....	159
Figure 5.18	Ion Beam Current Versus Extraction Voltage for Oxygen at Low Flow Rates.....	160
Figure 5.19	Ion Beam Current Versus Extraction Voltage for Oxygen with the 4.0 cm Disk.....	162

Figure 5.20	Ion Extraction With Applicator I Retrofitted With Only 8 Magnets Surrounding the Discharge.....	164
Figure 5.21	Ion Extraction With Applicator I Retrofitted With 17 Magnets.....	166
Figure 5.22	Electron Density Versus Discharge Pressure For the ECR Applicator.....	169
Figure 5.23	Electron Temperature Versus Discharge Pressure For the ECR Applicator.....	170
Figure 5.24	Ion Extraction With the ECR Applicator Without Magnets.....	171
Figure 5.25	Ion Extraction With the ECR Applicator With All Magnets.....	174
Figure 5.26	Ion Beam Current Versus Gas Flow.....	175
Figure 5.27	Ion Beam Current Versus Power.....	176
Figure 6.1	Calculated Electron-Neutral Effective Collision Frequency Versus Discharge Pressure.....	182
Figure 6.2	Calculated Average Electric Field Versus Discharge Pressure Diffusion Length Product.....	185
Figure 6.3	Calculated $E/p \Delta$ Versus $p \Delta$	186
Figure 6.4	Calculated Average Effective Electric Field.....	187
Figure 6.5	Calculated Ion Mobility.....	190
Figure 6.6	Comparison Between Experimental Measurements and Theoretical Calculations of the Electron Temperature.....	191
Figure 6.7	Comparison Between Experimental Measurements and Theoretical Calculations of Extracted Ion Beam Currents.....	194

LIST OF TABLES

Table 2.1	Comparison of Some RF and Microwave Ion Sources.....	34
Table 4.1	Applicator I Tuning Parameters.....	81
Table 5.1	ECR Applicator Tuning Parameters.....	167
Table 7.1	Comparison of the Three Ion Sources Tested in this Thesis.....	198

CHAPTER I

INTRODUCTION

1.1 INTRODUCTION

This dissertation describes the experimental development and test of a low pressure microwave plasma source. The research, which was primarily experimental, developed special microwave applicators for the production of low pressure (<0.1 Torr) microwave discharges. Recent parallel research efforts have demonstrated or are investigating the potential of these low pressure microwave discharges in a number of applications. Some of these are microwave ion sources^{1,2,3,4} for spacecraft propulsion and materials processing, low pressure, low temperature plasma assisted oxide growth⁵, microwave plasma etching⁶ and microwave plasma thin film deposition. Each of these applications makes use of a low pressure cylindrical microwave discharge which is operated either without or with an applied static magnetic field.

Fundamental to the development of these applications is the experimental development of efficient low pressure microwave plasma applicators and the development of a theoretical knowledge of the low pressure microwave

discharges. This thesis concerns itself with these issues by first experimentally studying the microwave discharge behavior of three applicator configurations. Knowledge and understanding of the microwave discharge is obtained by measuring the electron density and electron temperature with double Langmuir probes over a wide range of experimental conditions. Ion beam extraction is also experimentally studied using two different grid sets. Finally a simple, approximate, theoretical, ambipolar diffusion model of the discharge is also developed to aid in the understanding of the experimental discharge behavior.

Initial experiments studied the properties of a discharge generated in a cylindrical microwave resonant cavity without static magnetic field. The same microwave applicator is then retrofitted with small rare earth magnets to determine experimentally the effect of a multicusp magnetic field on the microwave generated discharge. Further experiments deal with the development and testing of a new cylindrical microwave applicator designed to operate either with or without a multicusp magnetic field. In this new applicator, rare earth magnets are located outside the cylindrical excitation volume occupied by the resonant electromagnetic fields. The location of these rare earth magnets produces a multicusp, electron cyclotron resonant (ECR) static magnetic field within the discharge zone which reduces the charged particle diffusion to the walls, and

facilitates operation at low discharge pressures by creating ECR zones.

The theoretical model, which is based on the fluid equations for electron, ion and neutral gases makes a number of simplifying assumptions. These assumptions make an otherwise complicated problem solvable. It is not expected that this model will describe the experimental behavior in exact detail. However, under the simplifying assumptions, the model predicts the values of some discharge parameters such as electron temperature, average effective electric field in the discharge and ion current available for extraction when the controllable parameters such as the gas type, the gas flow, the environmental pressure and the input microwave power are known.

This thesis summarizes the experimental research and development that lead to a successful demonstration of a low pressure microwave ion source. Some of this work has already been published in scientific publications^{4,7} and has been presented at international scientific conferences^{8,9,10}.

1.2 RESEARCH

The research described in this thesis was carried out by the author over a period of four years from 1983 to 1987 in Michigan State University under the direction of

Dr. Jes Asmussen. The work described in this thesis builds on previous research carried out by J. Root³, Dr. Fredericks¹¹, Dr. Mallavarpu¹², Dr. Rogers¹³ and Dr. Whitehair¹⁴.

1.3 THESIS OBJECTIVES

The objectives of this thesis are divided into three parts. The first was to develop and test a microwave plasma applicator which was able to generate a stable discharge and was able to allow ion beam extraction at very low pressures and gas flow rates. The second objective was to experimentally characterize a low pressure microwave plasma and ion source by measuring electron density and electron temperature over a wide range of discharge conditions. The third objective was to generate a simple theory that would predict the macroscopic properties of a disk shaped microwave plasma. These properties include the ion current available for extraction from the discharge.

1.4 THESIS OUTLINE

This dissertation is organized as follows. Chapter II presents a background and review of the basic concepts of different plasma and ion sources. A brief review of the

Dr. Jes Asmussen. The work described in this thesis builds on previous research carried out by J. Root³, Dr. Fredericks¹¹, Dr. Mallavarpu¹², Dr. Rogers¹³ and Dr. Whitehair¹⁴.

1.3 THESIS OBJECTIVES

The objectives of this thesis are divided into three parts. The first was to develop and test a microwave plasma applicator which was able to generate a stable discharge and was able to allow ion beam extraction at very low pressures and gas flow rates. The second objective was to experimentally characterize a low pressure microwave plasma and ion source by measuring electron density and electron temperature over a wide range of discharge conditions. The third objective was to generate a simple theory that would predict the macroscopic properties of a disk shaped microwave plasma. These properties include the ion current available for extraction from the discharge.

1.4 THESIS OUTLINE

This dissertation is organized as follows. Chapter II presents a background and review of the basic concepts of different plasma and ion sources. A brief review of the

performance of some operating RF and microwave ion sources is presented. Chapter III presents a simple model derived from the fluid equations applicable to a microwave plasma without static magnetic field. The fluid equations are separated into AC and DC parts. The AC part is used to calculate expressions for the plasma electric conductivity (or equivalent complex dielectric constant), the power absorbed by the discharge and the average effective electric field in the discharge. The DC part, along with the ambipolar diffusion assumption, provides expressions for the ion density distribution in the discharge, the electron temperature versus discharge pressure and discharge chamber dimensions, and finally the total ion current available for extraction. Chapter IV describes the basic experimental setup and methods used to conduct the experiments and measure data. Chapter V presents the measured plasma density and ion beam currents obtained with three different microwave applicators. Chapter VI correlates the measured data to the predictions of the model developed in Chapter III and Chapter VII presents a summary of the experimental results and recommendations for further research.

CHAPTER II

REVIEW OF PLASMA AND ION SOURCES

2.1 INTRODUCTION

The basic concepts of many different plasma and ion sources are reviewed in this chapter. The primary emphasis of this review concerns low pressure ion sources and their associated discharge configurations. Section 2.2 contains a classification of DC plasma and ion sources according to their static magnetic field pattern. Section 2.3 reviews the concepts of two kinds of RF plasma sources. These sources are based on two different methods by which the RF electrical power is transferred to the discharge. These are the capacitively coupled discharges and the inductively coupled discharges. The first type of discharge is described in more detail since these discharges are more often operated at lower gas pressures. In Section 2.4 a brief overview of different microwave plasma applicators is presented. A more complete description of a resonant microwave applicator will be presented in the following chapters. Finally the last Section 2.6 reviews and compares the performances of some RF and microwave ion sources. This

comparison is based on figures of merit described in Section 2.5.

2.2 DC PLASMA AND ION SOURCES.

The classification of some plasma and ion sources as DC is mainly due to the existence of other sources in which the discharge is activated with an electromagnetic field, such as RF or microwave. DC ion sources are presently used in a variety of research and production applications.

The basic principle shared by all direct-current sources is fairly simple, it involves the ionization of a low pressure gas, or a mixture of gases, from electron bombardment.

The electrons responsible for the impact ionization, usually called primary electrons, are emitted from a heated filament. This filament is biased negatively with respect to the discharge chamber walls, which have, usually a cylindrical geometry. The potential between the filament, or cathode and the walls is used to accelerate the primary electrons, until they reach the required ionizing energies. These ion sources are usually operated at low gas pressures, where the mean free path for electron impact ionization is larger than the chamber dimensions. To prevent the rapid escape of these electrons to the anode, a static magnetic field is applied to the discharge chamber. Since there are many possible ways to apply this magnetic field, DC ion

sources can be classified according to their magnetic field configuration. An extensive review of electrostatic sources is found in Reference¹⁵. A few of the most important broad beam ion source configurations are discussed below.

2.2.1 AXIAL FIELD.

The conventional axial field discharge chamber is probably the simplest one to describe. It was first designed by H. Kaufman¹⁶ in 1961. A cross sectional view of this type of ion source is shown in Figure 2.1. The discharge chamber is almost always cylindrical. The cathode is located near the axis and the anode forms the cylindrical boundary to the discharge region. The magnetic field is oriented approximately parallel to the cylinder axis. The primary electrons emitted from the cathode have energies corresponding approximately to the discharge potential difference, which is also the potential between the cathode and the anode. The discharge is found to have two groups of electrons. The primary electron group with higher energy, and the thermally randomized group with a lower energy. The magnetic field in the discharge chamber is made strong enough to make the electrons follow a helical trajectory centered around the axis of the cylinder. The effect of this field is to lengthen the trajectory of the electrons, allowing them to collide with the neutral particles before

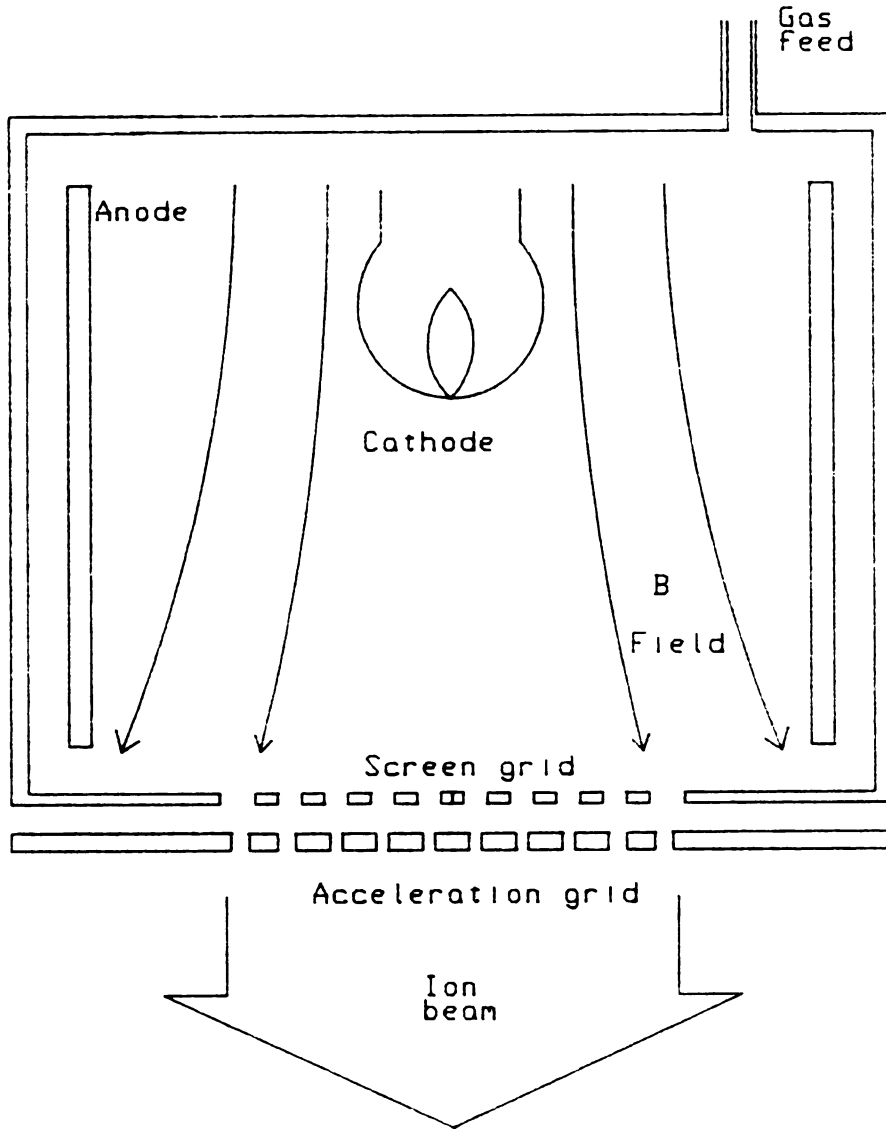


Figure 2.1 DC Ion Source with Axial Magnetic Field

reaching the anode. Usually the gas is fed from one end of the cylinder, and the ions are collected or extracted from the other end. Typically, the magnetic field strength at the downstream end is 60% to 80% of that at the upstream end. The cathode position is not critical, except that it should be near the axis and downstream of the magnetic field maximum.

The theoretical minimum magnetic field for containment of primary electrons in an axial field chamber, corresponds to a value that would make the electron cyclotron radius smaller than the chamber radius by approximately a factor of two. For efficient operation, a magnetic field strength about 50% higher is desirable. Higher fields than that increase the minimum gas pressure or the discharge voltage. Because of their heavy mass, the ions move nearly equally in all directions. This tendency results in a discharge loss per beam ion¹⁵ (in eV/ion) of roughly

$$50 A_p/A_{ex}$$

where A_p is the outside area of the primary electron region defined as the volume where the primary electrons do not suffer collisions. In many cases this region can be approximated by the whole discharge chamber volume. A_{ex} is the projected open area of the ion extraction system. A similar equation can be given for the minimum gas pressure required within the discharge chamber for efficient operation¹⁷. This density, in neutrals/m³, is roughly

$$1.4 \times 10^{17} A_p/V_p$$

where V_p is the primary electron region volume. Both of these equations are for Argon gas, and have about a factor of 2 uncertainty due to various designs.

Axial field discharge chambers are widely used in applications requiring small beam diameters, up to 10 cm. In larger diameters, this design has beam uniformity problems. For a typical axial field chamber with a length equal to its diameter and a 58% open screen extraction grid, the discharge loss is about 300-800 eV/ion. The minimum operating pressure is in the 10^{-4} Torr range.

2.2.2 MULTIPOLE FIELD.

The multipole magnetic field configuration is a more recent development in discharge chambers¹⁸. An example of such an ion source is shown in Figure 2.2. In this configuration, a series of alternating pole magnets are arranged throughout the surface of the discharge chamber. These alternating pole pieces shape the magnetic field in small cusps surrounding the outer surface of the discharge chamber. The anodes are located between the magnetic poles, with the magnetic field above the anodes sufficient to prevent the direct escape of primary electrons to the anodes. The bulk of the discharge chamber volume is nearly field free, allowing a uniform distribution of electrons and

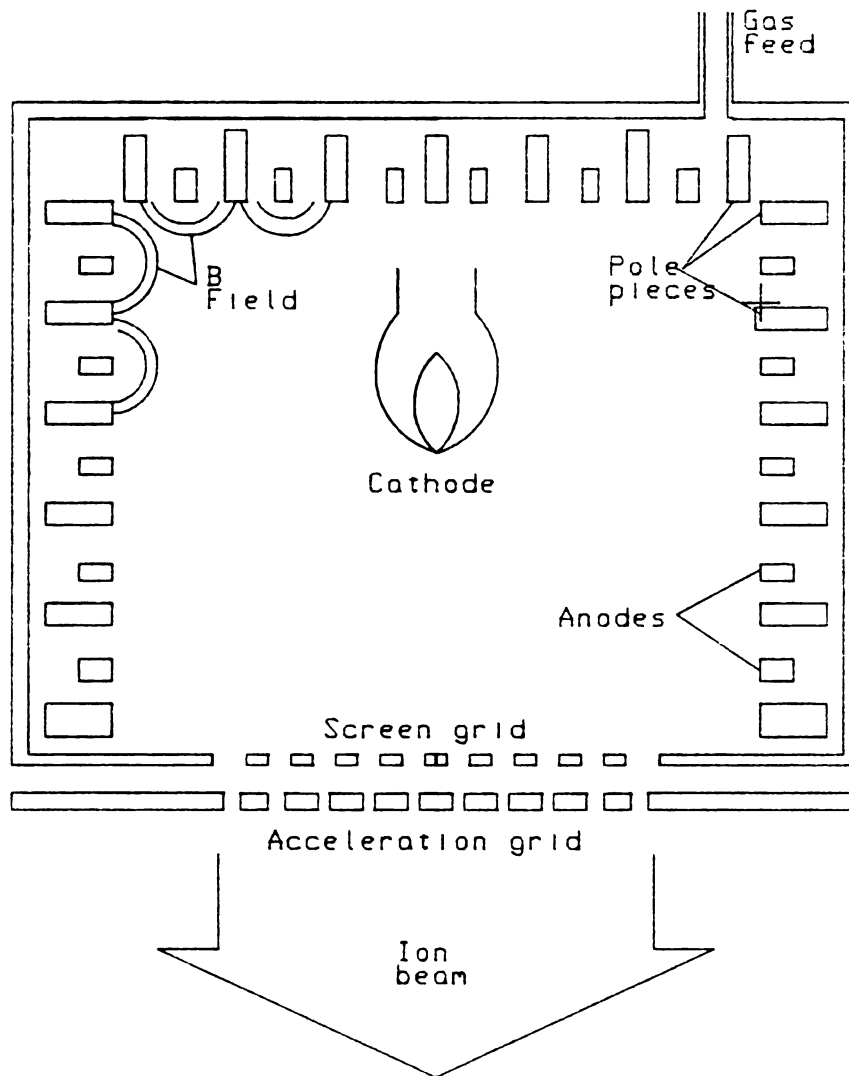


Figure 2.2 DC Ion Source with Multipole Magnetic Field

ions throughout this volume. The primary electron region approximates the volume inclosed by the pole pieces.

The major advantages of the multipole discharges, when used as ion sources are the uniformity of the ion beam profile and the ease of scaling. The beam uniformity is a consequence of the uniformity of primary electron and ion production distributions within the discharge chamber. Typical average-to-peak current density ratios are 0.8-0.9 for a 15 cm diameter ion source. As an example, a 30 cm diameter ion source was built¹⁸ with a 10 cm depth. The discharge losses for this configuration was about 200-400 eV/ion for Argon.

2.2.3 RADIAL FIELD.

For smaller ion sources, the complexity of multipole magnetic fields can be considerably reduced. As shown in Figure 2.3, the magnetic field is given a radial orientation by introducing a pole piece at the center of the chamber, closer to the upstream end. Other magnets are positioned around this center pole and near the discharge chamber cylindrical walls. All these magnets have the same orientation which is opposite to the center one. The magnetic field orientation resulting from this configuration is predominantly radial, with a highest field concentration near the upstream end of the discharge chamber. The

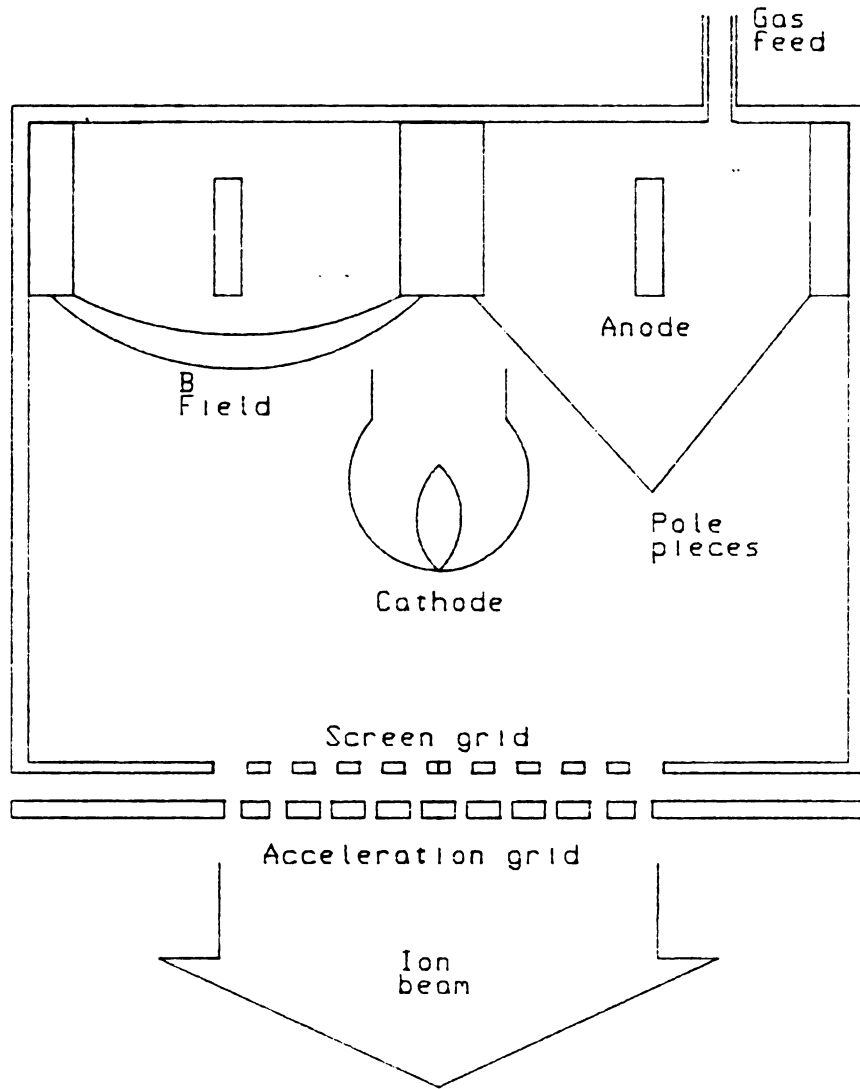


Figure 2.3 DC Ion Source with Radial Magnetic Field

downstream end has a low magnetic field. A circular anode is positioned symmetrically between the center magnet and the wall magnets. The cathode is a heated filament at the center of the discharge chamber.

A radial field ion source was designed and fabricated¹⁹ using this approach. The discharge chamber diameter was 3.8 cm, while the beam diameter was reduced to 3 cm to improve beam uniformity. The overall ion source diameter, including insulating supports for the ion optics and grounded enclosure, was 6.4 cm. The performances of this source were not published.

From all these examples, it is easy to see that a multitude of discharge chambers can be conceived, with some variations of basic principles.

In the same class of electrostatic discharge chambers, one can include some other ion sources²⁰, such as contact ion sources and duoplasmatrons. These types of sources find most of their applications in space propulsion.

2.3 RF DISCHARGES.

RF (radio frequency) discharges can be divided in two main categories, the capacitively coupled and the inductively coupled discharges. The frequencies used in both types can range anywhere between 1 KHz to 1 GHz.

2.3.1 CAPACITIVELY COUPLED DISCHARGES.

2.3.1.1 DESCRIPTION.

The capacitively coupled, or more generally referred to as parallel plates plasma sources, can be thought of as an extension of the positive column discharge in the sense that as for its DC counterpart, the plasma is generated between two electrodes. The basic concept of such sources is fairly simple. A cross section of a typical RF plasma source is shown in Figure 2.4. It consist essentially of a confining chamber in which two electrodes are positioned inside the chamber and externally connected to a high power, high frequency generator. An additional DC biasing circuit for these electrodes is usually used according to the specific applications.

The principal usage of the RF parallel plate plasma sources is reactive etching and sputtering deposition. Both processes are harder to achieve in a DC glow discharge if the samples used are insulators. When an electrically insulating material is covering an electrode in a DC discharge, the surface of the sample exposed to the plasma will charge up to the floating potential. In such a condition the fluxes of electrons and positive ions to the surface become equal. These electrons and ions will recombine at the surface, slowing down any chemical

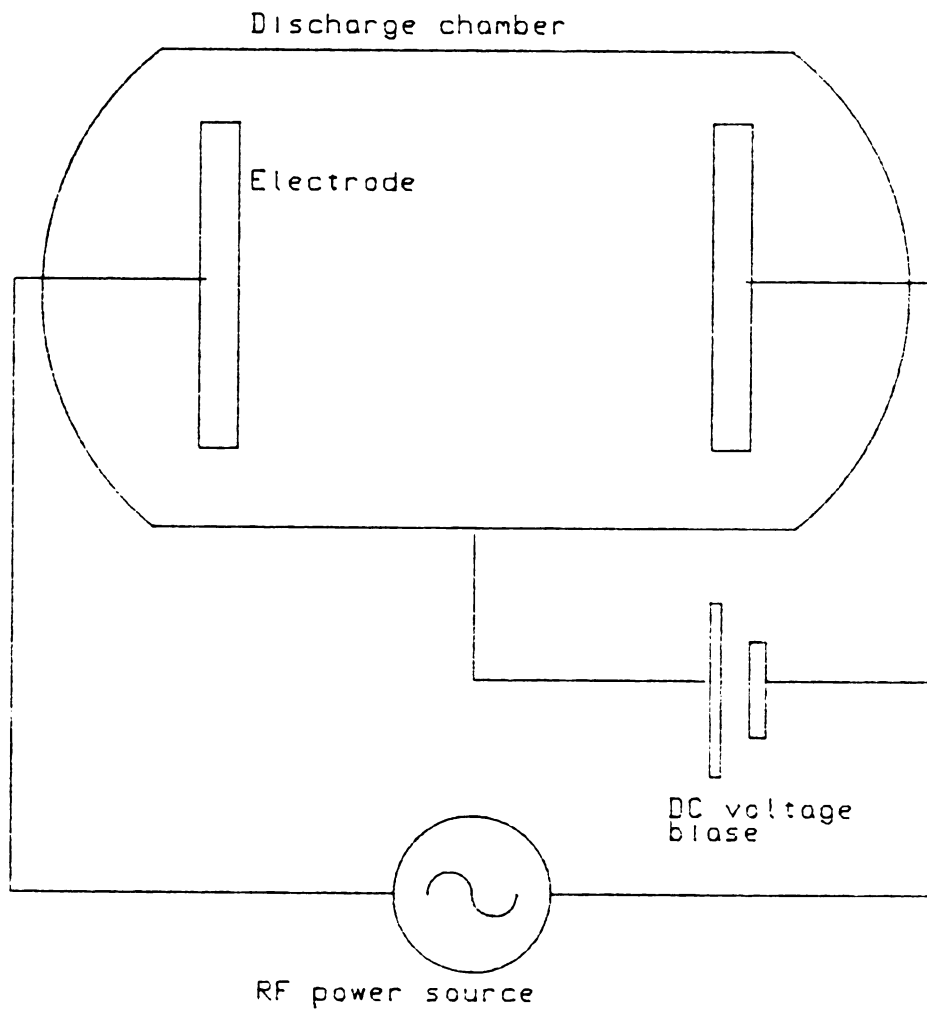


Figure 2.4 Capacitively Coupled RF Plasma Source

reaction. When a glow discharge is initiated, the negatively biased target will begin to be bombarded by positive ions. The insulator will start to charge positively because it loses electrons as the ions are neutralized at the surface. The potential of the insulator surface will then rise progressively to zero, and the discharge will be extinguished as soon as this voltage drops below the discharge sustaining value.

One way to deal with this problem is to use an AC discharge so that the positive charge accumulated during one half cycle will be neutralized during the next half cycle, thus allowing the positive ions to reach the surface almost continuously.

2.3.1.2 SELF BIAS

An important aspect of RF discharges is the self bias of the electrodes. The higher mobility of the electrons allows them to respond to the applied electric field much faster than the positive ions. As a result, a higher concentration of electrons around the electrodes is present at any given time. If the sinusoidal frequency is high enough, the imbalance between electron and ion concentrations will average to a constant negative voltage relative to the plasma. The applied voltage waveform will then be displaced by a negative value, with a mean known as

the DC offset voltage. If a sample is used around the electrodes, it acquires a net self bias voltage favorable for increasing the rate of ion bombardment of the target. From these properties, it is clear that the lower limit of the applied frequency is set by the condition that a quasi-continuous discharge is to be achieved for processing time optimization.

2.3.1.3 PLASMA PARAMETERS.

The interest in RF discharges goes as far back as 1929 when they were discovered. Many investigations exploring the basic phenomena involved in these discharges have been initiated since then. The most significant progress was made in the 1960's.

Harrison²¹ published the first paper where a number of plasma parameters were measured and correlated. In this experiment Argon gas was used in an RF discharge. The results which were summarized by Taillet²² are listed below:

- (a) In the absence of a magnetic field the wall potential is measured to be highly negative with respect to the plasma. Typical values of this voltage vary from 80 V to 120 V when the electronic temperature is approximately 130,000 °K.
- (b) The ionization ratio is very low, the maximum value is about 10^{-4} . The plasma density is approximately $2 \times 10^8 \text{ cm}^{-3}$.

(c) A plasmoid, which is a concentrated discharge floating in the center between the electrodes, appears in the free-fall diffusion regime, or when the mean free path of an ion between elastic collisions with neutral particles is larger than the dimensions of the vessel.

(d) Plasmoids occur only when air is present in the discharge even in very minute quantities, suggesting that oxygen is responsible for this phenomena.

Additional observations from a similar geometry were made by Geller²³.

(a) The electron density decreases with decreasing pressures, after a certain pressure limit it stays constant, it then drops abruptly near zero when the pressure is further decreased.

(b) The three domains of density (described above) correspond to different discharge regimes, diffusion glow, plasmoid and multipacting respectively.

(c) The plasma density is relatively independent of small power changes in the plasmoid regime.

(d) No breakdown is obtained in the plasmoid pressure region with a moderate voltage. Plasmoids are generated by decreasing the pressure once a diffusion discharge has been ignited.

2.3.1.4 RF PLASMA RESONANCE.

Hatch²⁴ went further in distinguishing various cases of diffusion regimes and plasmoids. He also discovered that the RF electric field inside a plasmoid has a 180° phase shift with respect to the applied field. For the diffusion regime no phase reversal was detected. This result was a confirmation of the resonant nature of plasmoids.

When the applied frequency is large compared to the electron neutral collision frequency, most of the RF energy applied to a plasma is stored as a kinetic energy of electron motion. In the regions outside the plasma, the energy is stored in the form of electric energy as a result of the quasi-static field at the electrode surface.

Under such conditions the electron oscillations make the plasma behave as an inductance in the RF circuit. The quasi-static electric field at the electrodes surface makes those regions behave as a capacitance. Resonant conditions are obtained when the inductance equivalent of the plasma is matched to the capacity equivalent to the surrounding medium.

Vandenplas²⁵ presented a comprehensive review of these resonant properties. It is important to note that the RF generator has its own impedance which may vary with power. In order to maintain a resonant discharge when one or more parameters are changing, it is necessary to add an

additional variable impedance to the RF circuit to keep the system in resonance.

2.3.1.5 EFFICIENCY.

RF discharges also have the property of being more efficient than their DC counterpart²⁶ in promoting ionization and sustaining the discharge. As the frequency increases, the minimum operating pressure is observed to fall, reaching a value of less than 1 mtorr at 13 MHz. This seems to indicate that there might be an additional mechanism generating more electrons, not present in DC discharges. This enhanced ionization can be explained as follows. In an AC discharge the electrons cannot move freely in phase with the oscillating electric field due to the elastic collisions with the neutral particles²⁷. If an electron makes an elastic collision at an appropriate time with respect to the phase of the electric field, its velocity could continue to increase until the next collision. The ideal case would be where an electron makes an elastic collision with a neutral particle, reversing its direction at the precise moment when the field changes direction. From this point of view, electrons could progressively build up their energies from a relatively weak electric field, until they reach ionizing energies. This

mechanism seems to be also accepted as the dominant ionization source in microwave discharges.

2.3.2 INDUCTIVELY COUPLED DISCHARGES.

These types of discharges are predominantly high pressure discharges. They are also called induction arcs, electrodeless arcs or thermal induction plasmas. They are sustained by induction from a time varying electromagnetic field. In a descriptive manner, they may be considered as a high frequency transformer whose primary consists of a cylindrical multiturn coil²⁸. The electrically conducting plasma inside the coil forms a secondary, which shorts out the transformer.

The basic configuration of this type of discharge is shown in Figure 2.5. It consists of a multiturn coil. Typically, the diameter of the coil varies anywhere between 5 cm to 30 cm. The plasma is separated from the coil by a tube made of quartz, ceramic or a longitudinally slotted metal that permits penetration of the magnetic field. The working gas, or gas mixture, is fed from one end of the cylindrical structure. The gas pressure is controlled by the combination of the rate of the gas flow and an exhaust system located at the other end of the cylinder. The basic phenomena governing the operation of inductively coupled plasmas are similar to that of the induction heating

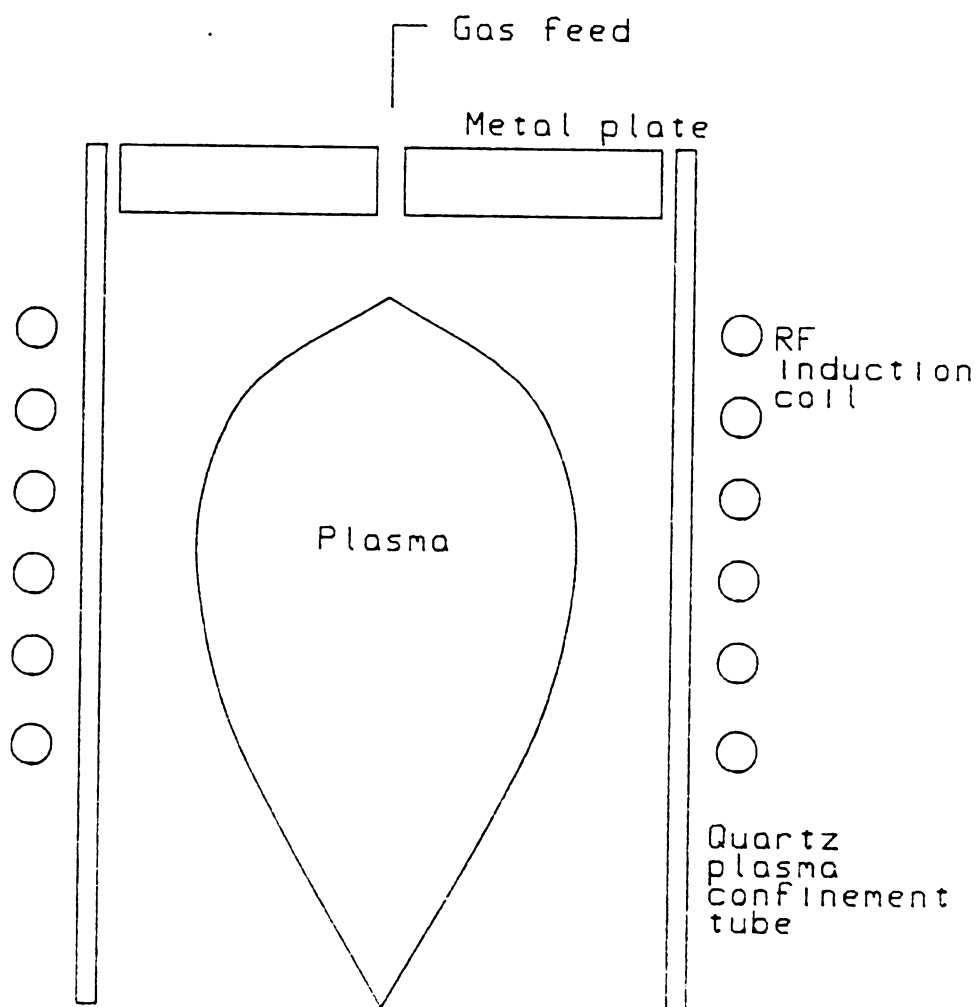


Figure 2.5 Inductively Coupled RF Plasma Source

of metals which have numerous industrial applications. The difference lies in the fact that a plasma has a substantially lower electrical conductivity. This has a direct influence on the optimal frequency, size and power combination necessary to maintain a stable discharge.

In the conventional induction heating theory, the application of an oscillating magnetic field results in the generation of eddy currents in the external cylindrical shell of the load. The thickness of this shell is known as the skin depth

$$\delta = \left(\frac{1}{\pi \mu \sigma f} \right)^{\frac{1}{2}}$$

where f is the applied frequency, σ is the load electrical conductivity and μ is the magnetic permeability which for the case of a plasma is very close to the free space permeability. For example²⁹, for an induction plasma operating with argon at atmospheric pressure with an average temperature of 8,000 °K, $\sigma = 10^3$ mhos/m. The skin depth corresponding to this conductivity is about 8 mm for a frequency of 4 MHz. A reduction of the applied frequency would result in an increase of the skin depth.

The sustaining power of an induction discharge is also dependent on the frequency. For an argon discharge at atmospheric pressure and a frequency of 960 Hz, the minimum sustaining power is close to 1 MW. The corresponding figure for 60 Hz is more than 10 MW.

2.4 MICROWAVE DISCHARGES.

The mechanisms involved in initiating and sustaining a microwave discharge are similar to those of an RF discharge. The difference existing between the two types of discharges lies primarily in the method used to couple the electrical power to the discharge in question.

Unlike RF discharges, microwave discharges are not operated with electrodes. For the case of low pressure microwave discharges there are basically two types of applicators, the propagating wave applicators and the resonant applicators.

Reviews of high pressure microwave discharges can be found in Ref ¹³. This section will only present the basic description of low pressure discharges.

2.4.1 THE PROPAGATION WAVE APPLICATORS.

There are two kinds of propagation wave applicators, the surfatrons and the surfaguides. The principle involved in these types of discharges is related to the propagation of a surface wave. The breakdown and operation of such discharges constitute a complex set of phenomena where the electromagnetic wave creates its own propagation guide³². The propagation of the wave is possible when the electron

density is higher than a cutoff value, which is determined by the excitation frequency. The spatial distribution of the electron density along the axis of the discharge is strongly dependent on the amplitude of the wave and vice-versa. Many surface wave discharges using this principle of operation have been built for different applications Ref 13,30,31.

An example³³ of such a system is shown in Figure 2.6. It consists of a coaxial cavity with a short gap between the center conductor and the front cavity wall. A quartz tube, used to contain the discharge, runs coaxially inside the center conductor. The microwave power is introduced into the cavity by means of a microcoaxial line terminated by a magnetic field excitation loop. In this configuration, the cavity length, the gap length and the loop orientation and position can be adjusted to produce electric fields high enough to breakdown the working gas in the gap region. After breakdown of the gas in the quartz tube, the electric fields in the gap launch traveling surface waves sustaining a plasma column which extends both outside the cavity and inside the center conductor. The dimensions of this system were approximately, 2 cm for the cavity length, and 2 mm for the gap length. The discharge tubes had either 4 mm or 7 mm inside diameters. The cavity outer conductor was 2.5 cm in diameter. The excitation frequency was 2.45 GHz CW. In this experiment, two of these cavities were used at both ends of a quartz tube to create a standing wave. The gas

Coaxial Reentrant Cavity

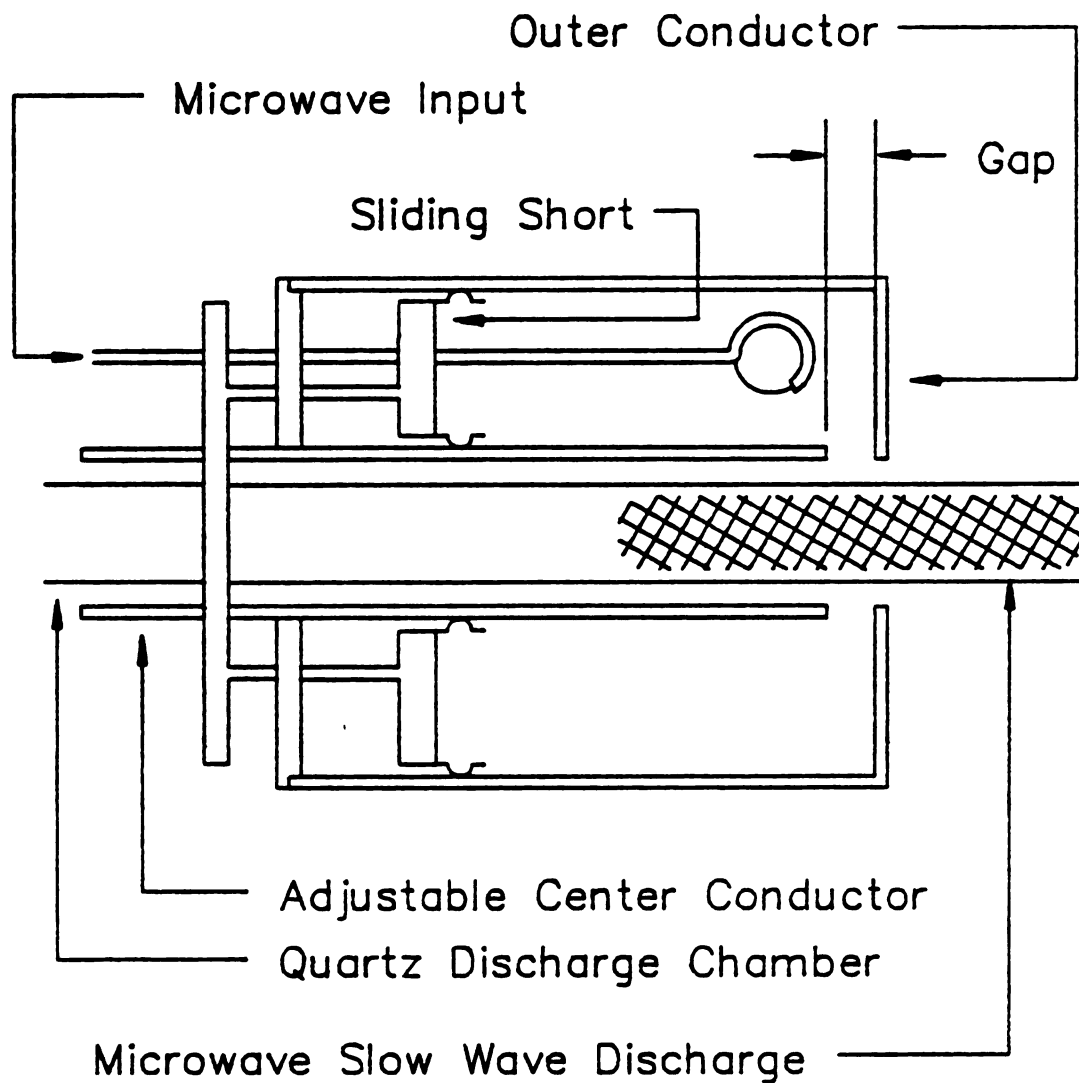


Figure 2.6 Surface Wave Microwave Applicator

used was argon at pressures from 0.05 torr to 330 torr. The electron density measured at the center of this system, was around $2 \times 10^{12} \text{ cm}^{-3}$ and the electron temperature was about 27,000 °K.

2.4.2 RESONANT APPLICATORS.

In this type of applicator the concept of resonant electromagnetic fields inside a cavity is used to couple the microwave energy to the gas discharge. An example of such a system is described in detail by Asmussen³⁴. In this system, the plasma is formed in a quartz tube located on the axis of a cylindrical cavity. The resonant cavity consists of a cylindrical waveguide terminated by a fixed short at one end, and a variable short at the other end. The cavity can be tuned to operate at a specific resonant mode by varying the length of the cylinder via the sliding short. The microwave power is coupled into the cavity-plasma system with a coupling antenna. The antenna can be an extension of the inner conductor of a coaxial cable or a loop. The choice of the geometry of this coupling system depends on the operating resonant mode. The position and orientation of this antenna can be varied to optimize the energy coupling of the system. This system was operated with argon at pressures varying between 1 mtorr to 1 atmosphere.

In some experiments¹³ the quartz tube diameter was varied between 4 mm and 13 mm with the plasma length approximately constant and equal to about 16 cm. The resonant mode was TM_{012} . The absorbed power density, defined as the total power absorbed by the plasma divided by the volume of the plasma, ranged between 0.6 - 10.0 Watt/cm³. The gas was argon at pressures ranging from 0.3 Torr to 1.0 Torr. For these experimental conditions, the measured electron density varied between 3×10^{11} cm⁻³ and 8×10^{12} cm⁻³, the higher densities correspond to higher pressures. The electron temperature varied from 25,000 °K to 50,000 °K, the higher temperatures correspond to the lower pressures.

2.4.3 ECR SOURCES.

Many applications of ion sources in material processing require a high density ion beam to minimize the processing time. One way to achieve these ion currents is by applying higher powers to any ion source. This solution however, has some practical limitations. Some materials cannot withstand the heat produced by such high energy discharges. Also the cost of high power electrical equipment makes this idea somehow less attractive. Another solution is to increase the efficiency of the ion source. In the case of microwave discharges, this can be done by introducing a static magnetic field to promote electron cyclotron resonance.

Miyamura³⁵ tested a 26-cm ECR ion source for reactive ion beam etching. The discharge chamber is a waveguide type applicator with external tuning. The magnetic field is produced by three external electromagnetic coils surrounding the discharge chamber. The magnetic field strength varies along the axis of the discharge from 1.5 KG to 0.5 KG. The lowest value is near the extraction grids system. The excitation frequency was 2.45 GHz. A stable plasma was generated at pressures between 2×10^{-5} and 2×10^{-4} Torr. For an argon plasma, the measured electron temperature and the plasma density were about 3 eV and 5×10^{10} ions/cm³, respectively. The ion beam current density for C₄F₈ at an energy of 1 KeV was 0.3 mA/cm².

Another ECR ion source was tested by Tokiguchi³⁶. In this experiment, the plasma chamber was a cylindrical coaxial waveguide. The impedance matching between the plasma and the 2.45 GHz microwave circuit was performed by a movable short flange. A 1.5 KG magnetic field was supplied by two electromagnetic coils surrounding the discharge chamber. For an argon discharge a current density of 7 mA/cm² was obtained at a microwave power of 850 W.

2.5 ION SOURCE PERFORMANCE EQUATIONS

The evaluation of ion sources involves the experimental determination and calculation of several figures of merit.

The definitions of these quantities used in this thesis are briefly outlined in this section. The first of these is the degree of ionization, D . It is defined as being equal to the number density of ionized particles in the discharge divided by the equivalent number density of neutral particles and ions present in the discharge.

$$D = N_i / (N_n + N_i)$$

The ion density N_i can be directly measured with a Langmuir probe and the neutral particles density can be estimated in the case of a weakly ionized discharge if the discharge pressure is known.

The mass utilization efficiency, U_m , is defined as the number of ions extracted from the source divided by the number of neutral particles introduced into the discharge.

$$U_m = N_b / N_f$$

The number of extracted ions N_b is directly calculated from the measured ion beam current while the number of neutral particles N_f introduced to the discharge can also be calculated from the measured input gas flow rate.

The ion production power cost of an ion source is defined as the power absorbed by the discharge in Watt divided by the ion beam current (in Amperes) extracted from the discharge.

$$P_c = P_a / I_b$$

The power cost can also be expressed as the energy cost to produce an ion in electron volts per ion.

The ion beam current density j_b is defined as the ion beam current I_b divided by the total extraction area of the extraction grid system. Note that the grid extraction area defined as the total area of the grids where the extraction holes are located is different than the total holes or aperture area. The aperture area is the total area of the extraction holes. The ratio of the aperture area and the grid extraction area is called the geometrical transparency of the grid system.

2.6 REVIEW OF RF AND MICROWAVE ION SOURCES

Numerous recent applications in material processing, such as ion implantation, ion milling and plasma assisted deposition of thin films has stimulated interest in developing RF and microwave discharges for ion and plasma material processing. A review of many microwave ion and plasma sources including an analysis of different energy coupling methods is presented in Ref ⁷. An overview of some RF and microwave ion sources^{36,37,38,39,40,41} is presented in Table 2.1 where some figures of merit defined in the preceding section are displayed for each ion source. It should be noted that these ion sources are designed for different purposes. For example the ion source in Ref³⁷ was designed and optimized for low energy ion beams (< 1 KeV), whereas the ion source in Ref³⁶ was designed to achieve high

Table 2.1 Comparison of some Electrodeless Ion Sources

	FREQUENCY	DISCHARGE		FLOW	POWER	GRID	EXTRACTION	EXTRACTION	VOLTAGE	BEAM	CURRENT	BEAM	CURRENT	DENSITY	POWER	COST	MASS	UTILIZATION	E.C.R.
		PRESSURE	WATTS																
		mTORR	SCCM			cm ²	kV	mA	mA/cm ²										
HALLOW ⁺ CATHODE MODE	13.5 MHz	1	5.4	5.38	39	1<	20	0.5	27000	5.7	NO								
LOW ⁺ PRESSURE MODE	13.5 MHz	0.3	1.6	430	39	1<	13.5	0.3	32000	12.7	NO								
SAKUDO et al (Ref.36)	2.45 GHz	0.4	--	850	28.3	7	200	7	4200	--	YES								
RIT 10 (Ref.38)	2.0 MHz	2.0	--	100	78.5	--	140	1.78	764	30-37	NO								
NAKANISHI et al (Ref.40)	154 MHz	0.1	4	75	50	1.45	100	2	750	85	NO								
NAKANISHI et al (Ref.39)	160	--	4.6	30	50	1.4	60	1.2	415	18	NO								
ENGEMANN [*] et al (Ref.41)	27.12 MHz	0.75	0.015	500	20.3	2	40	2	12500	25	NO								

+ - LEJEUNE (REF.37)
* - OXYGEN DISCHARGE

ion beam currents. All the ion sources reviewed utilize flat-type multiaperture extraction grids and argon as the working gas except Ref⁴¹ where oxygen gas was used.

CHAPTER III

DEVELOPMENT OF A SIMPLE MODEL

3.1 INTRODUCTION.

The objective, in this chapter is to develop a semi-empirical model applicable to a low pressure microwave generated discharge. This model is derived from the fluid equations⁴². These equations are simplified using some justified approximations. The simplified theory results in a macroscopic treatment of the problem. The predictions of this model are also limited to low pressure discharges ($p < 0.5$ torr) where ambipolar diffusion is the dominant charged particle loss mechanism. Also for the purpose of simplicity, the discharge considered is free of any static magnetic field.

The main reason for developing such a model is to derive a set of equations that will correlate the controlled experimental parameters to the discharge characteristics without having to solve the exact problem which is considerably more complicated. The controlled experimental parameters are; the discharge pressure, the gas type, the gas flow, the microwave power absorbed and the diffusion

length. The parameters characterizing the discharge are; the electron density and temperature, the ion temperature and the charged particles flux.

Starting from the Boltzmann equation and Maxwell's equations, expressions for particle conservation, momentum transfer and energy conservation are derived for each particle species. All these equations are then separated into a time varying part and a time independent part. The time varying part is used to derive expressions for the plasma complex conductivity, equivalent complex dielectric constant and the absorbed power density. The time independent part is used to derive expressions for the parameters associated with the diffusion of the charged particles.

3.2 DERIVATION OF THE FLUID EQUATIONS.

The behavior of a gas discharge can be modeled by using the kinetic theory of gases. The most common model consists of treating the plasma as a mixture of different interpenetrating subgases, such as electron, positive ion and neutral gases. Each subgas is described by a separate Boltzmann equation. For a distribution function $f(r,v,t)$ describing the position and velocity of some particles at a

certain time t , the Boltzmann equation is:

$$\frac{\partial f}{\partial t} + \bar{v} \cdot \nabla_r f + \frac{\bar{F}}{m} \cdot \nabla_v f = \left(\frac{\partial f}{\partial t}\right)_c \quad (3.1)$$

This is a conservation equation in a six dimensional space⁴², where $dn = f(\bar{r}, \bar{v}, t) d^3r d^3v$ represents the number of particles in a volume of phase space $d^3r d^3v$. The term $\bar{v} \cdot \nabla_r f$ represents the diffusion of particles in the three dimensional configuration space. The effect of external accelerating forces applied to the particles is described by the $\bar{a} = \bar{F}/m$ term, and $\left(\frac{\partial f}{\partial t}\right)_c$ is the collision term representing a change in the distribution of particles in a six dimensional elementary volume $d^3r d^3v$ due to elastic and inelastic collisions. This equation can be written for each species existing in a plasma discharge.

A set of macroscopic equations can be derived from the Boltzmann equation by multiplying equation (3.1) with a specific function of velocity $\phi(\bar{v})$, and integrating over the velocity space.

$$\begin{aligned} & \int d^3v \phi(\bar{v}) \frac{\partial f}{\partial t} + \int d^3v \phi(\bar{v}) \bar{v} \cdot \nabla_r f \\ & + \int d^3v \phi(\bar{v}) \frac{\bar{F}}{m} \cdot \nabla_v f = \int d^3v \phi(\bar{v}) \left(\frac{\partial f}{\partial t}\right)_c \end{aligned} \quad (3.2)$$

Using vector identities, some of the terms in equation (3.2)

can be simplified yielding

$$\begin{aligned} & \frac{\partial N\langle\phi(v)\rangle}{\partial t} + \nabla_r N\langle\phi(v)\bar{v}\rangle \\ &= N \left[\frac{\partial\langle\phi(v)\rangle}{\partial t} + \langle\bar{v}\cdot\nabla_r\phi(v)\rangle + \langle\frac{\bar{F}}{m}\cdot\nabla_v\phi(v)\rangle + \Delta\phi_c \right] \end{aligned} \quad (3.3)$$

This equation is sometimes called the Boltzmann transport equation where N is the particle density and $\Delta\phi_c$ is the collision term. The symbol " $\langle\dots\rangle$ " represents the average over the velocity space. If $\phi(v)$ is explicitly independent of time and position, and if F is independent of velocity, then equation (3.3) becomes

$$\frac{\partial N\langle\phi(v)\rangle}{\partial t} + \nabla_r [N\langle\phi(v)\bar{v}\rangle] - \frac{\bar{F}}{m}\langle\nabla_v\phi(v)\rangle = \Delta\phi_c \quad (3.4)$$

In all the previous equations, the total instantaneous velocity v of an individual particle is equal to

$$\bar{v} = \bar{U} + \bar{V} \quad (3.5)$$

where \bar{U} is the random or thermal velocity (also called peculiar velocity) and \bar{V} is the average velocity.

Note that $\langle\bar{U}\rangle=0$

3.2.1 THE PARTICLES CONSERVATION EQUATION

The particle conservation equation is obtained from equation (3.3) by letting $\phi(v) = 1$.

A continuity equation can be written for each species in the discharge.

$$\frac{\partial N}{\partial t} + \nabla_r \cdot (N \bar{V}) = N (\text{Gain} - \text{Loss}) \quad (3.6)$$

For the electrons the conservation equation is

$$\frac{\partial N_e}{\partial t} + \nabla_r \cdot (N_e \bar{V}_e) = N_e \nu_i - \alpha N_e N_i - N_e \nu_A \quad (3.7)$$

where N_e = electron density

\bar{V}_e = average electron velocity

ν_i = ionization frequency

α = recombination coefficient

N_i = ion density

ν_a = attachment frequency.

For the ions the conservation equation is

$$\frac{\partial N_i}{\partial t} + \nabla_r \cdot (N_i \bar{V}_i) = N_i \nu_i - \alpha N_e N_i \quad (3.8)$$

and for the neutral particles;

$$\frac{\partial N_n}{\partial t} + \nabla_r \cdot (N_n \bar{V}_n) = N_n (\text{Gain} - \text{Loss}) \quad (3.9)$$

where N_n and \bar{V}_n are the neutrals density and velocity respectively.

For the case of a plasma excited by external static and time varying electric fields and using phasor notation, the internal electric field can be written as

$$\bar{E} = \bar{E}_0 + \bar{E}_1 e^{j\omega t} \quad (3.10)$$

where ω is the applied excitation frequency, \bar{E}_1 is the forced steady state response due to the sinusoidal driving electric field, and \bar{E}_0 is the sum of the forced response due to an external static electric field and the induced internal space-charge field. For the experiments described in later chapters the forcing electric field will only have a time varying part. In this case, the average velocity for each particle species can be expressed as

$$\bar{V} = \bar{V}_0 + \bar{V}_1 e^{j\omega t} \quad (3.11)$$

where \bar{V} is the total macroscopic velocity, \bar{V}_0 is the time independent component and the complex phasor $\bar{V}_1 e^{j\omega t}$ is the time varying component of the velocity. The particles density can also be separated in two components

$$N = N_0 + N_1 e^{j\omega t} \quad (3.12)$$

where N_0 and $N_1 e^{j\omega t}$ are the time independent and time varying components respectively. In the theory presented here, small perturbations about a steady state are assumed and thus

$$N_0 \gg N_1.$$

In the course of these calculations, complex phasor notation is used and thus care should be taken in the manipulation of nonlinear terms. Only the real part of the complex expressions have a physical meaning and special attention must be given to nonlinear operations. For example, it can

be shown that

$$\begin{aligned} & \text{Re}(a+be^{j\omega t})\text{Re}(c+de^{j\omega t}) \\ &= \text{Re}\left[ac + \frac{1}{2}bd^* + (ac+bd)e^{j\omega t} + \frac{1}{2}bde^{2j\omega t} \right] \end{aligned} \quad (3.13)$$

Under such conditions the continuity equations become;
for the electrons

$$\begin{aligned} j\omega N_{e1}e^{j\omega t} + \nabla_r \cdot [N_{e0}\bar{V}_{e0} + \frac{1}{2}\text{Re}(N_{e1}\bar{V}_{e1}^*) + (N_{e0}\bar{V}_{e1} + N_{e1}\bar{V}_{e0})e^{j\omega t} \\ + \frac{1}{2}N_{e1}\bar{V}_{e1}e^{2j\omega t}] = (N_{e0} + N_{e1}e^{j\omega t})(\nu_i - \alpha(N_{i0} + N_{i1}e^{j\omega t}) - \nu_A) \end{aligned} \quad (3.14)$$

and for the positively charged particles

$$\begin{aligned} j\omega N_{i1}e^{j\omega t} + \nabla_r \cdot [N_{i0}\bar{V}_{i0} + \frac{1}{2}\text{Re}(N_{i1}\bar{V}_{i1}^*) + (N_{i0}\bar{V}_{i1} + N_{i1}\bar{V}_{i0})e^{j\omega t} \\ + \frac{1}{2}N_{i1}\bar{V}_{i1}e^{2j\omega t}] = (N_{i0} + N_{i1}e^{j\omega t})(\nu_i - \alpha(N_{e0} + N_{e1}e^{j\omega t})) \end{aligned} \quad (3.15)$$

where the subscripts e and i are for electron and positive ion respectively.

The particle conservation equation for the neutral species remains unchanged since it is not affected directly by the applied electric field.

3.2.2 THE MOMENTUM TRANSFER EQUATION.

The momentum transfer equation for each subgas is obtained by letting $\phi(v) = m\bar{v}$ in equation (3.3)

$$\frac{\partial Nm\langle\bar{v}\rangle}{\partial t} + \nabla_r \cdot (Nm\langle\bar{v}\bar{v}\rangle) - \bar{F}N = - Nm\langle\bar{v}\rangle\nu_m \quad (3.16)$$

where ν_m is the momentum transfer collision frequency⁴²

$$Nm \frac{\partial \bar{v}}{\partial t} + m\bar{v} \frac{\partial N}{\partial t} + \nabla_r \cdot Nm(\bar{U}\bar{U} + \bar{V}\bar{V}) - \bar{F}N = - Nm\bar{v}\nu_m \quad (3.17)$$

$$Nm \frac{\partial \bar{v}}{\partial t} + m\bar{v} \frac{\partial N}{\partial t} + \nabla_r \cdot \bar{P} + \nabla_r \cdot (Nm(\bar{V}\bar{V})) - \bar{F}N = - Nm\bar{v}\nu_m \quad (3.18)$$

$$Nm \frac{\partial \bar{v}}{\partial t} + m\bar{v} \frac{\partial N}{\partial t} + \nabla_r \cdot \bar{P} + Nm(\bar{V} \cdot \nabla_r) \bar{V} + m\bar{v} \nabla_r \cdot (N\bar{V}) - \bar{F}N = - Nm\bar{v}\nu_m \quad (3.19)$$

From the particle conservation equation we have

$$m\bar{v} \frac{\partial N}{\partial t} = - m\bar{v} \nabla_r \cdot (N\bar{V}) + m\bar{v}NZ \quad (3.20)$$

where all the inelastic collision processes have been included in the term Z.

For the electrons

$$Z_e = \nu_i - \alpha N_i - \nu_A$$

and ν_{me} is the momentum transfer collision frequency for the electrons .

For the ions

$$Z_i = \nu_i - \alpha N_e$$

and ν_{mi} = is the momentum transfer collision frequency for the ions.

For the neutral gas

$$Z_n = \text{Gain} - \text{Loss}$$

Substituting equation (3.20) in (3.19), we obtain

$$Nm \frac{\partial \bar{V}}{\partial t} + \nabla_r \bar{P} + Nm(\bar{V} \cdot \nabla_r) \bar{V} - \bar{F}N = \bar{C} \quad (3.21)$$

Calling

$$\bar{C} = - Nm \nu_m \bar{V} - Nm \bar{V} Z$$

where $\bar{p} = Nm \langle \bar{U} \bar{U} \rangle$ is the pressure tensor, \bar{C} is the collision term, \bar{F} is the applied force and m is the particle mass. for the electrons we have

$$N_e m_e \frac{\partial \bar{V}_e}{\partial t} + \nabla_r \bar{P}_e + N_e m_e (\bar{V}_e \cdot \nabla_r) \bar{V}_e - \bar{F}_e N_e = \bar{C}_e \quad (3.22)$$

where C_e is the electron collision term.

$$\bar{C}_e = - N_e m_e \nu_{m_e} \bar{V}_e - N_e m_e \bar{V}_e Z_e \quad (3.23)$$

similarly for the ions;

$$N_i m_i \frac{\partial \bar{V}_i}{\partial t} + \nabla_r \bar{P}_i + N_i m_i (\bar{V}_i \cdot \nabla_r) \bar{V}_i - \bar{F}_i N_i = \bar{C}_i \quad (3.24)$$

where

$$\bar{C}_i = - N_i m_i \nu_{m_i} \bar{V}_i - N_i m_i \bar{V}_i Z_i \quad (3.25)$$

and for the neutrals;

$$N_n m_n \frac{\partial \bar{V}_n}{\partial t} + \nabla_r \bar{P}_n + N_n m_n (\bar{V}_n \cdot \nabla_r) \bar{V}_n - \bar{F}_n N_n = \bar{C}_n \quad (3.26)$$

where

$$\bar{C}_n = - N_n m_n \nu_{m_n} \bar{V}_n - N_n m_n \bar{V}_n Z_n \quad (3.27)$$

Replacing E, N and V by their steady state expressions, equations (3.22) and (3.24) become respectively

$$\begin{aligned} & m_e (N_{e0} + N_{e1} e^{j\omega t}) j\omega \bar{V}_{e1} e^{j\omega t} \\ & + \nabla_r \bar{P}_e (N_{e0} + N_{e1} e^{j\omega t}) [(\bar{V}_{e0} + \bar{V}_{e1} e^{j\omega t}) \cdot \nabla_r] (\bar{V}_{e0} + \bar{V}_{e1} e^{j\omega t}) \quad (3.28) \\ & + e [N_{e0} \bar{E}_0 + \frac{1}{2} N_{e1} \bar{E}_1 + (N_{e0} \bar{E}_1 + N_{e1} \bar{E}_0) e^{j\omega t} + \frac{1}{2} N_{e1} \bar{E}_1 e^{2j\omega t}] = \bar{C}_e \end{aligned}$$

and

$$\begin{aligned} & m_i (N_{i0} + N_{i1} e^{j\omega t}) j\omega \bar{V}_{i1} e^{j\omega t} \\ & + \nabla_r \bar{P}_i (N_{i0} + N_{i1} e^{j\omega t}) [(\bar{V}_{i0} + \bar{V}_{i1} e^{j\omega t}) \cdot \nabla_r] (\bar{V}_{i0} + \bar{V}_{i1} e^{j\omega t}) \quad (3.29) \\ & + e [N_{i0} \bar{E}_0 + \frac{1}{2} N_{i1} \bar{E}_1 + (N_{i0} \bar{E}_1 + N_{i1} \bar{E}_0) e^{j\omega t} + \frac{1}{2} N_{i1} \bar{E}_1 e^{2j\omega t}] = \bar{C}_i \end{aligned}$$

Equation (3.26) remains unchanged since the neutral particles are not directly affected by the electric field.

3.2.3 THE ENERGY CONSERVATION EQUATION.

the energy conservation equation is obtained from equation (3.3), by letting

$$\phi(v) = \frac{1}{2}mv^2$$

leading to

$$\frac{\partial}{\partial t} [N \frac{1}{2} m \langle v^2 \rangle] + \frac{1}{2} m \nabla_r \cdot N \langle v^2 \vec{v} \rangle = \frac{N}{2} \langle \vec{F} \cdot \nabla_v v^2 \rangle + \langle \frac{\partial}{\partial t} [N \frac{m}{2} v^2] \rangle_c \quad (3.30)$$

where $\langle \frac{\partial}{\partial t} [N \frac{m}{2} v^2] \rangle_c$ is the collision term which includes all the collision processes such as elastic, superelastic⁴², recombination, excitation, ionization etc.

$$\langle \vec{F} \cdot \nabla_v (\frac{v^2}{2}) \rangle = \langle \vec{F} \cdot \vec{v} \rangle \quad (3.31)$$

$$\langle v^2 \rangle = \langle U^2 \rangle + V^2 \quad (3.32)$$

$$\epsilon = \frac{1}{2} m \langle U^2 \rangle \quad (3.33)$$

$$\langle (\vec{v} \cdot \vec{v}) \vec{v} \rangle = \langle U^2 \vec{U} \rangle + V^2 \vec{V} + \langle U^2 \rangle \vec{V} + 2 \langle \vec{U} \vec{U} \rangle \cdot \vec{V} \quad (3.34)$$

Substituting the expression for the pressure tensor

$$\vec{p} = mN \langle \vec{U} \vec{U} \rangle \quad (3.35)$$

and the heat flow

$$\bar{q} = \frac{1}{2}mN\langle U^2\bar{U} \rangle \quad (3.36)$$

we obtain

$$\frac{\partial}{\partial t} \left(\frac{1}{2}mNV^2 + N\epsilon \right) + \nabla_r \cdot [q + N\epsilon\bar{V} + \frac{1}{2}mNV^2\bar{V} + \bar{p}\cdot\bar{V}] = N\langle \bar{F}\cdot\bar{V} \rangle + C_E \quad (3.37)$$

where the term C_E symbolizes all collision processes.

For the case of a time varying plasma, N and \bar{V} have to be replaced by the time varying equivalent expressions.

3.2.4 MAXWELL'S EQUATIONS.

All the preceding basic equations are coupled to Maxwell's equations which are listed bellow

$$\nabla \cdot \epsilon_0 \bar{E} = e(N_i - N_e) \quad (3.38)$$

$$\nabla \times \bar{H} = e(N_i \bar{V}_i - N_e \bar{V}_e) + \epsilon_0 \frac{\partial \bar{E}}{\partial t} \quad (3.39)$$

$$\nabla \times \bar{E} = -\mu_0 \frac{\partial \bar{H}}{\partial t} \quad (3.40)$$

$$\nabla \cdot \bar{H} = 0 \quad (3.41)$$

3.3 SIMPLIFYING ASSUMPTIONS.

Some additional assumptions are to be considered in order to find a reasonable solution to these equations.

3.3.1 ASSUMPTIONS.

a.) For the isotropic plasma approximation, the pressure tensor \bar{p} is considered as a scalar quantity $p = NkT$ and not a diatic. Implied in this assumption is that the gas particles have a Maxwellian distribution.

b.) The electron and ion temperatures are uniform throughout the discharge and constant with respect to time. The effect of non uniform gas temperature becomes noticeable at high currents and/or high pressures in a plasma column. Ecker⁴³ treated the case of a thermally inhomogeneous plasma column. When the assumption of constant temperature is dropped, the problem becomes much more complicated since the coefficients in the particle conservation law show a radial dependence. The electron temperature is no longer an eigenvalue of the problem, but becomes related to the electron density through the energy balance equation. The assumption of uniform temperature is used in the simple model presented in this thesis. A more complete model should include temperature nonuniformities.

c.) The inertia term $Nm(\bar{V} \cdot \nabla_r) \bar{V}$ in the momentum transfer equation for both the electrons and ion gases is neglected.

d.) There is no static magnetic field.

e.) The time dependent motion of the ions is neglected with respect to the electron motion for the case of a high frequency excitation field.

f.) Only diffusion losses are important. Volume recombination and attachment are neglected.

The assumption that only diffusion losses are important is justified if the discharge pressure and plasma density are low enough. Kagan⁴⁴ studied, experimentally, contractions in a positive column in the pressure range of 1-50 Torr for inert gases. Under such conditions it was shown that the volume occupied by the electrons does not change as the pressure is increased, suggesting that volume recombinations do not play a major role. All the experimental measurements presented in this thesis correspond to discharge pressures lower than 1 Torr, so the assumption that volume recombination can be neglected is justified for this model. At higher pressures, however, contraction of the region occupied by electrons is observed. The mechanism of contraction is explained by the fact that, at relatively high pressures, the the charged particles, produced mainly in the center of the column, recombine before reaching the tube walls and thus the discharge contracts into a narrow region. The high pressure allows volume recombination since the probability of a three body collision increases with pressure. Eletskaa⁴⁵ estimated that, at electron densities in the order of 10^{10} - 10^{13} cm⁻³

and an ambipolar diffusion coefficient of $10-100\text{cm}^2/\text{sec}$, only a predominance of molecular ions can cause contraction. Oskam⁴⁶ found that, at room temperature, atomic Ar^+ and Ne^+ ions change into molecular Ar_2^+ and Ne_2^+ at pressures higher than 10 Torr.

g.) Only singly ionized positive ions are present. This assumption is good for rare gases and relatively low input power.

h.) Only one step ionization is considered. A complete theory of low pressure discharges would require an exact solution to the Boltzmann equation for both electron and ion subgases. In order to solve these equations one would have to take into account all of the atoms and ions excited states. This requirement by itself makes the problem very hard, if not impossible to solve since many of the cross-sections for excitation and ionization from excited states are not very well known. This is an example that justifies why a common practice is to use simplified models for calculations. Kagan⁴⁷ developed a method that takes into account multistep ionizations. In this method the electron energy distribution was calculated for Neon gas for the pressure range of 5-20 Torr taking into account both elastic and inelastic collisions between electrons and atoms and between electrons and electrons. The number of direct ionizations

was calculated using this distribution function and so was the number of stepwise ionization events. The interesting result of this stepwise ionization treatment is that, in considering the number of stepwise ionization obtained by this method, further calculations give the same order of magnitude as the calculation based on the Maxwellian distribution assuming direct ionization. The fact that these two results are similar is a coincidence and does not imply a physical similarity. It is important, however, to note that the combination of the non-Maxwellian distribution and multistep ionization tends to give roughly the same results as the assumed one step ionization and a Maxwellian distribution.

i.) Ambipolar diffusion assumption.

The plasma model developed in this thesis is that of a gas discharge in which the loss mechanisms are assumed to be dominated by the diffusion of charged particles to the discharge chamber walls. The case where the diffusion of these particles is ambipolar is developed. This means that the plasma is assumed to be quasineutral, and that both electrons and positive ions diffuse to the discharge chamber walls at the same rate. The process of ambipolar diffusion is explained by the fact that the higher mobility of electrons allows them to move faster toward the walls. As a consequence, a negative voltage, with respect to the plasma voltage, begins to build near the walls. This negative

voltage will slow down the electron diffusion and increase the ion diffusion rate until the system reaches a steady state, where the diffusion rates of both species are equal. This model has been developed elsewhere⁴² and is reviewed here by using part of the equations of Section 3.2.

The assumptions related to this model are:

1. The flux of electrons entering or leaving an elementary volume is equal to the flux of positive ions;

$$\bar{\Gamma}_e = \bar{\Gamma}_i$$

2. The discharge is quasineutral i,e

$$N_e - N_i \ll N_e$$

and

$$N_e = N_i = N$$

It is a well known fact that free diffusion dominates in very low density discharges. In the free diffusion process, electrons and positive ions diffuse to the discharge walls independently of each other. Gerber⁴⁸ investigated the transition from ambipolar-to-free diffusion as a function of gas pressure and discharge tube size in Helium afterglow. Both theoretical and experimental results show that the transition begins when $\Delta / \langle \lambda_D \rangle = 86$ independent of pressure and size of the discharge tube, where $\langle \lambda_D \rangle$ is the

Debye length

$$\lambda_D = 69 \sqrt{\frac{T_e}{N_e}} \quad (\text{in m})$$

N_e is the average value of the electron density in m^{-3} and T_e is the electron temperature in degrees K. The transition happens progressively over several orders of magnitude in $\Delta / \langle \lambda_D \rangle$. The ions diffuse free by space charge effects when $\Delta / \langle \lambda_D \rangle$ is smaller than 0.25 .

All the experimental gas discharges obtained for this thesis correspond to a value of $\Delta / \langle \lambda_D \rangle$ larger than 50. Thus it is reasonable to assume that most of our experimental discharges correspond to the ambipolar diffusion regime. However, note that some discharge conditions ($\Delta / \langle \lambda_D \rangle < 86$) would correspond to the ambipolar-to-free fall diffusion transition regime. These conditions are obtained for the lower discharge pressure range.

3.3.2 PRACTICAL SIMPLIFICATION OF THE BASIC EQUATIONS.

Along with the previous assumptions we can further simplify the basic equations by adding the following approximations:

$$N_0 E_0 \gg N_1 E_1$$

$$N_0 E_1 \gg N_1 E_0$$

$$N_0 V_0 \gg N_1 V_1$$

$$N_0 V_1 \gg N_1 V_0$$

$$N_{i0} \gg N_{i1}$$

All these approximations are related to the assumption that the terms N_1 are considered as small perturbations about the steady states N_0 .

Second harmonic terms are also neglected.

With the application of these approximations, the particle conservation equation for the electrons becomes:

$$\nabla_r \cdot (N_{e0} \bar{V}_{e0} + (N_{e0} \bar{V}_{e1} + N_{e1} \bar{V}_{e0}) e^{j\omega t}) + j\omega N_{e1} e^{j\omega t} = (N_{e0} + N_{e1} e^{j\omega t}) \nu_i \quad (3.42)$$

this equation can be separated into a dc part

$$\nabla_r \cdot (N_{e0} \bar{V}_{e0}) = N_{e0} \nu_i \quad (3.43)$$

and an AC part

$$j\omega N_{e1} + \nabla_r \cdot (N_{e0} \bar{V}_{e1} + N_{e1} \bar{V}_{e0}) = N_{e1} \nu_i \quad (3.44)$$

For the ions, the DC part of the particle conservation equation is

$$\nabla_r \cdot (N_{i0} \bar{V}_{i0}) = N_{i0} \nu_i \quad (3.45)$$

and the AC part is

$$j\omega N_{i1} + \nabla_r \cdot (N_{i0} \bar{V}_{i1} + N_{i1} \bar{V}_{i0}) = 0 \quad (3.46)$$

The momentum transfer equation for the electrons becomes

$$\begin{aligned} j\omega m_e N_{e0} \bar{V}_{e1} e^{j\omega t} + e N_{e0} \bar{E}_0 + e N_{e0} \bar{E}_1 e^{j\omega t} + k T_e \nabla_r (N_{e0} + N_{e1} e^{j\omega t}) \\ = m_e \bar{V}_{e0} (\nu_{me} - \nu_i) (N_{e0} + N_{e1} e^{j\omega t}) \end{aligned} \quad (3.47)$$

where ν_{me} is the total collision frequency for momentum transfer due to binary elastic collisions between electrons and neutral particles and between electrons and ions, it often can be expressed as a sum of these two processes.

$$\nu_{me} = \nu_{men} + \nu_{mei} \quad (3.48)$$

where ν_{men} and ν_{mei} are the collision frequencies for momentum transfer between electrons and neutrals and between electrons and ions respectively. At moderate pressures (0.01-1 torr) in a weakly ionized gas $\nu_{men} \gg \nu_{mei}$ and $\nu_{me} = \nu_{men}$. However, for the case of a low pressure plasma (less than 0.01 Torr) when the discharge is no longer weakly ionized, ν_{mei} may become important. Also, an additional computation arises when ν_{men} is a function of velocity. A correction to ν_{men} must be made using the isotropic part of the distribution function. The result is an effective collision frequency for momentum transfer⁴²

$$\nu_e = \frac{\int_0^\infty v^3 \frac{\nu_{men}(v)}{\nu_{men}(v)^2 + \omega^2} \frac{\partial f_0}{\partial v} dv}{\int_0^\infty v^3 \frac{1}{\nu_{men}(v)^2 + \omega^2} \frac{\partial f_0}{\partial v} dv} \quad (3.49)$$

where $\frac{\partial f_0}{\partial v}$ is the first term of the expansion of the velocity distribution function of the electrons in spherical harmonics.

Equation (3.47) can also be separated into a DC part

$$eN_{e0}\bar{E}_0 + kT_e\nabla_r N_{e0} = N_{e0}\bar{V}_{e0}m_e\nu_e + N_{e0}\bar{V}_{e0}m_e\nu_i \quad (3.50)$$

and an AC part

$$(\nu_e + j\omega)m_e N_{e0}\bar{V}_{e1} = -eN_{e0}\bar{E}_1 \quad (3.51)$$

Similarly the momentum transfer equation for the ions is

$$-eN_{i0}\bar{E}_0 + kT_i\nabla_r N_{i0} = -N_{i0}\bar{V}_{i0}m_i\nu_{mi} \quad (3.52)$$

where ν_{mi} is the ion collision frequency for momentum transfer.

3.4 RF PLASMA MODEL.

Using the time varying part of the electron momentum transfer equation (3.51) and the effective collision frequency, we obtain

$$\bar{V}_{e1} = -\frac{e\bar{E}_1}{(\nu_e + j\omega)m_e} \quad (3.53)$$

Thus the expression for the time varying electron current

density is

$$\bar{J}_{e1} = -eN_{e0}\bar{V}_{e1} = \frac{e^2 N_{e0}}{(\nu_e + j\omega)m_e} \bar{E}_1 = \sigma \bar{E}_1 \quad (3.54)$$

where the RF plasma conductivity is

$$\sigma = \frac{e^2 N_{e0}}{(\nu_e + j\omega)m_e} \quad (3.55)$$

$$\sigma = \frac{e^2 N_{e0}}{m_e} \left[\frac{\nu_e}{\nu_e^2 + \omega^2} - j \frac{\omega}{\nu_e^2 + \omega^2} \right] \quad (3.56)$$

The expression for the plasma conductivity can be used to determine the power absorbed by the discharge in terms of the plasma parameters. The time average RF power absorbed by the plasma in an elementary volume is given by

$$P_{abs} = \frac{1}{2} \text{Re}(J \cdot E^*) = \frac{1}{2} \text{Re}(\sigma E^2) \quad (3.57)$$

substituting for σ from equation (3.55), we obtain

$$P_{abs} = \frac{e^2 N_{e0} \nu_e E^2}{2m_e(\nu_e^2 + \omega^2)} \quad (3.58)$$

Multiplying the numerator and denominator of equation (3.58) by the free space dielectric constant ϵ_0 , we get

$$\sigma = \frac{\omega_p^2 \epsilon_0}{\nu_e + j\omega} \quad (3.59)$$

where ω_p is the plasma frequency defined as

$$\omega_p^2 = \frac{N_{e0} e^2}{m_e \epsilon_0} \quad (3.60)$$

From the expression of the conductivity we can find the plasma complex dielectric constant ϵ_c . From Maxwell's equation

$$\nabla \times \bar{H} = \sigma \bar{E} + \epsilon_0 \frac{\partial \bar{E}}{\partial t} \quad (3.61)$$

$$\nabla \times \bar{H} = j\omega\epsilon_0(1 - j\frac{\nu}{\omega})\bar{E} \quad (3.62)$$

$$\nabla \times \bar{H} = j\omega\epsilon_0 \left[1 - j \frac{\omega_p^2 \epsilon_0}{\nu_e + j\omega} \right] \bar{E} \quad (3.63)$$

we can write

$$\epsilon_c = \epsilon_r + j\epsilon_i \quad (3.64)$$

where

$$\epsilon_r = 1 - \frac{\omega_{pe}^2}{\nu_e^2 + \omega^2} \quad (3.65)$$

$$\epsilon_i = \frac{\nu_e \omega_{pe}^2}{\omega (\nu_e^2 + \omega^2)} \quad (3.66)$$

For a steady state discharge the power absorbed by the plasma is equal the power losses in the plasma. It can be shown that the power loss by the electron gas per unit volume can be expressed as

$$\frac{e^2 E^2}{m_e \nu_e} = \left\{ \frac{5}{2} k T_e \right\} \left(\frac{D_a}{\Lambda} \right) + \nu_{men} \left(\frac{2m_e}{m_n} \right) \frac{3k}{2} (T_e - T_n) + eV_{ei} \nu_i + \sum_j eV_{exj} \nu_{exj} \quad (3.67)$$

where

D_a = Ambipolar diffusion constant (defined later in this chapter).

Λ = Diffusion length (defined later in this chapter).

T_e = Electron temperature.

T_N = Neutral gas temperature.

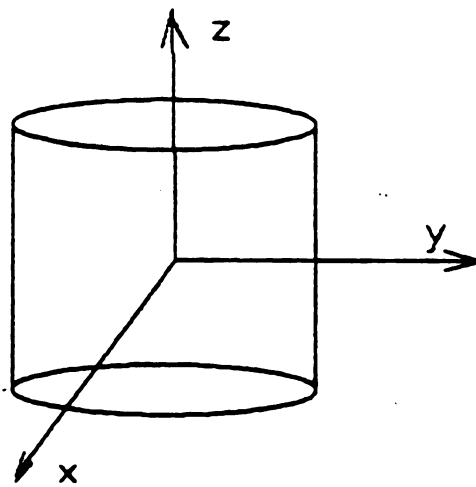
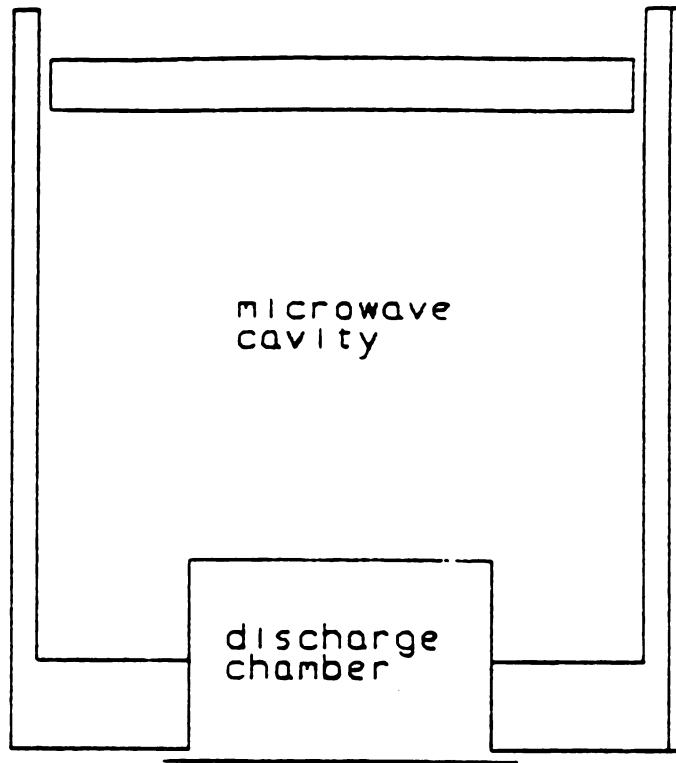
V_{ei} = Ionization potential

V_{exj} and ν_{exj} = excitation potentials and excitation frequencies of the atoms

The first term of eq (3.67) represents the energy loss by the electrons diffusing to the discharge chamber walls. The second term represents the energy transfer from the electron gas to the neutral gas due to elastic collisions. The third term represents the energy lost to ionization. The last term accounts for the energy loss by inelastic collisions.

3.5 THE AMBIPOLAR DIFFUSION MODEL FOR A CYLINDRICAL GEOMETRY.

the geometry considered in this thesis is that of a cylindrical microwave generated discharge. The discharge region is located at one end of a cylindrical microwave resonant cavity as shown in Figure (3.1). The plasma region is confined by a quartz disk forming one end of a cylinder, the other end of the cylinder consists of a circular opening in the lower base of the resonator and an electrically conducting plate adjacent to the bottom of the cavity. The inner radius of the discharge chamber is $R = 4.7$ cm and the



discharge axis

Figure 3.1 discharge geometry

length L is made variable by interchanging quartz dishes of different heights. The relatively low loss dielectric constant of quartz allows the resonant microwave fields to be transmitted to the discharge region without significant losses.

The electric fields interact with the electrons inside the chamber to break-down and maintain the discharge. The electromagnetic field distribution in the discharge chamber is directly related to the type of resonant mode selected. At this point we should note that the DC part of the particle conservation equation and the DC part of the momentum transfer equation are completely uncoupled from the time varying parts (see eq. 3.43 to 3.46 and 3.50 to 3.52). This was made possible with the use of approximations.

If we consider the time independent part of the momentum transfer equation for the electrons and ions. Substituting the expressions for the particle flux $\bar{\Gamma}_e = N_{e0}\bar{V}_{e0}$ for the electrons and $\bar{\Gamma}_i = N_{i0}\bar{V}_{i0}$ for the ions, equations (3.50) and (3.52) can be written as.

$$\bar{\Gamma}_e = -\frac{eN_{e0}\bar{E}_0}{m_e \nu_e} - \frac{kT_e \nabla N_{e0}}{m_e \nu_e} \quad (3.68)$$

$$\bar{\Gamma}_i = \frac{eN_{i0}\bar{E}_0}{m_i \nu_{mi}} - \frac{kT_i \nabla N_{i0}}{m_i \nu_{mi}} \quad (3.69)$$

Using the relation for the diffusion constants

$$\frac{kT_e}{m_e \nu_e} = D_e \quad ; \quad \frac{kT_i}{m_i \nu_{mi}} = D_i \quad (3.70)$$

and the mobilities

$$\frac{e}{m_e v_e} = \mu_e \quad ; \quad \frac{e}{m_i v_{mi}} = \mu_i \quad (3.71)$$

equations (3.68) and (3.69) become

$$\bar{\Gamma}_e = - N_{e0} \mu_e \bar{E}_0 - D_e \nabla N_{e0} \quad (3.72)$$

$$\bar{\Gamma}_i = N_{i0} \mu_i \bar{E}_0 - D_i \nabla N_{i0} \quad (3.73)$$

Substituting these terms in (3.43) and (3.45) and neglecting recombinations and attachments yields

$$\nabla \bar{\Gamma}_e = N_{e0} v_i \quad (3.74)$$

$$\nabla \bar{\Gamma}_i = N_{i0} v_i \quad (3.75)$$

using the assumption that $N_e = N_i = N$ and multiplying (3.72) by μ_i and (3.73) by μ_e and taking the sum

$$\left(\frac{\mu_i D_e + \mu_e D_i}{\mu_e + \mu_i} \right) \nabla^2 N = - N v_i \quad (3.76)$$

where

$$\frac{\mu_i D_e + \mu_e D_i}{\mu_e + \mu_i} = D_a \quad (3.77)$$

is the ambipolar diffusion constant

Equation (3.76) can be expressed as

$$N v_i + D_a \nabla^2 N = 0 \quad (3.78)$$

for the case of a cylindrical symmetry and steady state

$$\nabla^2 N + \left\{ \frac{\nu_i}{D_a} \right\} N = 0 \quad (3.79)$$

The radial solutions to this equation are the Bessel functions of the first kind, since the density has a finite value on the z axis, only the $J_n(x)$ functions are to be retained. Furthermore we can consider only $J_0(x)$ since higher order modes decay more rapidly. The axial solution is a combination of sin and cos functions. If the origin is chosen at the center of the cylinder as in Figure (3.1), the solution can be written as

$$N(r,z) = N_0 J_0(\beta_0 r) \cos(\alpha z) \quad (3.80)$$

where N_0 is the density along the axis of the cylinder and $\beta_0 = \nu_i/D_a$. The boundary conditions are $N(r,z)=0$ for $r=R$ and for $z = \pm L/2$, where R is the cylinder radius and L is the height.

Taking the first zero of $J_0(\beta_0 r)$

$$\beta_0 R = 2.405$$

and

$$\alpha = \frac{\pi}{L}$$

Substituting (3.80) in (3.79) and carrying out the derivation we obtain

$$\frac{\nu_i}{D_a} = \left(\frac{\pi}{L} \right)^2 + \left(\frac{2.405}{R} \right)^2 = \frac{1}{\Lambda^2} \quad (3.81)$$

where Λ is defined as the diffusion length of the cylindrical discharge volume. Equation (3.81) defines a

relation between the ionization frequency and the geometry of the discharge.

The ionization frequency is a function of the electron temperature T_e , pressure p_e and the gas type. It can be determined⁴² from

$$\nu_i = N \langle \sigma_i(v_e) v_e \rangle \quad (3.82)$$

where $\sigma_i(v_e)$ is the ionization cross section and v_e is the electrons speed

$$\langle \sigma_i(v_e) v_e \rangle = \int_0^{\infty} \sigma_i(v_e) v_e f(v_e) dv_e \quad (3.83)$$

For a Maxwellian distribution

$$f(v_e) = 4\pi \left[\frac{m}{2\pi k T_e} \right]^{\frac{3}{2}} e^{-\frac{m v_e^2}{2k T_e}} v_e^2 \quad (3.84)$$

or

$$f(\epsilon_e) = \frac{4\sqrt{\epsilon_e}}{\sqrt{\pi} (k T_e)^{\frac{3}{2}}} e^{-\frac{\epsilon_e}{k T_e}} \quad (3.85)$$

where ϵ_e is the electron kinetic energy. Figure 3.2 shows a typical superposition of a Maxwellian distribution and an ionization cross section. The ionization cross section can be approximated by two straight lines as shown in Figure 3.3, line (2) can be omitted in the integration when the distribution function goes to zero faster than the ionization cross section. If a_1 is the slope of line (1),

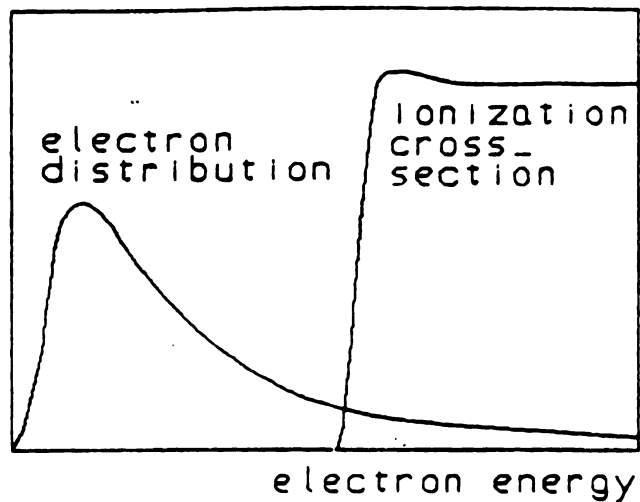


Figure 3.2 superposition of the electron distribution and the ionization cross section

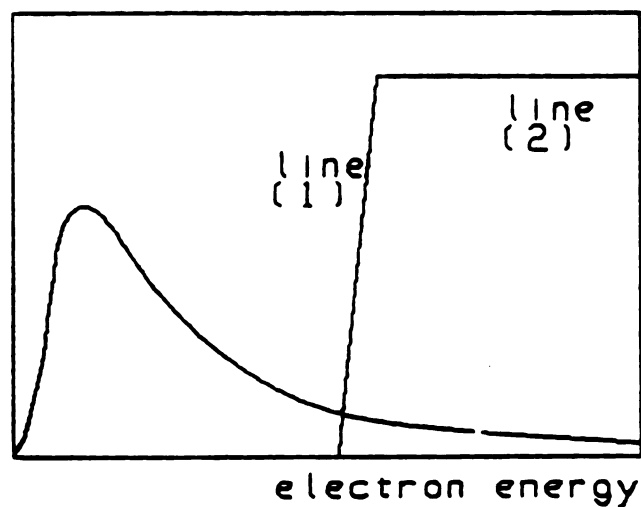


Figure 3.3 linear approximation of the ionization cross section

integral (3.83) becomes

$$\langle \sigma_i(\epsilon) v(\epsilon) \rangle = \left(\frac{m}{2\pi kT_e} \right)^{\frac{3}{2}} 4\pi a_i \int_{\epsilon_0}^{\infty} \sqrt{\frac{\epsilon}{2m_e}} e^{-\frac{\epsilon}{kT_e}} \left(\frac{2\epsilon}{m_e} \right)^{\frac{3}{2}} d\epsilon \quad (3.86)$$

and the ionization frequency is

$$\nu_i = \frac{4\sqrt{2}}{\sqrt{\pi m_e}} N a_i (kT_e)^{\frac{3}{2}} e^{-\frac{\epsilon_i}{kT_e}} \left(1 + \frac{\epsilon_i}{2kT_e} \right) \quad (3.87)$$

substituting in (3.81)

$$\frac{D_a}{\Lambda^2} = \frac{4\sqrt{2}}{\sqrt{\pi m_e}} N a_i (kT_e)^{\frac{3}{2}} e^{-\frac{\epsilon_i}{kT_e}} \left(1 + \frac{\epsilon_i}{2kT_e} \right) \quad (3.88)$$

but

$$D_a = \frac{\mu_i D_e + \mu_e D_i}{\mu_e + \mu_i}$$

and since

$$\mu_e \gg \mu_i \quad \text{and} \quad T_e \gg T_i$$

then

$$D_a = \frac{k T_e \mu_i}{e} \quad (3.89)$$

Equation (3.88) leads to

$$\Lambda^2 N^2 \left[\frac{4a_i \sqrt{2}}{\sqrt{\pi m_e}} \frac{e \sqrt{\epsilon_i}}{N \mu_i} \right] = \frac{\left(\frac{\epsilon_i}{kT_e} \right)^{\frac{1}{2}} e^{-\frac{\epsilon_i}{kT_e}}}{1 + \frac{\epsilon_i}{2kT_e}} \quad (3.90)$$

using the ideal gas approximation $p = N_n k T_n$, we get

$$C^2 p^2 \Lambda^2 = \frac{\left(\frac{\epsilon_i}{kT_e}\right)^{\frac{1}{2}} e^{\frac{\epsilon_i}{kT_e}}}{1 + \frac{\epsilon_i}{2kT_e}} \quad (3.91)$$

where

$$C^2 = \frac{4a_i \sqrt{2}}{\sqrt{\pi} m_e} \frac{e \sqrt{\epsilon_i}}{N \mu_i} \frac{1}{(kT_n)^2} \quad (3.92)$$

Equation (3.91) can be represented by a curve expressing

ϵ_i/kT_e versus $Cp \Lambda$ which is a universal curve for all atomic gases. The interpretation of this equation is that for a given gas the electron temperature is a unique function of the pressure diffusion length product and is independent of the electron density.

Many applications of plasma and ion sources require the knowledge of electron and positive ion currents flowing to the discharge chamber walls. In the case of an atomic gas the value of these currents can be derived from this model. Combining equation (3.72) and (3.73) along with the ambipolar diffusion assumption

$$\bar{\Gamma}_i = \bar{\Gamma}_e = \bar{\Gamma}$$

an expression for the charge particles flux is obtained

$$\bar{\Gamma} = -D_i \nabla N + \mu_i \frac{D_i - D_e}{\mu_e + \mu_i} \nabla N \quad (3.93)$$

This equation can be simplified knowing that $\mu_e \gg \mu_i$ and

$D_e \gg D_i$ to become

$$\bar{\Gamma} = - D_i \nabla N - \mu_i \frac{D_e}{\mu_e} \nabla N \quad (3.94)$$

$$\bar{\Gamma} = - \mu_i \frac{kT_e}{e} \nabla N \quad (3.95)$$

The total current flowing to the walls is obtained by multiplying $\bar{\Gamma}$ by the electron (or ion) electric charge and integrating over the walls surface.

Substituting the expression for N from equation (3.80) in equation (3.95), one can express the particles flux in two cylindrical components, the component of $\bar{\Gamma}$ in the \bar{v} direction being zero because of the azimuthal symmetry of the problem.

In the r direction

$$\Gamma_r = - \mu_i \frac{kT_e}{e} N_0 \cos\left(\frac{\pi z}{L}\right) \frac{\partial J_0\left(2.405 \frac{r}{R}\right)}{\partial r} \quad (3.96)$$

using the identities

$$2 \frac{dJ_n(x)}{dx} = J_{n-1}(x) - J_{n+1}(x)$$

and

$$J_{-1}(x) = - J_1(x)$$

we find

$$\Gamma_r = \mu_i \frac{kT_e}{e} N_0 \frac{2.405}{R} J_1\left(2.405 \frac{r}{R}\right) \cos\left(\frac{\pi z}{L}\right) \quad (3.97)$$

and

$$\Gamma_z = \mu_i \frac{kT_e}{e} N_o \frac{\pi}{L} J_o\left[2.405 \frac{r}{R}\right] \sin\left(\frac{\pi}{L}z\right) \quad (3.98)$$

The radial current is then

$$I_r = \mu_i kT_e N_o L (5.002) \quad (3.99)$$

and the current flowing to one end of the cylinder

$$I_z = 2 \pi^2 kT_e \frac{N_o}{L} \mu_i \int_0^R J_o\left[2.405 \frac{r}{R}\right] r dr \quad (3.100)$$

using the following identity and integrating

$$\frac{d J_n(x)}{dx} = J_{n-1}(x) - \frac{n}{x} J_n(x)$$

The total current of electrons or positive ions flowing to the walls is

$$I = \mu_i kT_e N_o \left[2 \frac{R^2}{L} (4.268) + L (5.002) \right] \quad (3.101)$$

The ion mobility μ_i is given by the relation

$$\mu_i = \frac{\mu_o T_i}{p T_o} \quad (3.102)$$

where μ_o is the ion mobility measured at temperature T_o in degree Kelvin and at a pressure of one Torr, p and T_i are the experimental pressure (in Torr) and ion temperature (in Kelvin) respectively.

In Reference⁴⁹ it is shown that the ion mobility is dependent of the ratio E/P , where E is the applied electric

field in a DC discharge, in the following way

$$\mu_i = \mu_i^* \left[1 + a_0 \left(\frac{E}{p} \right) \right]^{-\frac{1}{2}} \quad (3.103)$$

where μ_i^* and a_0 are constants that can be determined from experimental measurements of the mobility. Frost⁵⁰ shows an experimental plot of μ_i versus E/p for Argon at 1 Torr and 300⁰ K. From this data, μ_i^* and a_0 were calculated to be 1.3×10^3 (cm²/Volt-sec) and 2.3×10^{-2} (Torr/Volt cm) respectively. Using this result the ion mobility becomes

$$\mu_i = \frac{1.3 \times 10^3 T_i}{\left[1 + 2.3 \times 10^{-2} \left(\frac{E}{p} \right) \right]^{\frac{1}{2}} 300 p} \quad (3.104)$$

In an RF discharge E has to be replaced by the RF effective electric field which is defined in Chapter 5. Substituting equation (3.104) in (3.101), we obtain an expression for the currents flowing to the walls, in terms of the gas pressure and temperature, the electron temperature, the electron density, the dimensions of the discharge chamber and the applied electric field.

$$I = \frac{1.3 \times 10^3 T_i}{\left[1 + 2.3 \times 10^{-2} \left(\frac{E}{p} \right) \right]^{\frac{1}{2}} 300 p} k T_e N_o \left[2 \frac{R^2}{L} (4.268) + L (5.002) \right] \quad (3.105)$$

3.6 POSSIBLE IMPROVEMENT OF THIS MODEL.

The most frequently used method, for explaining some of the gas discharges properties, is based on the assumption that the electrons have a Maxwellian distribution. This is justified when the electron density is high enough to make the Coulomb relaxation the dominant energy transfer involving the electrons.

For electron densities lower than 10^{13} cm^{-3} , the inelastic electron-atom collisions play a more important role in depleting the high energy tail of the electron distribution. Vriens⁵¹ described a simple method that enables one to account for the large deviations from Maxwell distribution. The main purpose of the method is to obtain accurate values of averages over the electron velocity distribution without making it necessary to calculate the exact distribution function.

The energy conservation relation for the electrons in a gas discharge can be written as

$$P_E + P_{se1} + P_{rec} = P_{el} + P_{exc} + P_{ion} + P_{diff} \quad (3.106)$$

where P_E, P_{se1}, P_{rec} represent the electron energy gain such as from the electric field, superelastic collisions and recombinations respectively. P_{el}, P_{exc}, P_{ion} and P_{diff} are the energies lost through elastic collisions, exciting and ionizing collisions, and diffusion respectively.

In Vriens method, the electron temperature T_e is neither constant nor continuous. Instead, a subdivision is

made in two or possibly more energy regions. The region below the threshold of the first dominant inelastic process E_1 , corresponds to the bulk electrons. The region of energy higher than E_1 corresponds to the tail electrons. The bulk electrons are described by an effective temperature T_b equal to $2\langle E_e \rangle / 3k$, where $\langle E_e \rangle$ is the average electron energy. This is a good approximation if $\langle E_e \rangle$ is smaller than E_1 . The tail electrons are described by a temperature T_t which is determined uniquely by solving the system of two equations similar to equation (3.106), each of these corresponds to a different electron group. In this case a term is added to each equation to account for the Coulomb interaction between the two groups. T_b is clearly greater than T_t which value is determined by the atoms excitation levels considered in the method.

Results from this method were calculated for an Argon discharge, with a pressure of 5 Torr, and compared to experimental results. In these calculations the recombination and diffusion terms have being omitted because, the difference between these two terms in the energy equation is smaller than the sum of the terms representing the direct ionization and the ionization from excited states.

The values for the electric field, electron density and temperature used in these calculations were taken from experimental measurements. The following conclusions were drawn;

- a) Deviations from the Maxwell distribution are found to be very large for the excitation and direct ionization terms
- b) Calculated excited state densities are very close to the measured values, in contrast to calculations using the Maxwell distribution which predict much higher values.
- c) The energy flow to the tail is implemented mainly by Coulomb collisions. The superelastic collisions and electric field terms are negligible.
- d) Excitation is responsible for more than 85% of the energy lost by the tail electrons.
- e) Excited atoms are lost mainly by radiation, while ionization is of lesser importance in the loss process.

L.Vriens⁵² extends this method to a three electron group model. The three groups consist of one bulk and two tails. The tail electron temperatures are determined by considering two threshold energies for inelastic collisions instead of one.

The results of this three electron group model are in better agreement with measured values than the two group model. However, as more groups of electrons are considered in the calculations, the results converge toward the same values.

Other improvements of the model should include

- 1) The study of free fall diffusion regime at very low discharge pressures.
- 2) The characterization of the ion sheath region for

a better understanding of the processes involved in the plasma surface processing applications.

- 3) The study of the effects of a nonuniform applied electric field.

CHAPTER IV

EXPERIMENTAL SYSTEMS

4.1 INTRODUCTION

This chapter describes the experimental systems used to generate and measure the data presented in this thesis. The first part of this chapter, Section 4.2, presents the description of two microwave applicators used to generate and characterize a plasma and ion beam. The first applicator (applicator I) consists of a cylindrical microwave cavity without a static magnetic field. This applicator is later retrofitted with small samarium cobalt magnets to study the effect of a multicusp static magnetic field on the microwave discharge. Using the experimental results of the retrofitted applicator, a new applicator was designed and built. This new applicator included a total of 34 rare earth magnets which were positioned in a multicusp configuration to produce charged particle confinement and electron cyclotron resonance zones within the discharge volume.

The second part of this chapter describes the microwave circuit, gas flow and vacuum systems used in the experiments related to this thesis. Also described are the double

Langmuir probes and extraction systems and methods used to characterize the plasma and ion beam obtained with both applicators.

4.2 DESCRIPTION OF THE MICROWAVE ION SOURCES

4.2.1 MICROWAVE PLASMA DISK ION SOURCE, APPLICATOR I

4.2.1.1 THE CAVITY APPLICATOR DESCRIPTION

A cross-sectional view of the microwave plasma disk ion source³ is shown in Figure 4.1. This ion source consists of a 17.8 cm-i.d. brass cylinder (1) forming the outer conducting shell of the cavity applicator. The sliding short (2), the cavity end plate (3) and the cylinder (1) form the cylindrical cavity microwave excitation zone. The end plate is water cooled by means of an embedded circular water channel (19). The sliding short (2) is a movable circular end of the cavity and it is surrounded with a ring of silver coated finger stock (4) to insure good electrical contact with the cylindrical shell. The end plate (3) with a thickness of 0.9 cm is soldered to the other end of the cylinder (1). The working gas is introduced into the discharge chamber (5) by means of an annular ring (6), and the gas feed tube (7). A disk shaped quartz tube of 9.4 cm inside-diameter (8) confines the working gas to region (5),

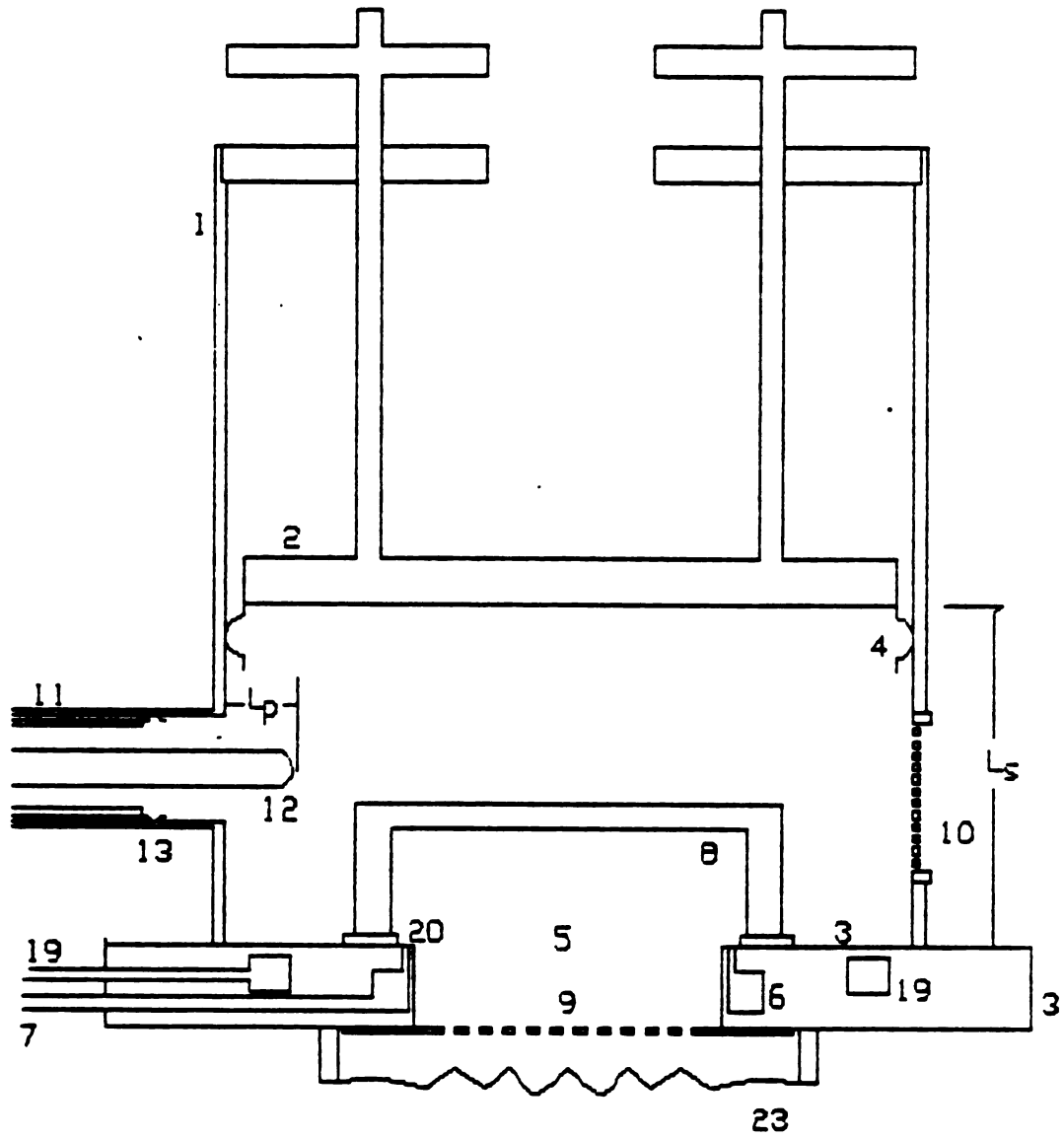


Figure 4.1 Cross Section of Applicator I

where the microwave fields produce a disk shaped plasma adjacent to the ion extraction grid system (9). The ion extraction grid system consists of either a single grid or double grid assembly and a neutralizer (23).

The ion source is designed to allow quartz disks of different heights to be easily interchanged and thereby allows plasma discharges of different thicknesses (or diffusion lengths) to be experimentally investigated. A silicon rubber gasket (20) positioned between the base of the quartz disk and the end plate provide a seal isolating the discharge region from the atmospheric pressure present in the cavity. The gasket is held in a 0.5 mm deep groove on the end plate. The discharge region is exposed to the vacuum system through the extraction grid holes. The pressure difference applied on the quartz disk holds it firmly to the end plate thus providing an adequate self vacuum seal.

A screen port (10) is cut in the cavity side wall for viewing the discharge. The microwave power is coupled into the cavity through the coaxial input port (11) via the length-adjustable coaxial input probe (12). Similar to the sliding short, silver plated finger stock (13) provide the required good electrical contact for the adjustable probe. The probe is connected to a coaxial feed line via an Andrew type N connector. A radial choke (24), shown later in Figure 4.20, is placed between this connector and the coupling probe to provide the DC electrical isolation of the

cavity from the ground potential when the high grid voltages are applied during ion extraction.

The sliding short and the adjustable excitation probe provide the impedance tuning required to match the applicator with and without the plasma. This cavity can be tuned to resonate in several electromagnetic modes such as TE_{211} , TE_{111} and TM_{011} . In this thesis however, only the TE_{211} mode was used because it was the mode choice of earlier experiments³. The tuning process involves the adjustment of the sliding short position L_S and the coupling probe position L_p . The method used for matching the cavity is described in References ^{3,14,53,54}. The sliding short is driven by a low RPM AC servo motor when the extraction high voltages are applied.

4.2.1.2 APPLICATOR OPERATION

In order to start a gas discharge, the cavity applicator has to be adjusted to resonate at the chosen mode (in this case the TE_{211} mode). For this purpose, a calibrated measuring system is designed to indicate the position of the sliding short L_S relative to the end plate which is a measure of the cavity length. Also, the excitation probe is calibrated to indicate its position L_p relative to the cavity side wall. A list of theoretical and

experimental values of L_S and L_P for several resonant modes is given in Table 4.1.

An initial calibration of the applicator is necessary since the values of the adjustable parameters L_S and L_P vary with each mode. Furthermore, they also depend on the size and shape of the quartz disk used. This calibration procedure is described in details elsewhere¹³. It consists of using a microwave circuit in which the frequency can be constantly varied by means of a sweep generator to display the power absorbed by the cavity versus the excitation frequency. This method can yield the quality factor Q of the cavity and the exact positions of the sliding short and the excitation probe for all the resonant modes allowed with or without the quartz disk present in the cavity. The identification of these resonant modes can be further verified by means of a micro-coaxial electric field probe. The experimental procedure which is employed when using the microcoax probes is also described in detail in Reference¹⁴. The electromagnetic field pattern as well as L_S and L_P for the TE_{211} mode are shown in Figures 4.2 and 4.3.

When the empty cavity (with the quartz disk) is tuned to the chosen resonant mode the discharge breakdown can be induced at relatively low microwave power (no more than 100 Watts) by a hand held Tesla coil. Since the electric field required to breakdown a discharge has a minimum value⁵⁵ at pressures typically between 100 mTorr to 10 Torr, it is often necessary to increase the the gas pressure

Table 4.1 Applicator I Tuning Parameters

SLIDING SHORT LENGTH L_S AND COUPLING
 PROBE POSITION L_P CORRESPONDING TO
 DIFFERENT RESONANT MODES FOR
 APPLICATOR I

EMPTY CAVITY						
MODES *	TE ₁₁₁	TM ₀₁₁	TE ₂₁₁	TE ₀₁₁	TM ₁₁₁	TE ₁₁₂
$L_S^{(EX)}$ (cm) *	6.2	7.1	8.05	10.85	11.0	13.1
$L_P^{(EX)}$ (cm)	+0.4	+0.5	+0.2	+0.15	+1.3	+0.4
$L_S^{(TH)}$ (cm) **	6.69	7.21	8.24	11.27	11.27	13.39

CAVITY WITH 1.8 cm DISK

$L_S^{(EX)}$ (cm) *	6.85	7.1	9.4	9.45	12.15	14.1
$L_P^{(EX)}$ (cm)	+0.3	+0.25	+0.5	+0.3	+0.2	+0.25

- * $L_S^{(EX)}$ = Measured sliding short position.
 * $L_P^{(EX)}$ = Measured probe position.
 ** $L_S^{(TH)}$ = Theoretical sliding short position.

Cross Section of TE_{211} Mode

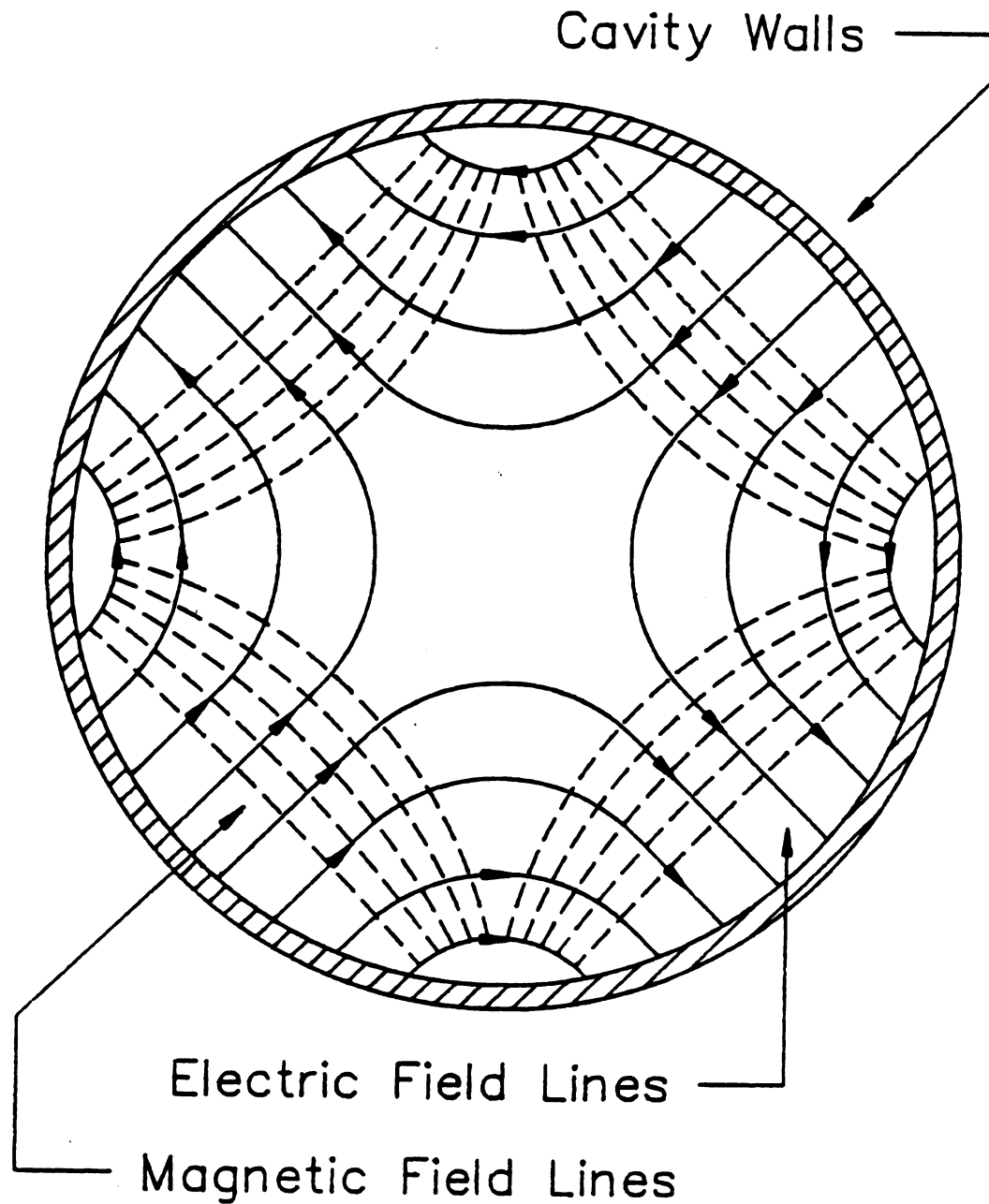


Figure 4.2 Cross Section of Cavity Mode

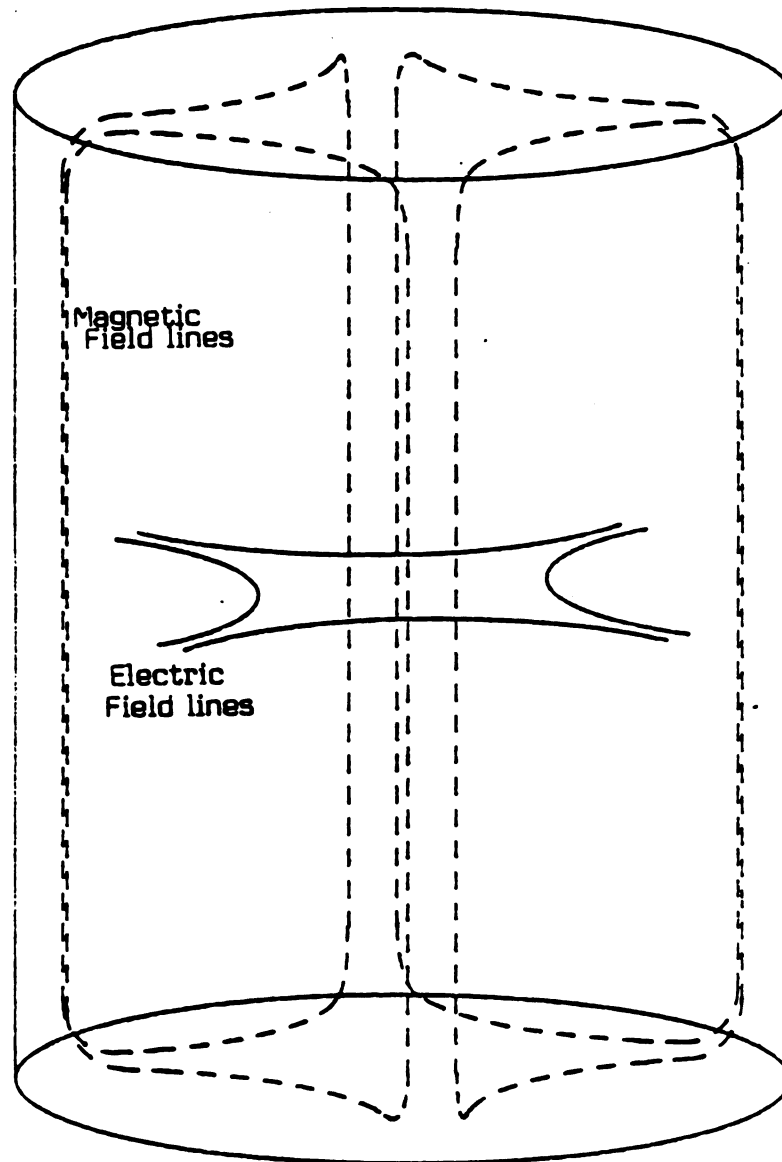


Figure 4.3 Three Dimensional View of the Electromagnetic Cavity Resonant Fields for the TE_{211} Mode

to > 10 mTorr by increasing the gas flow to ignite the plasma. Once the discharge is ignited, the cavity has to be retuned to compensate for the change of the dielectric constant in the discharge region. The expression for the plasma dielectric constant is given in equation (3.64). This operation requires the sliding short to be pulled out until the new matching condition is found. In practice, the cavity is considered to be tuned when the reflected power from the cavity-plasma system is brought to a minimum by iteratively varying the sliding short and the excitation probe positions. The discharge pressure can then be decreased by reducing the gas flow rate. Note that as seen in Chapter 3, any significant variation of the discharge pressure is followed by some variations of the discharge parameters such as plasma density, electron temperature, etc. Since the plasma dielectric constant is a function of the plasma density, it is then necessary to retune the cavity as these parameters are varied.

This process of tuning the cavity as the discharge conditions are changing is easily achieved when the discharge pressure remains higher than about 1 mTorr. When the pressure is further decreased the discharge becomes unstable and difficult to tune. An improvement of this system was needed in order to easily operate the discharge at very low pressures.

4.2.2 APPLICATOR I RETROFITTED WITH A MULTICUSP MAGNETIC FIELD.

At very low pressures the ion mobility increases since it is inversely proportional to the pressure as seen in equation (3.102). The increase of the ion mobility will result in a proportional increase in the ambipolar diffusion constant eq. (3.77 and 3.89). For example, argon gas at room temperature and at 1 mTorr has an atomic mean free path of about 8 cm and an electron mean free path of a same order of magnitude. These lengths are comparable to the discharge dimensions. As a result of this, the electrons in the low pressure discharge have a higher probability to diffuse to the chamber walls before they can make an ionizing collision with the neutral gas particles. This low pressure limitation can be solved by the application of a static magnetic field to the discharge.

The potential benefits of the addition of a static magnetic field are to

- (i) improve the microwave coupling efficiency at low pressures through electron cyclotron resonance (ECR). The condition for such a resonance exists when the rotation frequency of the electron around the magnetic field lines is equal to the microwave

excitation frequency. This condition can be expressed as

$$\omega_c = eB/m_e$$

where ω_c is the cyclotron frequency, B is the magnetic field, e and m_e are the electron charge and mass respectively. The value of B corresponding to $\omega_c = 2.45$ GHz, is 875 Gauss.

- (ii) improve discharge efficiency by reducing charged particles losses.

As a first step in applying a static magnetic field to the microwave discharge, applicator I described above was modified to include rare earth magnets. The modifications of this plasma disk ion source⁷ are displayed in Figure 4.4. In this configuration the 9.4 cm.i.d disk shaped zone (8) is surrounded by 17 2.54 x 2.54 x 1 cm samarium cobalt magnets. Each magnet has a maximum field strength of approximately 2.5 KG which is well in excess of the 875 G required for the electron cyclotron resonance at the excitation frequency of 2.45 GHz. Eight magnets (14) are positioned on a soft iron keeper (18) in a circle around and adjacent to the outer circumference of the disk. The poles of these magnets are alternated thus providing eight magnetic cusps. The magnetic field of all the rare earth magnets is oriented

parallel to their 1 cm thickness. There are two different ways for positioning these magnets. The first configuration consisted in placing these magnets in an upright position with the 2.54 cm square magnetic pole faces tangent to the quartz enclosure. This position maximized the radial magnetic field exposed to the discharge chamber. This configuration was tested and a discharge was obtained. In this discharge eight distinct very bright plasma regions were observed near the eight surrounding magnets. These bright regions correspond to the ECR zones in the discharge. However, as the discharge pressure was further reduced during the experiment, the discharge became instable. This instability was attributed to the fact that in the upright position, the eight magnets surrounding the discharge created a conducting shield preventing the microwave resonant fields from efficiently reaching the discharge region. In addition the intrusion of these magnets in the cavity region caused a substantial perturbation of the resonant modes.

A second configuration was tested where the eight rare earth magnets surrounding the discharge were positioned as shown in Figures 4.4 and 4.5 to minimize the resonant fields perturbation. In this configuration, more stable discharges were obtained at lower pressures, but since the orientation of the magnets was not optimum, no ECR zones could be sighted in the discharge. This magnetic field geometry was

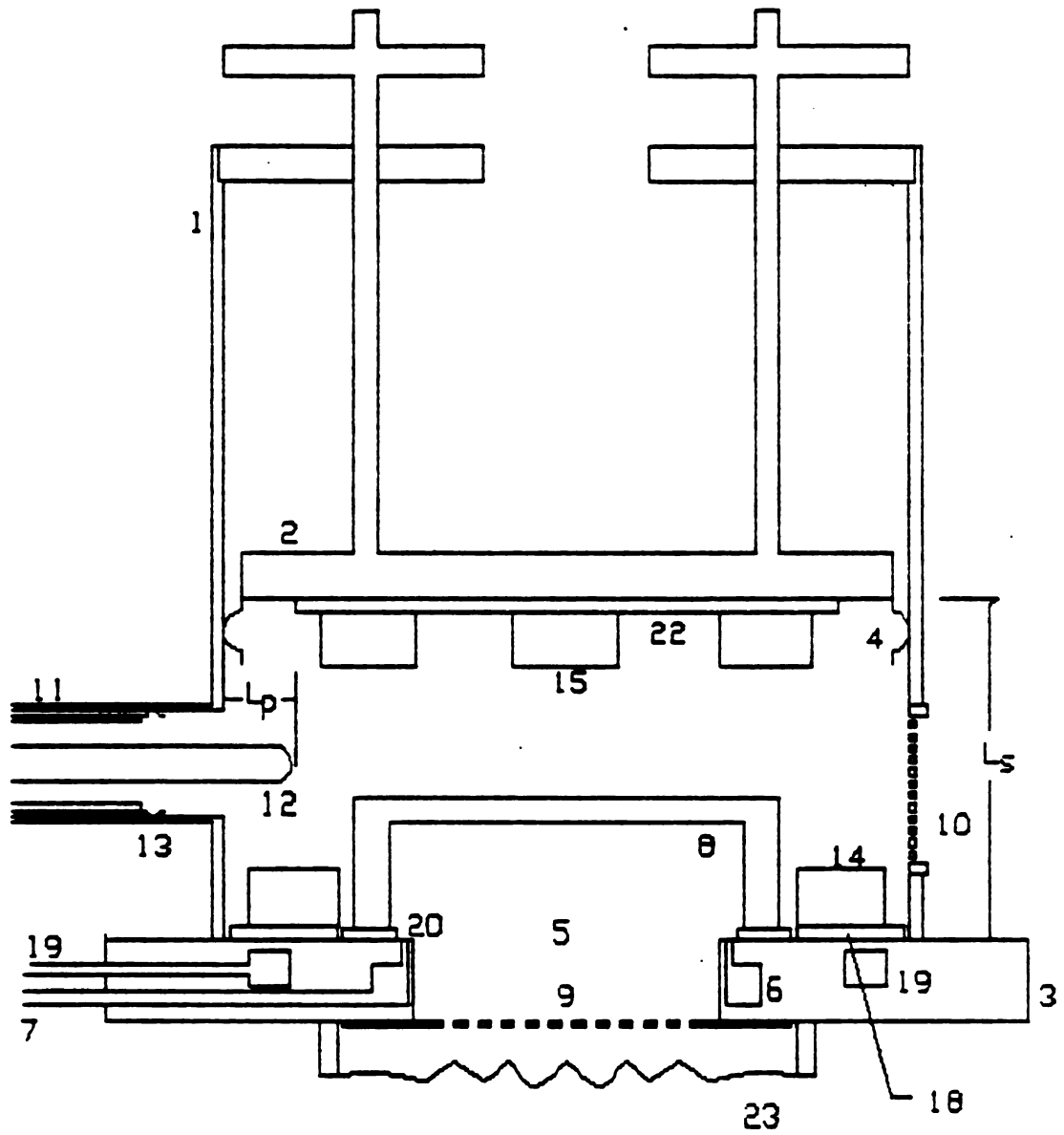
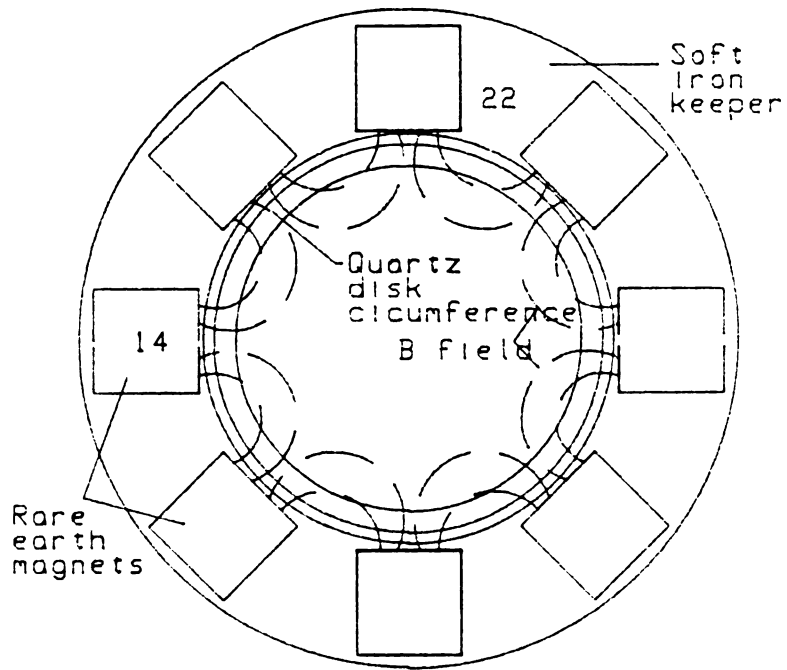


Figure 4.4 Cross Section of Applicator I
Retrofitted with Rare Earth Magnets

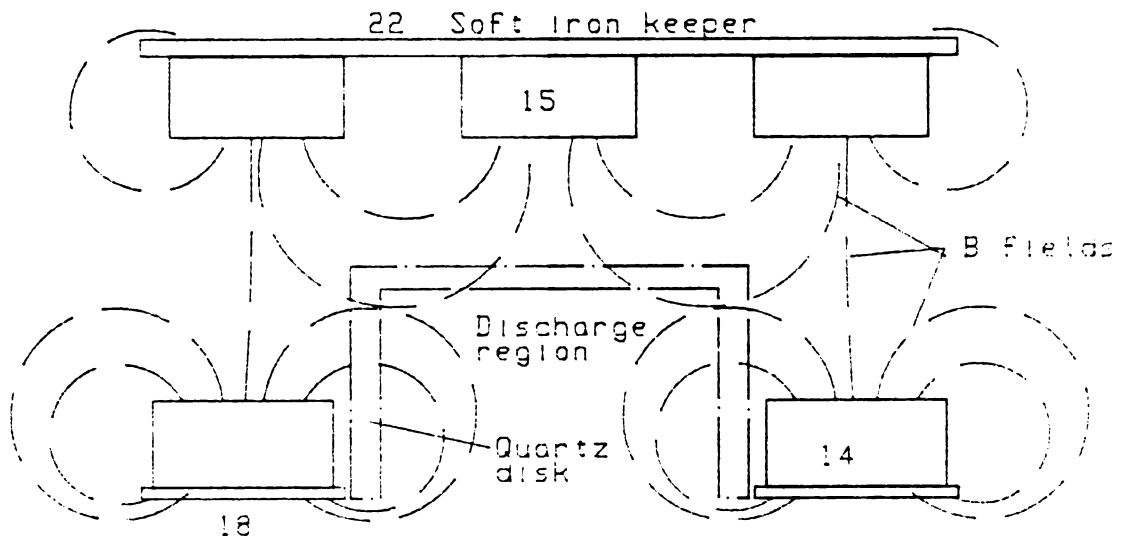
preferred over the first configuration because it provided stable low pressure discharges.

The other 9 alternating pole magnets (15) are positioned on a circular soft iron plate (22) at the bottom side of the sliding short. The magnetic fields obtained with this configuration are sketched in Figure 4.5.

The main improvement achieved with this configuration is a better stability of the gas discharge at low pressures. The plasma stability is the result of the magnetic field confinement of the charged particles. However, there is no evidence of electron cyclotron resonance mainly because the optimum position of the magnets around the discharge region could not be achieved. Due to their limited field strength, the best position for these magnets to promote ECR is upright and as close as possible to the quartz disk side walls. However, in such a location the magnets would partially shield the discharge from the microwave excitation fields. In addition, the intrusion of the magnets inside the microwave cavity causes a perturbation of the resonant electromagnetic fields. The result is a limitation in matching the microwave power into the cavity-plasma system. The reflected power could not be reduced to a value lower than 10% of the incident power.



(a) Top view



(b) Cross sectional view

Figure 4.5 Magnetic Field Lines in Applicator I Retrofitted

4.2.3 MULTICUSP MICROWAVE ION SOURCE

Using the experimental knowledge acquired with applicator I, a new design was developed. This new design is based on the original ion source where the end plate and the sliding short have been modified to remove the rare earth magnets from the electromagnetic excitation region in the cavity. The advantage here is to prevent the conducting magnets from interfering with the microwave resonant fields and use the static magnetic field more efficiently. Figures 4.6 to 4.8 display a cross-sectional view and photographs of this ECR ion source. Similar to the earlier design the ion source consists of a 17.8 cm i.d. brass cylinder (1) where the screen viewing port (10) and the coaxial input port (11) have been positioned closer to the end plate to allow the sliding short to reach lower cavity lengths. Silver plated finger stock ((4) and (13)) is used for good electrical contact.

The end plate (3) can be pulled apart from the brass cylinder (1) when not in operation allowing for easy examination or replacement of the quartz disk (8). During cavity excitation, four threaded bolts (16) firmly hold the end plate (3b) onto the cylinder (1). The end plate consists of two separate pieces (3a) and (3b) bolted tightly together. The piece (3a) adjacent to the interior of the cavity is made from brass, while piece (3b), which is

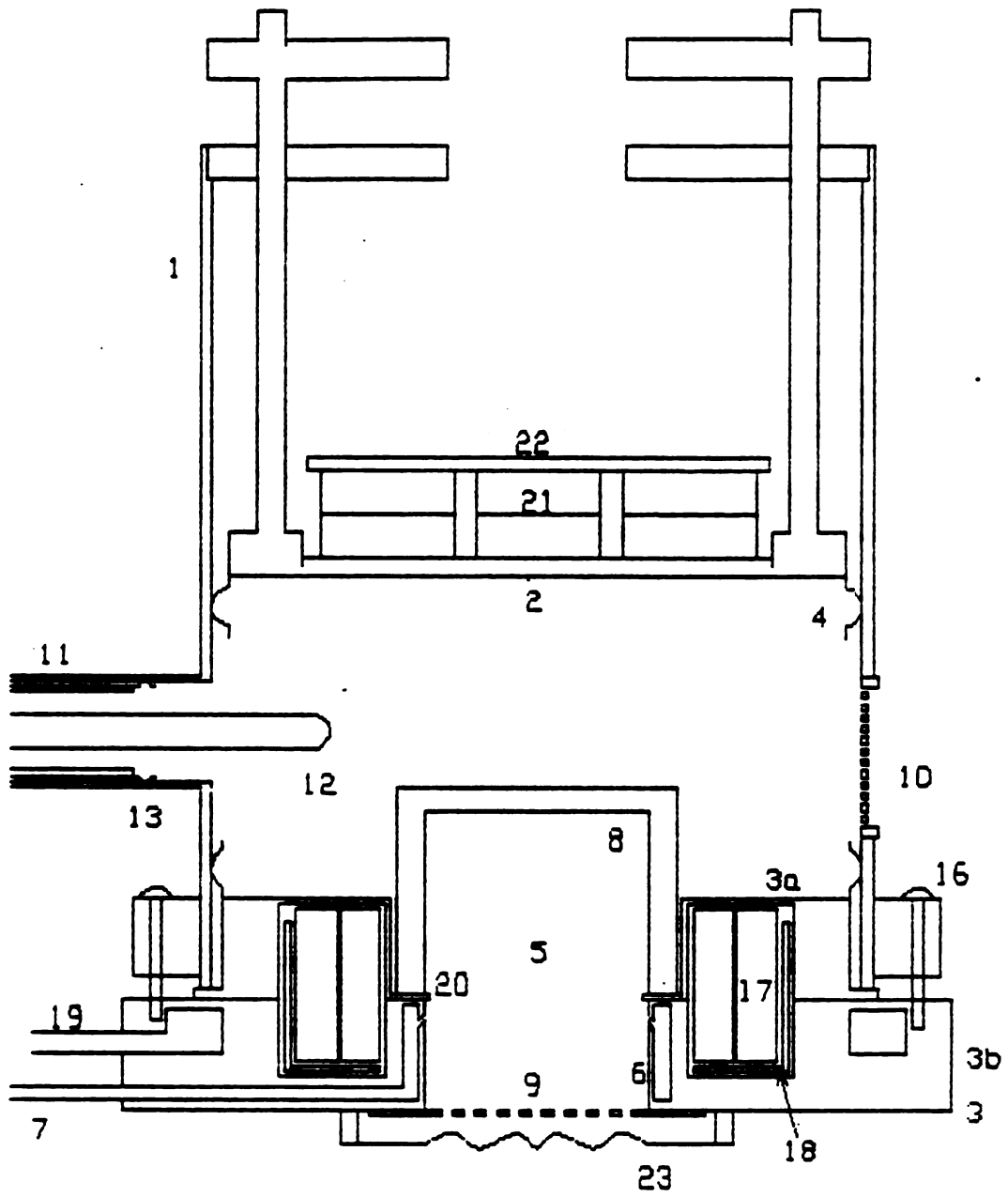


Figure 4.6 Cross Section of ECR Applicator

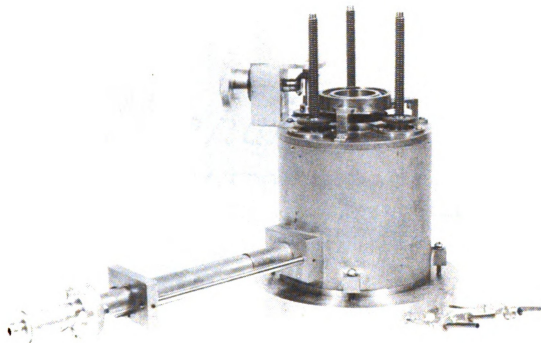
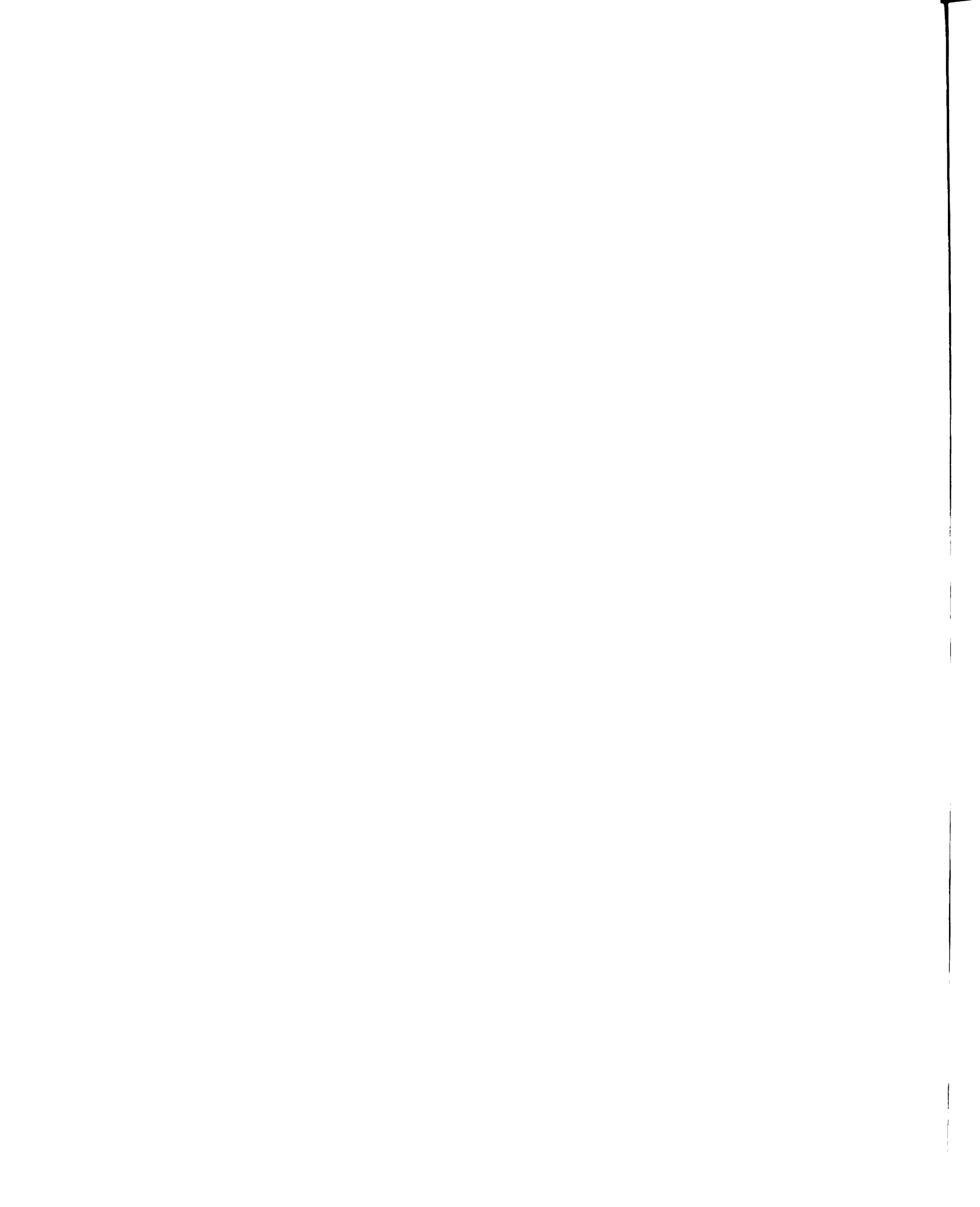


Figure 4.7 Photograph of Assembled ECR Applicator



Figure 4.8 Photograph of the ECR Applicator Disassembled



exposed to the discharge and the downstream high vacuum, is machined from nonmagnetic stainless steel. These two cylindrical pieces enclose sixteen 2.54 x 2.54 x 1 cm samarium cobalt magnets (17). Each magnet has a maximum field strength of approximately 2.5 KG. Eight pairs of magnets (17) are equally spaced on a circle around and adjacent to the radial gas feed annular ring (6) and quartz discharge chamber (5). The magnet pairs are placed in series and are arranged on a soft iron keeper (18) with alternate poles in the circumferencial direction forming a multicusp, octapole, static magnetic field across a radial plane as shown in the cross-sectional view of Figure 4.9.

Field maps of the multicusp magnetic fields are also displayed in Figures 4.9 and 4.10. The magnetic fields mapping was obtained with a method utilizing iron filings, the method is described in more detail in Appendix A. The magnetic field strength produced by these magnets is near zero at the center and increases in the radial direction. Each magnetic pole pair produces a pole face with a maximum field strength of approximately 3 KG which is well in excess of the 875 G required for electron cyclotron resonance. The strength and position of these magnet pairs produces a radial magnetic field surface in excess of 875 G in the discharge zone and thus, as shown in Figure 4.9, results in an undulating radial ECR layer inside the quartz chamber. The iron keeper (18) has an L-shaped cross-section and is placed on the outer radius and under the magnet pairs, and

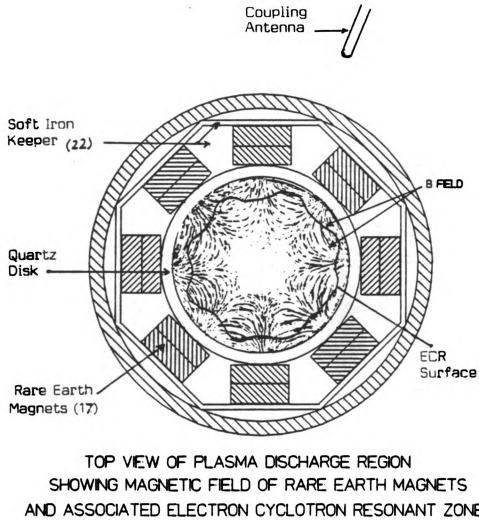


Figure 4.9 Radial Magnetic Field Lines in the ECR Applicator

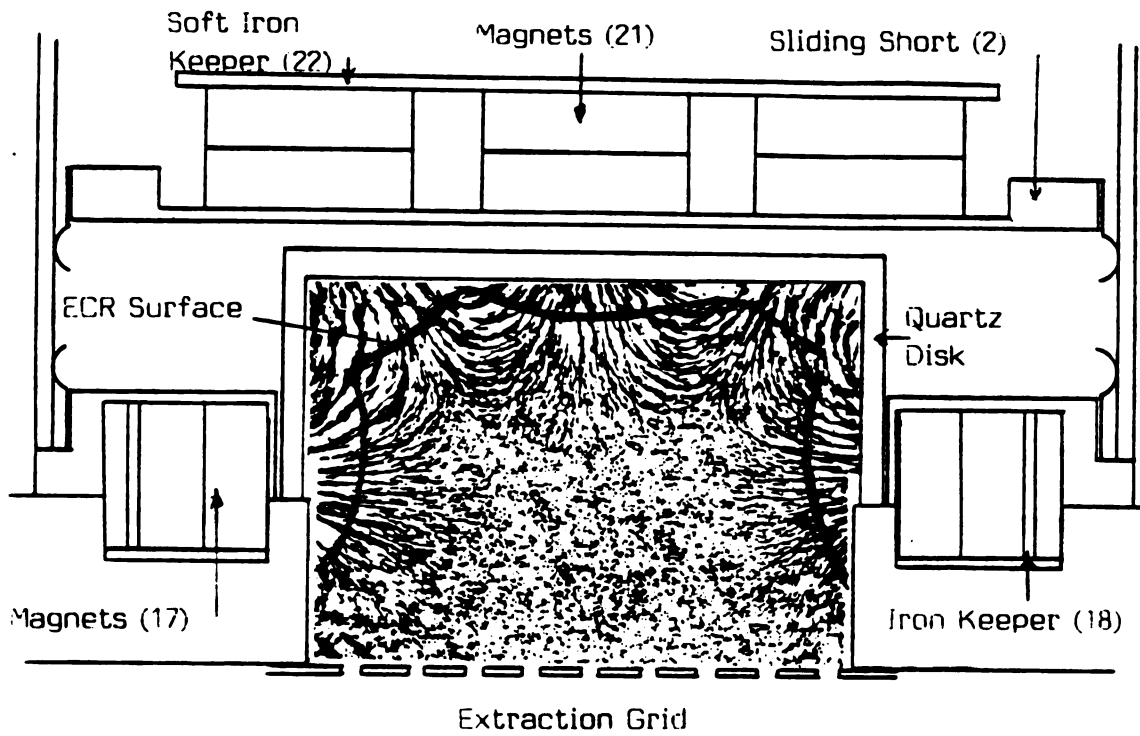


Figure 4.10 Cross Sectional View Showing the Static Magnetic Field Lines in the ECR Applicator

thus reduces the fringing static field in the grid extraction zone.

Also shown in Figure 4.6, nine rare earth magnet pairs (21) identical to the above-mentioned magnets, are arranged in a 3 x 3 square array with a 14 cm diagonal. They are placed on a circular, thin, soft iron keeper (22) and are either located on the interior surface of the sliding short as described earlier in Figure 4.4, or as is shown in Figure 4.6, are located outside the cavity excitation zone. Similar to the radial octapole, the poles of the nine magnet pairs alternate. This nine-pole array is aligned so that the poles of the eight outer magnets alternate with the poles of the radial octapole. Thus, a multicusp magnetic field is also formed over the flat circular end surface of the discharge, and the magnetic field lines from magnets (21) also interconnect with the radial octapole field from magnets (17).

4.3 GENERAL EXPERIMENTAL SYSTEM

4.3.1 VACUUM AND GAS FLOW SYSTEMS.

The gas flow system and vacuum system are shown in Figure 4.11. Starting from the gas cylinder and regulator, the gas flow is divided in two parallel paths. The upper

path is designed to function with manual controls and is mainly used for the higher flow rates (20 sccm - 100 sccm). It consists of a rotameter, a pressure gage and two needle valves. The valves are used to control the gas flow rate and the back-pressure. The pressure gage is used to accurately monitor the gas pressure before reaching the rotameter. This pressure control is needed since the rotameter is calibrated for a constant back-pressure. The lower gas path is designed for the lower flow rates (0.5 sccm - 50 sccm). It consists of a Tylan mass flow controller and two valves used to isolate this path if needed. These two paths converge toward a common line connected to the microwave cavity. On this line, a 30 cm long quartz tube is used to electrically isolate the microwave cavity from the rest of the gas flow system. This isolation is necessary since the cavity is held at a high potential during ion beam extraction. The ion source is located on top of a 45.7 cm radius by 45.7 cm cylindrical bell jar which could be pumped down to 10^{-6} Torr.

The vacuum system consists of a 10 inch NRC diffusion pump with a water cooled cold trap and a roughing pump. This system is separated from the bell jar by an air pressure driven throttle valve.

The bell-jar pressure is directly measured by means of a thermocouple gage and ion gage as shown in Figure 4.11. The discharge pressure was deduced from the bell-jar pressure and the gas flow rate using a thermodynamic

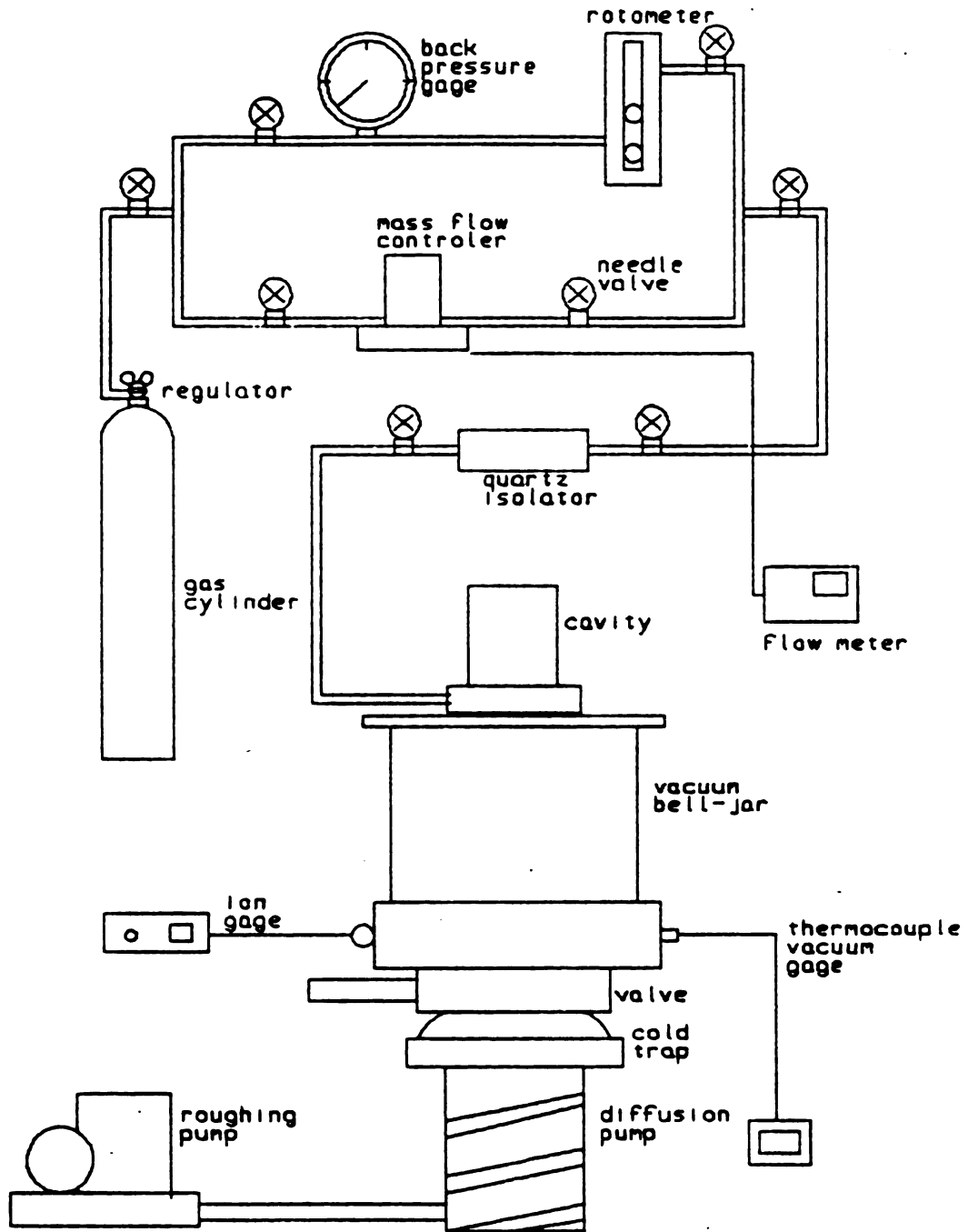


Figure 4.11 Gas Flow and Vacuum Systems

calculation⁵⁶. This calculation takes into account the total area of the grids holes linking the discharge chamber to the bell-jar. The equation for the gas pressure in Pascal inside the discharge chamber is

$$p_d = \frac{q(2\pi km)^{\frac{1}{2}}}{A} \sqrt{T_d} + p_{bj} \sqrt{\frac{T_d}{T_{bj}}} \quad (4.1)$$

where m in Kg is the gas particles mass, T_d is the discharge temperature in degree Kelvin, q is the gas flow rate in particles per second, A is the total area of the holes in m^2 , p_{bj} is the bell-jar pressure and T_{bj} is the bell-jar temperature.

4.3.2 MICROWAVE SYSTEM.

The microwave circuit used in these experiments is shown in Figure 4.12. It consists of a variable power (0.0 to 400 Watts) CW Holaday microwave power source. The frequency of this source is 2.45 GHz and is very frequency stable at operating powers higher than 70 Watts. The waveguide output of the source is connected to a three port circulator via a 3 in x 1.5 in rectangular waveguide. The circulator is used to prevent any reflected power from returning to the magnetron tube and causing possible damage from overheating. The reflected power is directed to a 500 Watt water cooled matched load where it is absorbed. The output power from the microwave source and the power

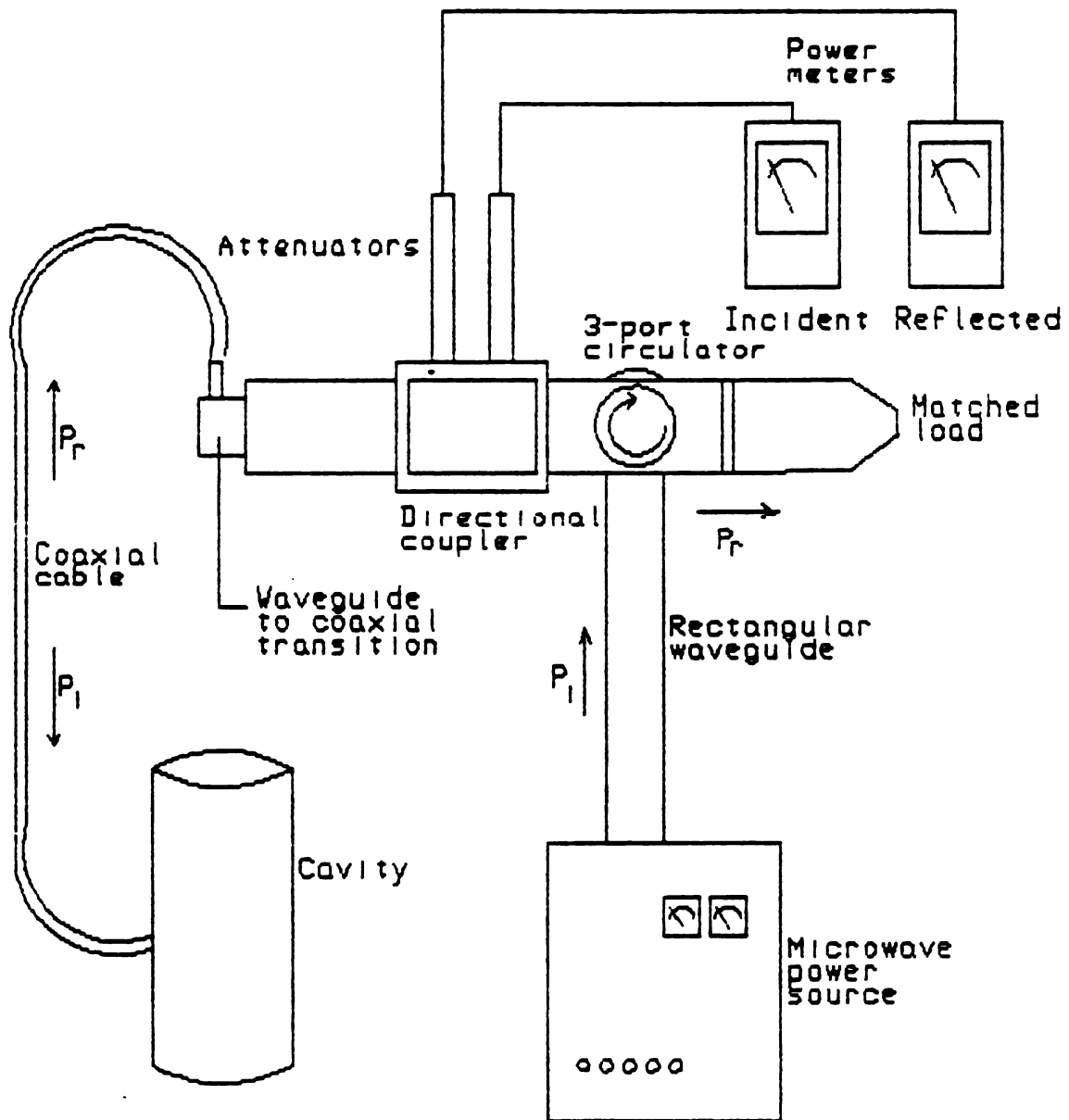


Figure 4.12 Microwave System

reflected from the resonant cavity are measured through a 20 db Microlab/FXR directional coupler. These powers are further reduced with a 40 db attenuator for the incident power and 20 db attenuator for the reflected power and then measured with two Hewlett-Packard 432A power meters. The power coupled into the cavity-plasma system was measured and calibrated for this circuit as follows

$$P_C = 230 \times P_{mI} - 18.6 \times P_{mR},$$

where P_{mI} is the incident power read on the power meter and P_{mR} is the reflected power also read on the meter. The microwave power is then coupled into the cavity with a type N coaxial cable.

4.3.3 ELECTRON DENSITY AND TEMPERATURE MEASUREMENTS.

The method used to determine the ion density and the electron temperature is described in Reference⁵⁷. The experimental setup consists of a double Langmuir probe shown in Figure 4.13. The probes length is 0.356 cm, the diameter is 0.0254 cm for each probe and the separation between the two probes is 0.35 cm. The reason for this choice is the reasonable accuracy obtained in measuring the electron temperature due to the fact that the size of the probes is small enough not to disturb the plasma. Also, the

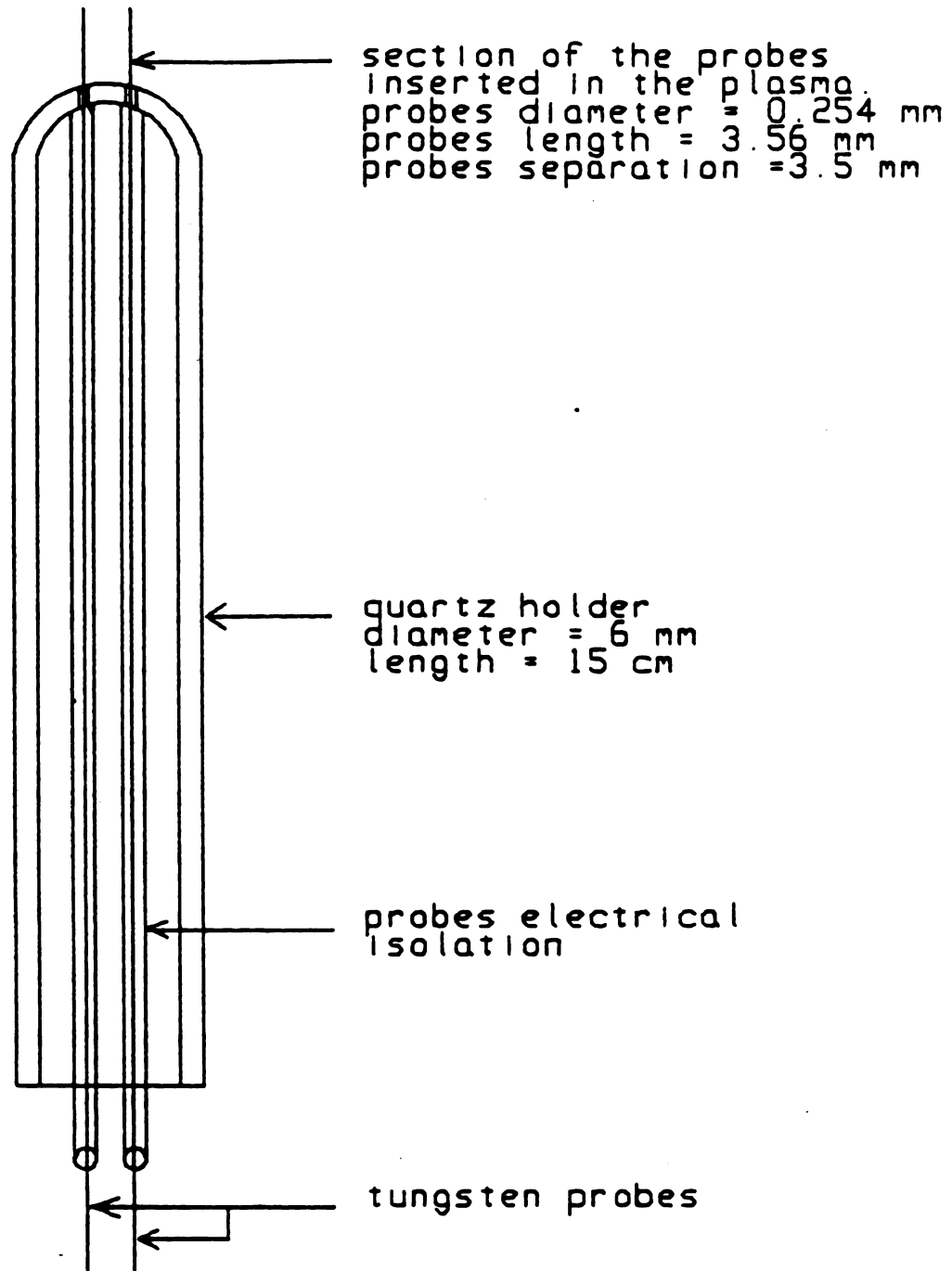


Figure 4.13 Langmuir double probe system

separation between the probes has to be larger than many Debye lengths. An expression for the Debye length in meters is given as

$$\lambda_D = 69.0 (T_e/N_e)^{1/2} \quad (4.2)$$

where T_e is the electron temperature in Kelvin and N_e is the electron density in m^{-3} . As an example, for a plasma with $T_e = 50,000$ °K and $N_e = 1 \times 10^{12}$ cm^{-3} , the Debye length is $\lambda_D = 1.5 \times 10^{-2}$ mm.

The double probe measurement technique assumes a Maxwellian distribution for the electrons so that the concept of temperature is justified. It is based on the Boltzmann relation and the plasma-sheath properties of a gas discharge. In addition it is based on an application of Kirchhoff's law, which requires, in this case that at any time the total net current of positive ions and electrons flowing to the probes from the plasma must be zero. A qualitative treatment on how the system works can be described in the paragraphs below.

The electrical circuit used to bias the Langmuir double probe is shown in Figure 4.14. When the voltage between the two probes is zero, each probe will collect zero net current from the plasma and will ride at the same floating potential, since the number of electrons reaching each probe equals the number of positive ions. As the voltage of one probe is made negative relative to the other probe, the

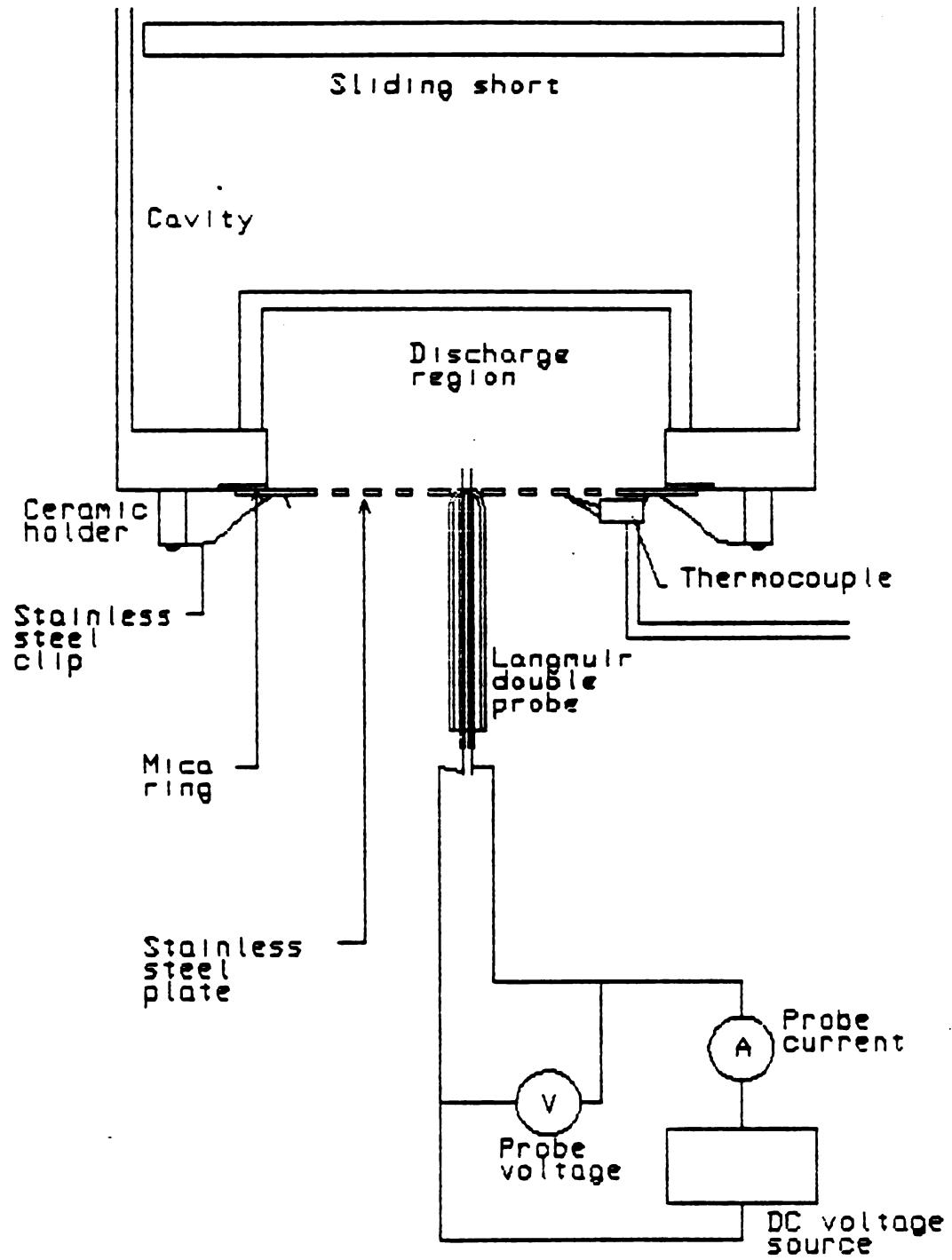


Figure 4.14 Langmuir Probe and Electrical Circuit

positive probe moves close to the plasma potential and collects more electrons. The negative probe moves away from the plasma potential and collects fewer electrons. The excess electrons flowing to the positive probe pass through the system's circuit to make up the deficiency at the negative probe. As the voltage of one probe is made somewhat more negative, the positive probe moves still closer to the space potential and collects the entire electron current since the other probe is now so highly negative that virtually no electron can reach it. Up to a certain point, further increase in the voltage can cause no additional change because the positive probe collects a sufficient electron current to balance the entire positive ion current flowing to the system. This state can be referred to as a state of saturation.

In practice there is no complete saturation, but a slower and steady increase of the net current going through the system as the voltage is further increased appears on the current versus voltage characteristics. This deviation from the theory can be explained by the fact that the method uses the assumption of stationary positive ions in the plasma due to their heavier mass relative to the electrons. In fact the positive ions are not stationary, but move with a smaller velocity due to their lower mobility. As the voltage of one probe is made increasingly more negative, the number of ions reaching that probe will increase accordingly. The symmetry of the system will cause it to

reverse these results when the voltage between the two probes is inverted. A typical current versus voltage data is shown in Figure 4.15.

The electron temperature is determined by a logarithmic plot method. Since the net current to the system must be zero, we have

$$i_{i1} + i_{i2} = I_p = i_{e1} + i_{e2} \quad (4.3)$$

where i_{i1} and i_{i2} are the positive ion currents to probe 1 and 2 respectively, i_{e1} and i_{e2} are the electron currents and I_p is the total current collected on both probes. Substituting i_{e1} and i_{e2} in terms of the Boltzmann relation, we obtain

$$I_p = I_{01} e^{-\phi v_1} + I_{02} e^{-\phi v_2} \quad (4.4)$$

where $I_{01,2}$ are the electron currents reaching the respective probes when the voltage applied is zero. These electrons constitute the high energy tail of the distribution. v_1 and v_2 are the voltages of probes 1 and 2 respectively and $\phi = e/kT_e$.

Looking at the voltages, we have

$$v_1 - v_2 = v_d + v_c \quad (4.5)$$

Where v_d is the potential applied and v_c represents any small difference in plasma potential which may exist between the regions surrounding the probes plus the contact potentials acting in the system. In all the measurements

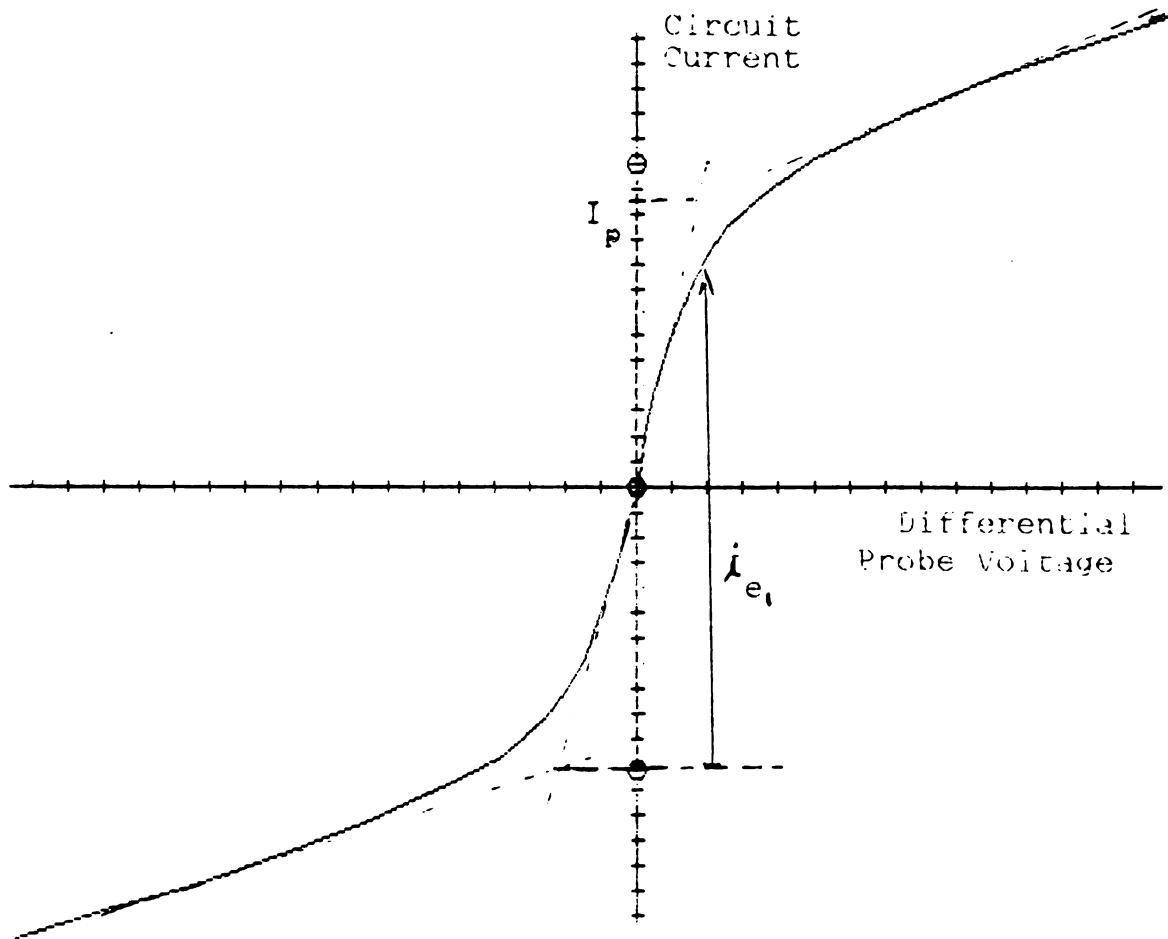


Figure 4.15 Typical Langmuir Probe Current-Voltage Characteristics

related to this thesis v_c is very small and would be significant only if the probes were separated by a large distance, or if the plasma potential was highly variable. Equation (4.5) can be written as

$$v_1 = v_2 + v_d + v_c \quad (4.6)$$

substituting in (4.4) and dividing by i_{e2}

$$\frac{I_p}{i_{e2}} = \left(\frac{I_{01} e^{-\phi v_1}}{I_{02} e^{-\phi v_2}} \right) + 1 \quad (4.7)$$

rearranging (4.7) and taking the natural log

$$\ln\left[\left(\frac{I_p}{i_{e2}}\right) - 1\right] = -\phi v_d + \ln(\alpha) = \ln(\Gamma) \quad (4.8)$$

where

$$\Gamma = \left(\frac{I_p}{i_{e2}}\right) - 1 \quad \text{and} \quad \alpha = \left(\frac{I_{01}}{I_{02}}\right) e^{\phi v_d} \quad (4.9-10)$$

The plotting of $\ln(\Gamma)$ versus v_d should yield a straight line whose slope is a measure of the electron temperature.

The plasma density is obtained from the ion current density

$$J_i = N_i e v_i \quad (4.11)$$

where v_i is the average ion velocity near the probe and N_i is the ion density. An estimate of this ion current density was given by Bohm^{26,58}

$$J_i = 0.6 N_i e \left(\frac{kT_e}{m_i}\right)^{\frac{1}{2}} \quad (4.12)$$

where k is the Boltzmann constant, T_e is the electron temperature and m_i is the ion mass. This expression for the ion current density takes into account the effect of the

plasma sheath potential around the probe. The ion density can be derived from equation (4.11)

$$N_i = \frac{i_p}{0.6 e A_s} \left(\frac{m_i}{kT_e} \right)^{\frac{1}{2}} \quad (4.12)$$

where i_p is the ion saturation current falling on one probe, m_i is the ion mass, T_e is the electron temperature and A_s is the sheath area surrounding the probe. An estimation of this sheath area is given in Reference⁵⁷. In practice i_p is read from the probes voltage current characteristic. It corresponds to the bend in the current voltage curve as shown in Figure 4.15.

It should be noted that this method involves a number of approximations, and therefore should be expected to have some limitations. In particular, the assumption that the electrons have a Maxwellian distribution is important since the probes collect primarily electrons in the high energy end of the distribution. A limitation of this method is to be expected when the electron distribution deviates strongly from the Maxwellian distribution. The result of this is observed as a deviation of equation (4.8) from a linear curve.

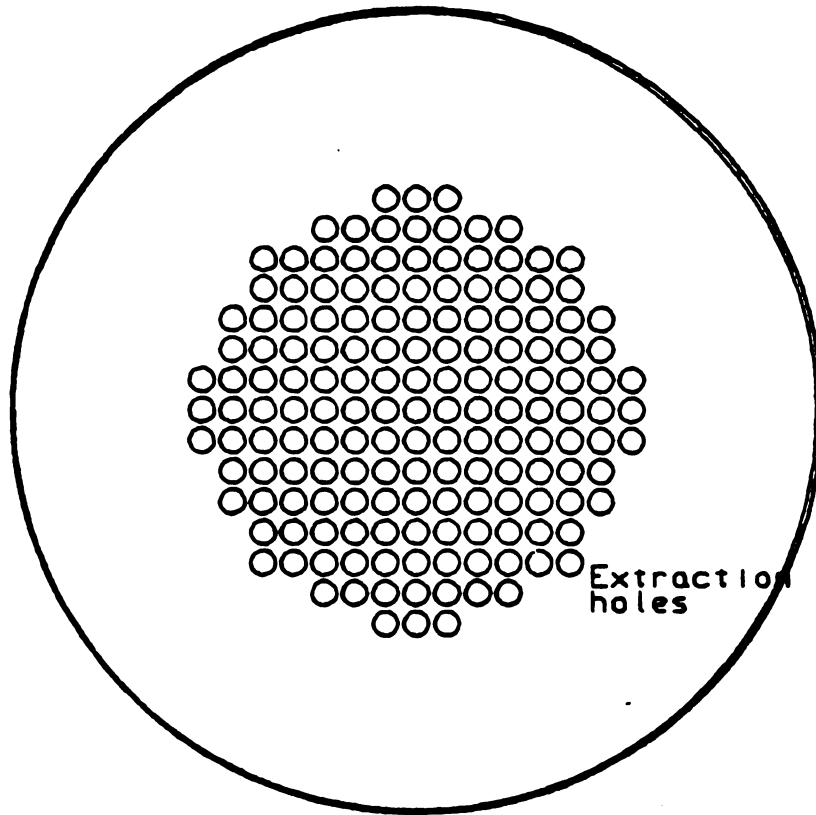
A cross section of the experimental system used to measure the plasma density and the electron temperature is shown in Figure 4.14. It consists of a double Langmuir probe described earlier. This probe is held, along the axis of the cylindrical discharge, by a metal tube connected to a

thin perforated stainless-steel plate that forms the bottom end of the discharge chamber. The brass plate has 220 holes 1.6 cm in diameter positioned in a circular pattern with a 5.5 cm diameter. The vertical position of the double probe can be adjusted to expose only the uncovered portion of the tungsten probes to the plasma in a region where the microwave fields are small or inexistant, thus minimizing errors in measurements due to perturbations of the discharge and radiations caused by the microwave fields. In all the measurements the plane containing both probes is oriented perpendicular to the coupling probe axis. The discharge temperature is assumed to be equal or close to the discharge walls temperature which is measured with a thermocouple attached to the lower side of the perforated stainless-steel plate. This plate is thermally isolated from the water cooled cavity end plate by means of a mica ring. The probes are connected to the output of a variable voltage DC source from which the current and voltage are measured. The data was taken manually by varying the voltage between the probes and recording the current collected by the probes. The data was then analyzed by a computer program, written by J. Hopwood, which allows a fast determination of the saturation currents for each probe and a consistent calculation of the electron temperature and electron density.

4.3.4 EXTRACTION GRIDS

Two ion extraction systems are used in this experiment, a double grid system and a single grid system. The single grid system is shown in Figure 4.16, it consists of a 0.5 mm thick stainless steel plate. The side of this plate exposed to the plasma is coated with a thin silicon layer for electrical isolation. This plate has 220 extraction holes 1.6 mm in diameter positioned in a circular pattern with a diameter of 5.5 cm. The total extraction area of this single grid is 4.42 cm^2 which corresponds to a 18.6% geometric transparency. In this configuration the metal plate is biased negative with respect to ground while the cavity is biased positive with respect to ground.

The double grid assembly shown in Figure 4.17 consists of a 0.46 mm thick screen grid with a circular extraction area 2.54 cm in diameter, and a 1.6 mm thick acceleration grid. Both grids are made of a carbon graphite material to minimize erosion. The system has a total of 120 coaxial circular extraction holes. The diameter of these holes is 2 mm for the screen grid and 1.6 mm for the acceleration grid. The optimum separation between the two grids is 1 mm. For the screen grid the total area of the extraction holes is 3.8 cm^2 which corresponds to a 77% transparency. The acceleration grid has a total open area of 2.4 cm^2 corresponding to a transparency of 49%. In this system the



Single grid top view

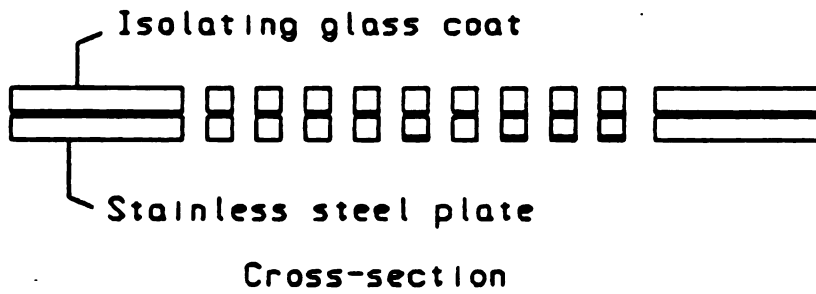


Figure 4.16 Single Grid

screen grid is biased positive with respect to ground and the acceleration grid is biased negative with respect to ground.

For both extraction systems a tungsten filament is used to neutralize the ion beam by electron thermal emission. This filament is positioned approximately 1 cm downstream from the acceleration grid. The theoretical basis for this kind of ion beam extraction is Child's law

$$J = \left(\frac{4\epsilon_0}{9}\right) \sqrt{\frac{2q}{m_i}} \left(\frac{V^2}{l^2}\right)^{\frac{3}{2}} \quad (4.13)$$

where J is the maximum current density between two parallel plates, ϵ_0 is the free space dielectric constant, V is the potential difference and l is the spacing between the two grids. q/m_i is the charge to mass ratio of the accelerated particles.

For the case of the double grid system a stable plasma sheath is formed around each screen hole as shown in Figure 4.18. This sheath is a space charge limited emissive surface of positive ions. The ions reach the sheath and are accelerated by the strong electric field between the positive sheath and negative accelerator grid hole. It was found⁵⁹ that Child's law is in a fairly good agreement with the results of the ion current extracted with such a system, provided the separation l is replaced by the effective acceleration length l_e shown in Figure 4.19. Ion focusing effects occur in two regions of the accelerator system: between the grids and just upstream of the grids. In these

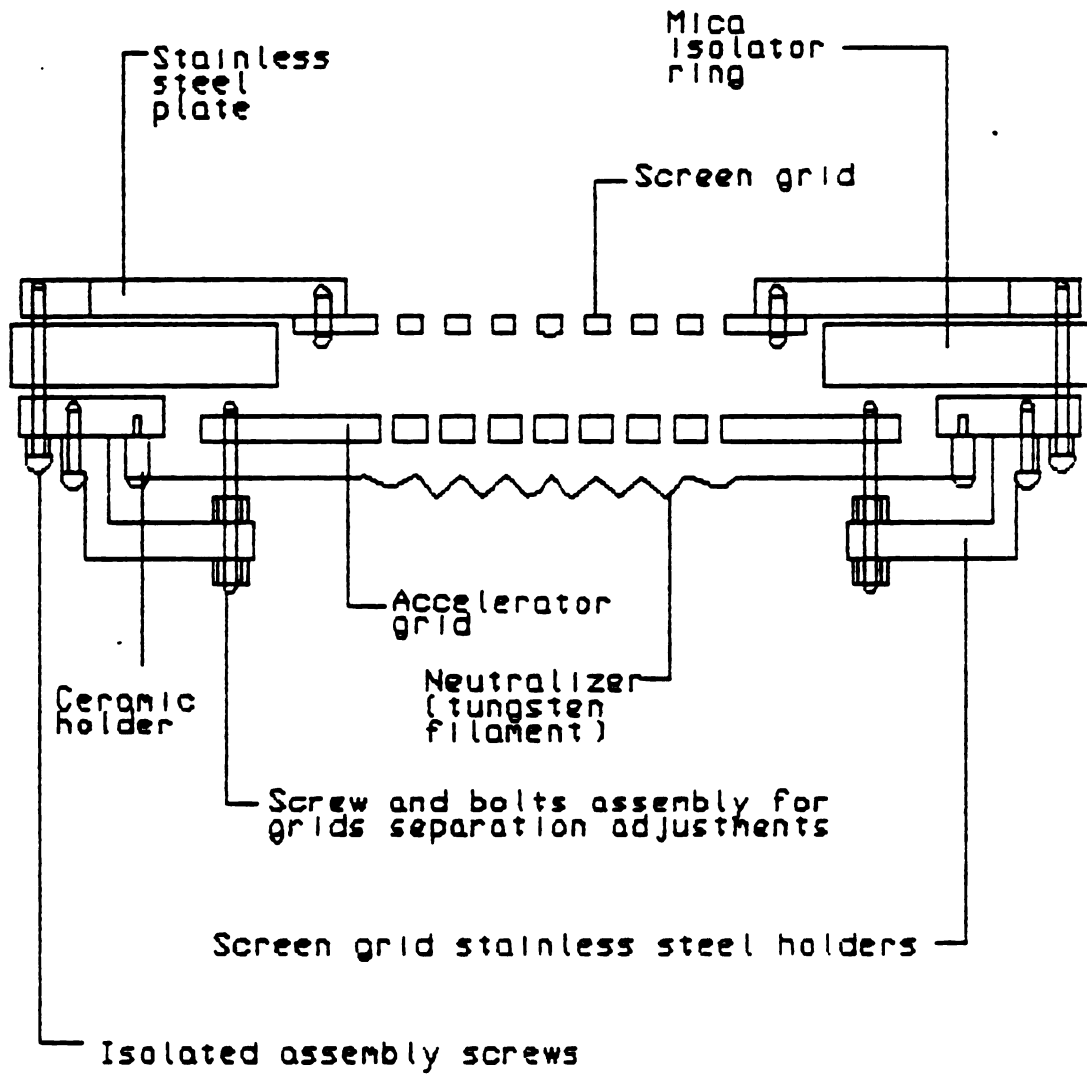
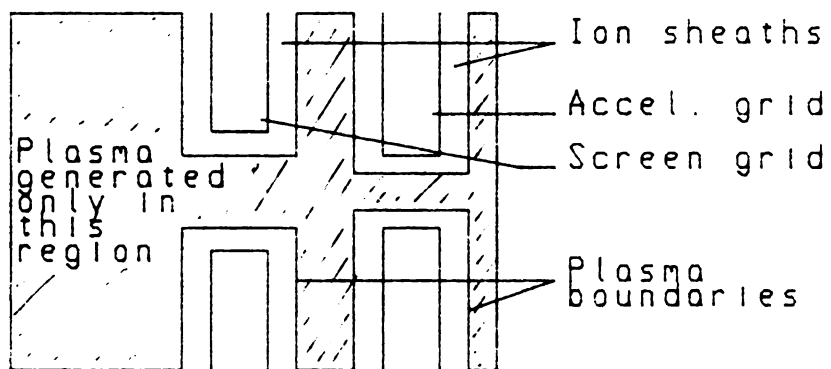
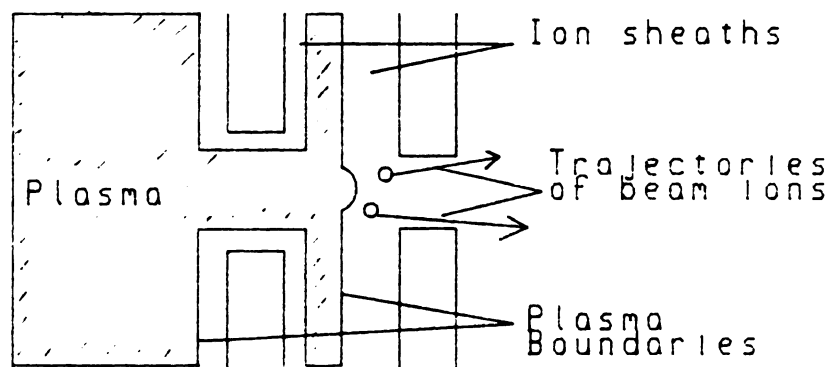


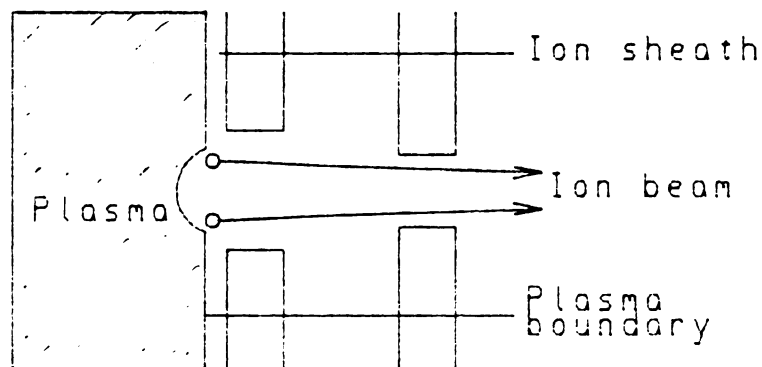
Figure 4.17 Double Grid Assembly



(a) NO ACCELERATION VOLTAGE

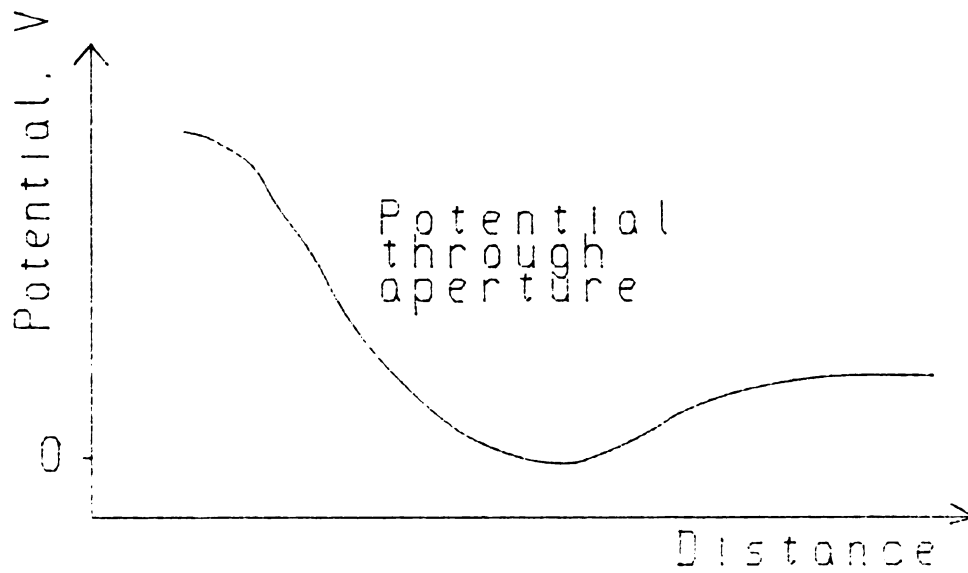
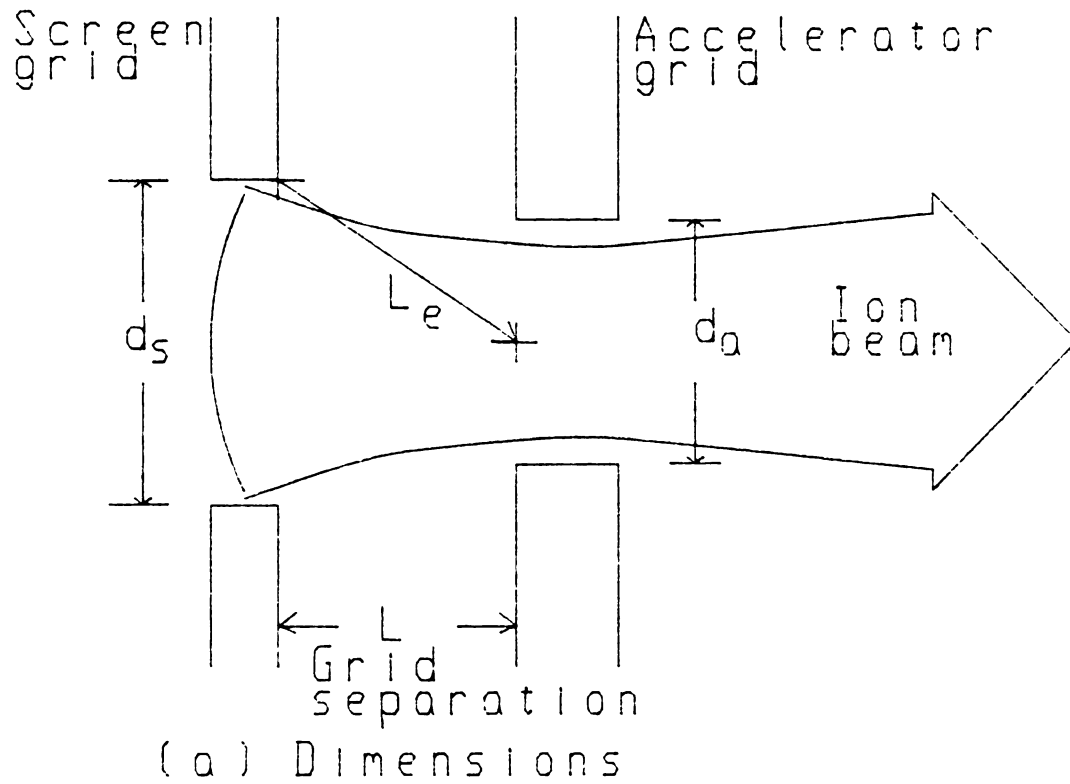


(b) INTERMEDIATE ACCEL. VOLTAGE



(c) NORMAL ACCEL. VOLTAGE

Figure 4.18 Plasma and Ion Sheath Near the Grids Apertures



(b) Potential variation between grids

Figure 4.19 Double Grids Dimensions and Potential

regions the ions tend to follow the electric field lines passing from the screen grid hole through the accelerator grid hole. The important aspect of a double grid system design is to shape these electric field lines to achieve a good focusing and a maximum ion beam density.

A comprehensive experimental investigation of two-grid accelerator systems is found in Reference⁶⁰. In this work a wide range of geometrical grid parameters and grid set operating conditions were investigated for their effect on ion beam divergence. Other investigations⁶¹ showed that three-grid accelerator systems offer significant improvements in ion beam focusing over two-grid systems. A three-grid system is similar to a two-grid system except that a third grid which is spaced as close as practically possible to the accelerator grid, is added downstream from the beam and is biased to decelerate the ions. The hole diameter in this deceleration grid is about 25% larger than the accelerator hole diameter.

The effect of electrodes misalignment and ion current variations on the beam thrust from a single aperture of a two-grid system have been investigated using a computer simulation⁶². In this investigation four types of perturbations have been considered: changes in ion emission rate, changes in axial spacing of the electrodes, transverse misalignment and tilt between the electrodes. It was found that apart from the changes in the ion emission rate, the dominant effect on the thrust was caused by the axial

changes in the electrodes spacing. The other perturbations were found to have negligible effects on the thrust or ion beam extraction.

4.3.5 VOLTAGE EXTRACTION SYSTEM

The high voltage circuit used for ion extraction is shown in Figure 4.20. It consists of two high voltage power supplies connected in series. The positive terminal of this power supply combination is connected to the metallic cavity base plate. The negative terminal is connected to the metal part of the single extraction grid for the case when a single grid is used or to the acceleration grid for double grid operation. The electrical ground is connected between the two power supplies to allow two ammeters to separately read the electrical currents flowing through each power supply. The cavity is isolated from the ground potential by means of a DC radial choke (24). The beam neutralization system consists of a tungsten filament (23) placed downstream from the extraction grids and connected to the terminals of a high current power supply. The positive terminal of this power supply is connected to ground potential through an ammeter that measures the electron current extracted from ground and thermally emitted through the heated tungsten filament. The vacuum system below the bell-jar is also connected to ground potential.

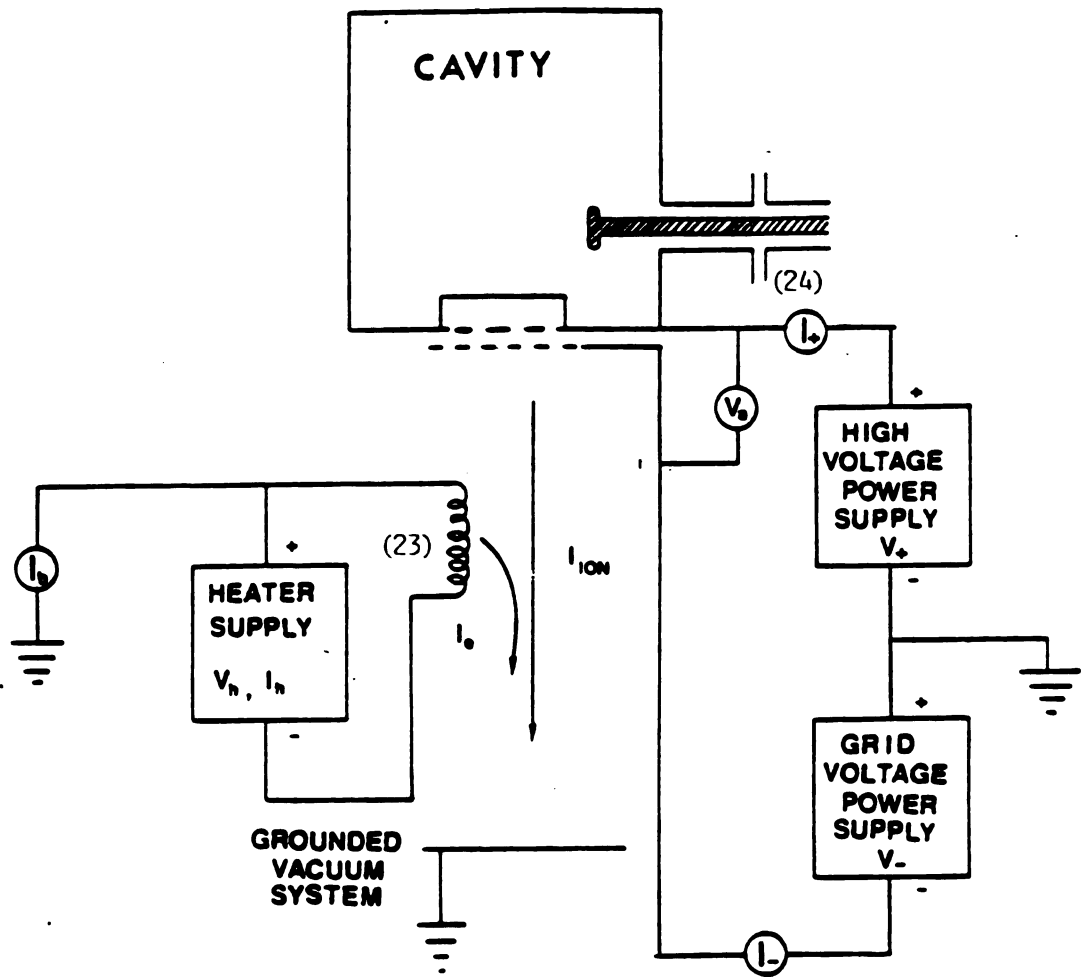


Figure 4.20 Electrical Circuit for Ion Beam Extraction

The measured voltages and currents are labeled as follow:

V_+ , I_+ = voltage and current between ground and the cavity base plate and screen grid.

V_- , I_- = voltage and current between the single grid or the acceleration grid and ground.

V_h , I_h = voltage and current applied to the neutralizer tungsten filament.

I_b = current flowing from the neutralizer to ground.

The electron and ion currents involved in the ion extraction system are shown in Figure 4.21 where

i_{e1} = electron current flowing from the gas discharge to the cavity base plate and screen grid.

i_{e2} = electron current flowing from the gas discharge to the bell-jar environment.

i_{e3} = electron current backstreaming from the bell-jar environment to the cavity base plate.

i_{e4} = electron current emitted from the neutralizer.

i_{i1} = ion current extracted from the gas discharge through the grids.

i_{i2} = ion current collected by the acceleration grid.

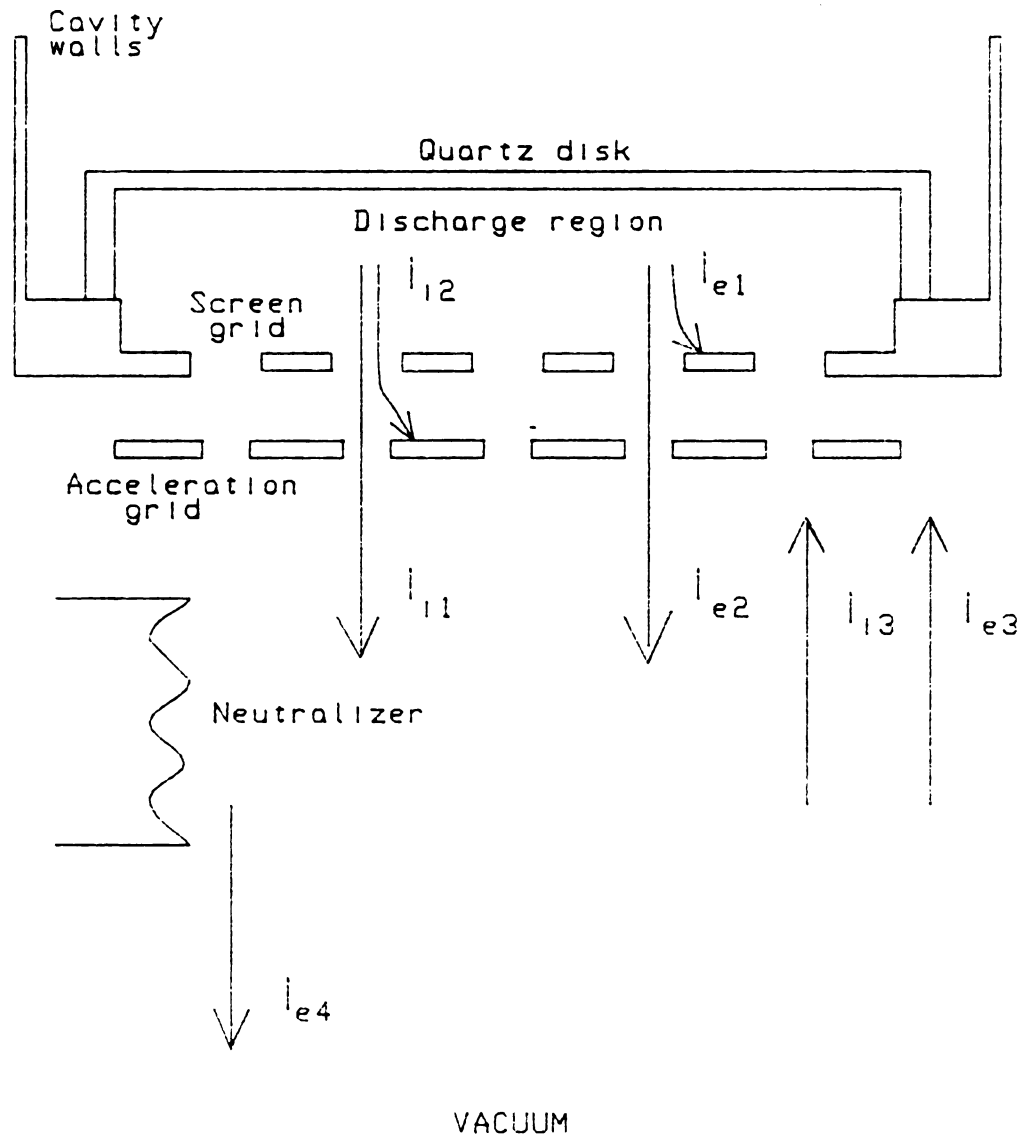


Figure 4.21 Electron and Ion Currents Involved in Ion Beam Extraction

i_{i3} = ion current backstreaming to the base plate
and acceleration grid.

During an ion extraction operation the cavity base plate and the screen grid are held at a high potential relative to ground ($1600 \text{ V} > V_+ > 300 \text{ V}$). The single grid or the acceleration grid are biased negatively relative to ground potential ($-200 \text{ V} < V_- < 0 \text{ V}$). This voltage bias minimizes some of the electron and ion currents. For example i_{e2} and i_{i3} can be neglected at very low pressures. The current i_{i3} cannot be neglected at bell-jar pressures higher than 1 mTorr since the ions in the bell-jar have a higher probability to collide with neutral particles and return to the negatively biased acceleration grid.

A metal screen, shown in Figure 4.22 is placed below the base plate and biased with the same potential as the acceleration grid to prevent the electrons emitted by the neutralizer from reaching the positively biased base plate, thus minimizing i_{e3} .

The rest of the currents are accounted for by the ammeters in the extraction system as follow:

$$i_{e1} = I_+ \quad (4.14)$$

$$i_{i2} = I_- \quad (4.15)$$

$$i_{e4} = i_{e1} - i_{i2} = I_b \quad (4.16)$$

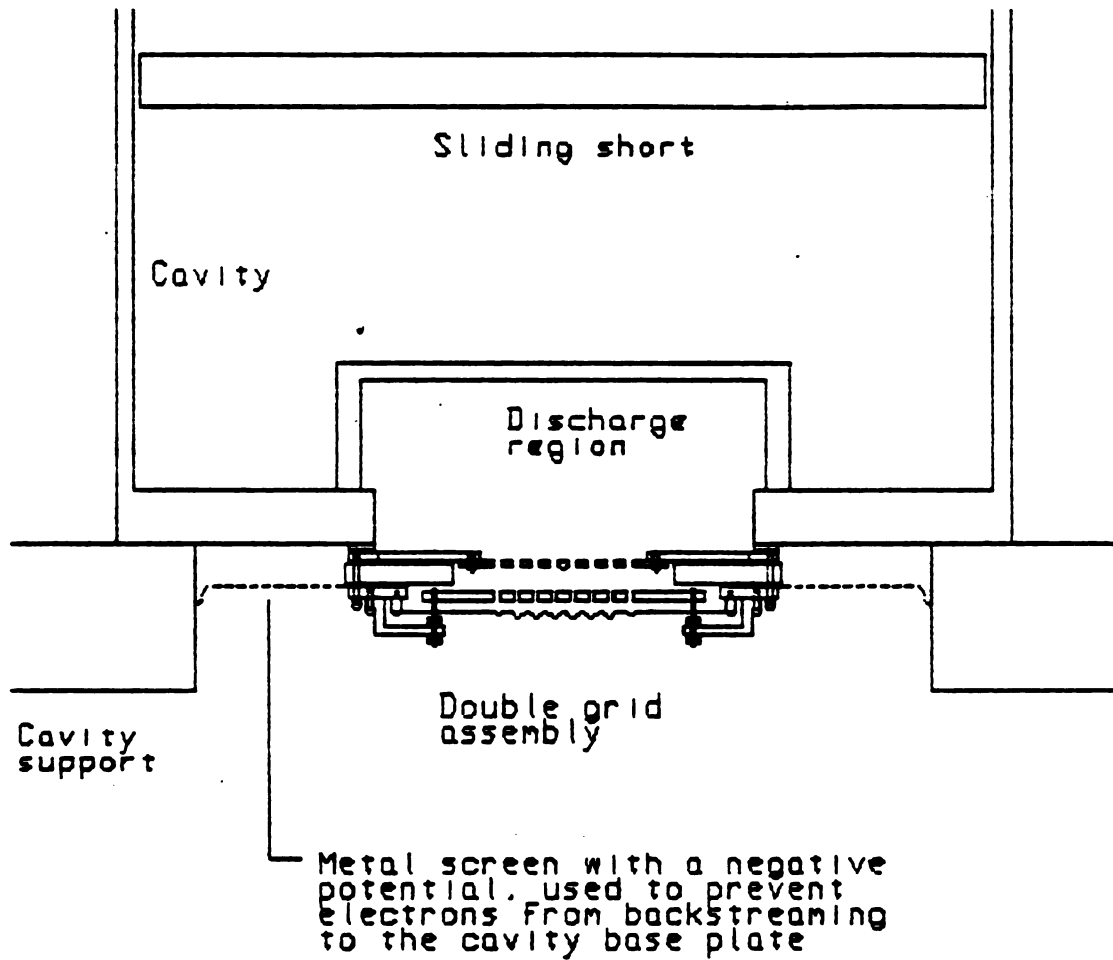


Figure 4.22 Cross Sectional View Showing the Double Grid Assembly and the Shielding Metal screen

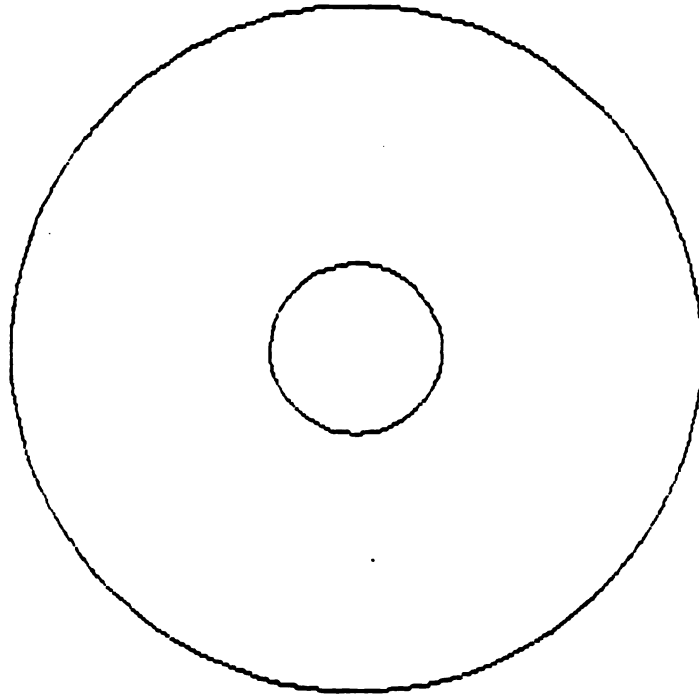
then

$$I_b = i_{i1} \quad (4.17)$$

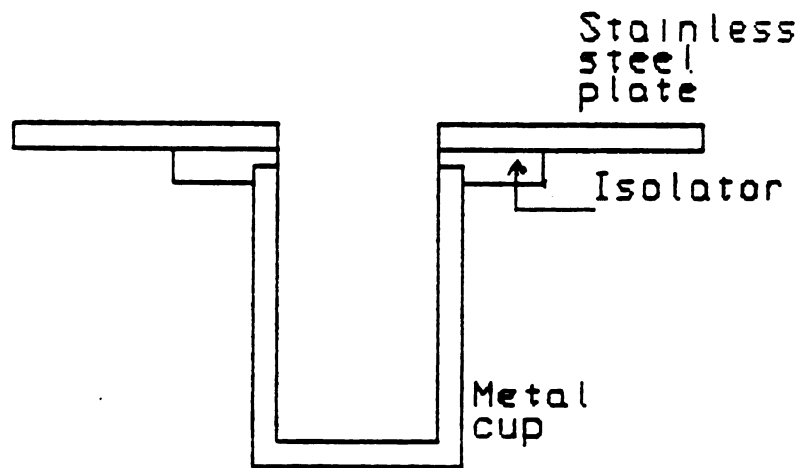
As shown in these equations the ion beam current i_{i1} can be deduced from a balance of the measured currents. This is done in practice by adjusting the tungsten filament voltage V_h and current I_h so that the electron emitted current I_b is made equal to the difference ($I_+ - I_-$). When this currents balance is achieved, the ion beam current can be read directly from an ammeter. This method however, does not indicate how well the ion beam is focused. For this reason a Faraday cup was added to the system.

4.3.6 FARADAY CUP

A cross-section of the Faraday cup used in these experiments is shown in Figure 4.23. It consists of a cylindrical aluminum cup 2.54 cm in diameter and 2.5 cm high. The outer surface of the cup is shielded from the ion beam by means of a 1.6 mm thick circular stainless steel plate positioned on top of the cup. This stainless steel plate has a diameter of 15 cm and a 2.54 cm diameter circular hole at the center. The cup is electrically isolated from the plate by an insulating ring. The Faraday cup assembly was positioned about 30 cm downstream from the



(a) Top view



(b) Cross section

Figure 4.23 Faraday Cup

grids on a movable cart driven by a small electric motor, allowing the cup to be accurately centered on the ion beam axis.

The stainless steel plate is held at ground potential while the cup is biased negative with respect to ground to collect ions and repel electrons.

This Faraday cup was used to control the ion beam collimation and to confirm the ion beam current measurements, thus no explicit measurements involving the Faraday cup are presented in this dissertation.

For the double grids, the focusing of the ion beam can be controlled by the magnitude of the negative voltage applied to the acceleration grid. The negative voltage controls the ion optics between the grids which affects the beam collimation. The ion beam focusing can be monitored by positioning the Faraday cup around the beam axis and as close as possible to the acceleration grid. In this location, the current collected by the Faraday cup is maximum when the beam is focused since the beam divergence is minimized.

The experimental results showed that for screen grid voltages higher than 800 V, the proper acceleration grid voltage, for optimum beam focusing, is approximately -50 V. It was also found that the optimum acceleration voltage

depends on the magnitude of the ion beam current extracted. Experimental measurements obtained with the Faraday cup also confirmed the accuracy of the method used to measure the value of the ion beam current.

CHAPTER V

EXPERIMENTAL MEASUREMENTS

5.1 INTRODUCTION

This chapter presents the experimental measurements performed to characterize microwave discharges and the extracted ion beams under different experimental conditions. Argon and oxygen gases were used in these experiments. In Section 5.2 applicator I is used without static magnetic field, and the measurements for electron density, electron temperature and extracted ion beam currents are presented for different experimental conditions where gas flow rate, pressure, microwave input power and extraction voltages are varied. In Section 5.3 Applicator I is retrofitted with rare earth magnets to allow an initial investigation of the effect of a multicusp static magnetic field on the microwave discharge. Only ion beam extraction results are presented in Section 5.3 since the applied static magnetic field introduces errors in the double probe electron density and electron temperature measurements. Section 5.4 presents the results of the same type of measurements performed with a

new Electron Cyclotron Resonance (ECR) microwave applicator. All experimental results are discussed and summarized in the last section of this chapter.

5.2 APPLICATOR I WITHOUT STATIC MAGNETIC FIELD

5.2.1 EXPERIMENTAL DISCHARGE CONDITIONS

In this experiment applicator I shown in Figure 4.1 was used to characterize a microwave discharge without static magnetic field. The experimental set up is shown in Figure 4.11 and the microwave system diagram is shown in Figure 4.12. Electron density and electron temperature measurements were performed using the double Langmuir probe described in Chapter 4 and shown in Figures 4.13 and 4.14. Ion beam extraction was performed using the single grid and double grid systems described in Chapter 4 and shown in Figures 4.16, 4.17 and 4.20. Three different quartz disks were used to investigate the effects of the discharge chamber volume variation. All quartz disks have a same inside diameter of 9.4 cm, but different heights which are 0.5 cm, 1.8 cm and 4.0 cm corresponding to discharge volumes of 97.2 cm^3 , 187.4 cm^3 and 340 cm^3 respectively and diffusion lengths (defined in Chapter 3 equation (3.81)) of 0.43 cm, 0.79 cm and 1.22 cm respectively. For the calculations of the diffusion lengths and volumes, the

discharge height is the quartz disk height augmented by the base plate thickness which is 0.9 cm for the case of applicator I.

Argon and oxygen gases were used. The discharge pressure was varied from 6×10^{-3} Torr to 0.5 Torr corresponding to a bell-jar (or environmental) pressure variation ranging from 1×10^{-4} Torr to 6×10^{-1} Torr. In the higher discharge pressure range ($p > 3 \times 10^{-2}$ Torr) only the vacuum roughing pump was used whereas for the lower discharge pressures the roughing pump and the diffusion pump were used. The gas flow rate ranged between 20 sccm to 170 sccm. The microwave power was varied from 80 W to 200 W. No static magnetic field was applied to the discharge chamber.

5.2.2 EXPERIMENTAL RESULTS OF ELECTRON DENSITY AND ELECTRON TEMPERATURE MEASUREMENTS.

It was observed that for the TE_{211} mode, the sliding short position L_S and the coupling probe position L_P are dependent on the discharge chamber height, the input microwave power and the discharge pressure. The parameters L_S and L_P along with the cavity tuning procedure are described in Chapter 4.

For argon gas at a pressure of 10^{-2} Torr and a microwave power of 80 W, the sliding short and probe

positions corresponding to the three quartz disks are as follows:

for the 0.5 cm disk $L_S = 7.7 \text{ cm}$
 $L_P = + 0.7 \text{ cm}$

for the 1.8 cm disk $L_S = 7.8 \text{ cm}$
 $L_P = + 1.2 \text{ cm}$

for the 4.0 cm disk $L_S = 8.0 \text{ cm}$
 $L_P = + 1.9 \text{ cm}$

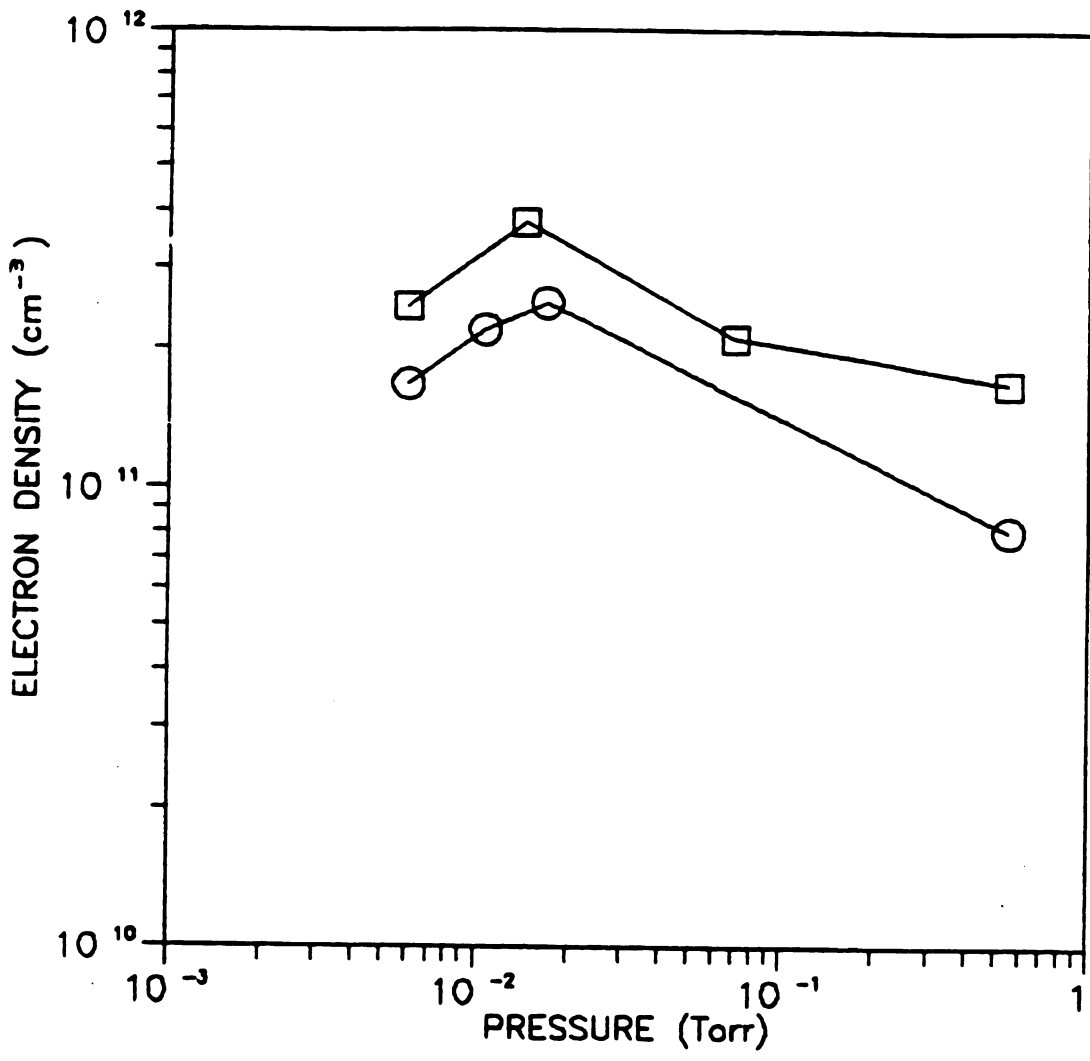
It was also observed that for all these discharge geometries, a power increase of 100 W from 80 W to 180 W corresponds to an increase in the sliding short position L_S of about 0.2 cm, but the coupling probe position decreases by about 0.1 cm.

The same kinds of variations of L_S and L_P are observed when the discharge pressure is increased to about 0.5 Torr. During experimentation it is important to implement such adjustments as one or more discharge parameters are varied so that the optimum power match is always maintained. Reflected microwave power could always be adjusted to be less than or equal to 0.2% of the incident power for the 0.5 cm disk. For the 4.0 cm disk the lower limit of the reflected power was about 1% of the incident power.

Examples of typical experimental measurements of electron density and electron temperature versus discharge pressure for argon discharges are shown in Figures 5.1 and 5.2. The results for the 1.8 cm and the 4.0 cm disks are displayed for a constant input microwave power of 100 W as the discharge pressure is reduced from 0.5 Torr to 6×10^{-3} Torr. Note that for the same input microwave power the electron density obtained with the 1.8 cm disk is higher than the electron density for the 4.0 cm disk. The discharge obtained by using the 0.5 cm disk was harder to tune and maintain at the lower pressures. Thus measurements are not displayed for this diffusion length.

The uncertainties involved in these measurement can only be estimated from the systematic errors since the method used in determining the results is not based on an exact theory. For example the electrons energy was assumed to have a Maxwellian distribution and the effect of the ion sheath is only approximated in the calculations. The relative uncertainties evaluated from repeated measurements are 10% for the electron density and 20% for the electron temperature.

Figures 5.3 and 5.4 show the electron density and electron temperature dependence on the microwave input power for the three quartz disk sizes. These experimental measurements were performed at constant pressure with a varying input microwave power. The discharge pressure was

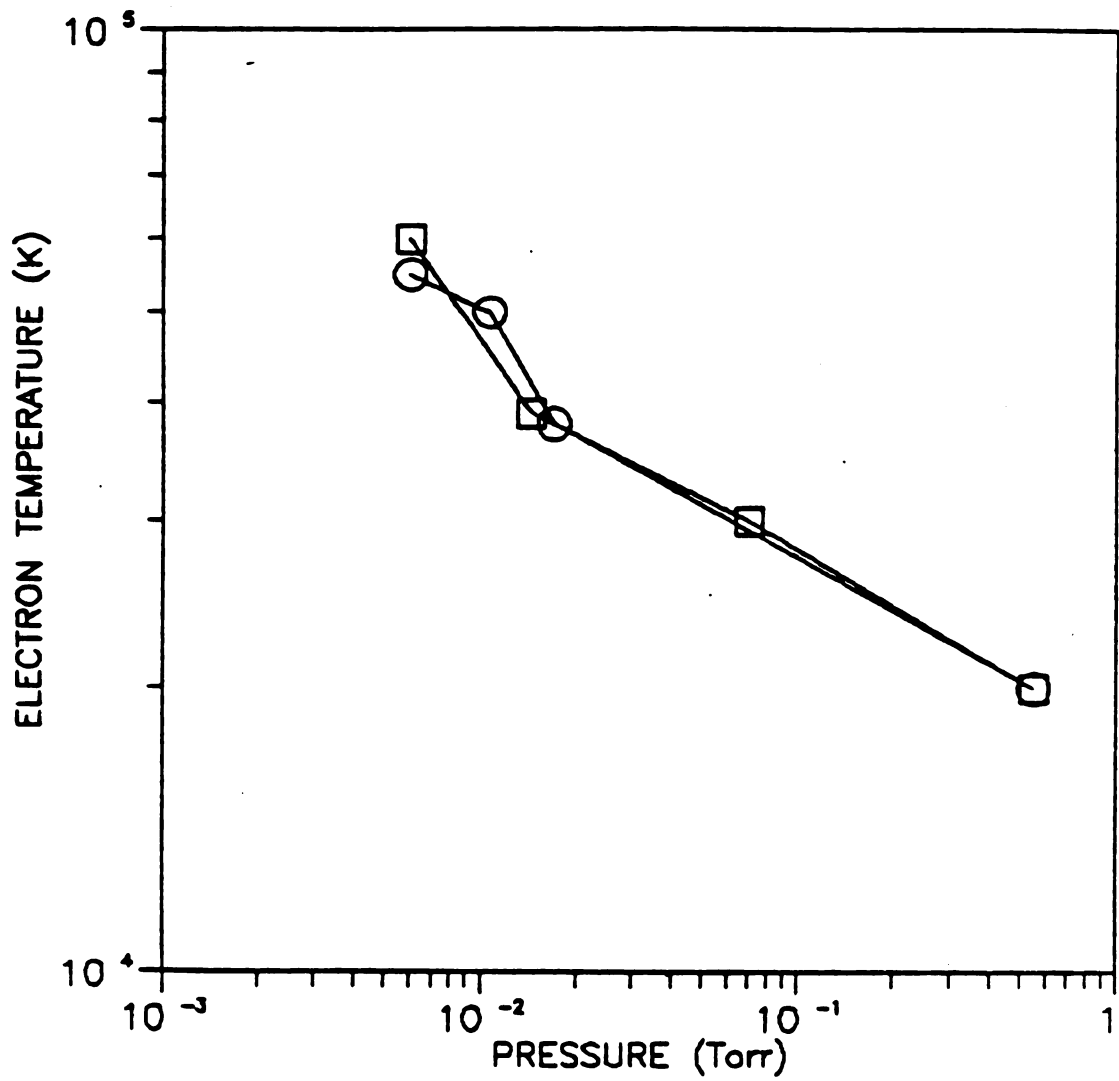


Gas - Argon
 Applicator I
 No Magnets
 Power = 100 W

□ - 1.8 cm Disk, $L_s = 7.8$ cm
 $\Lambda = 0.79$ cm $L_p = +1.2$ cm

○ - 4.0 cm Disk, $L_s = 8.0$ cm
 $\Lambda = 1.22$ cm $L_p = +2.0$ cm

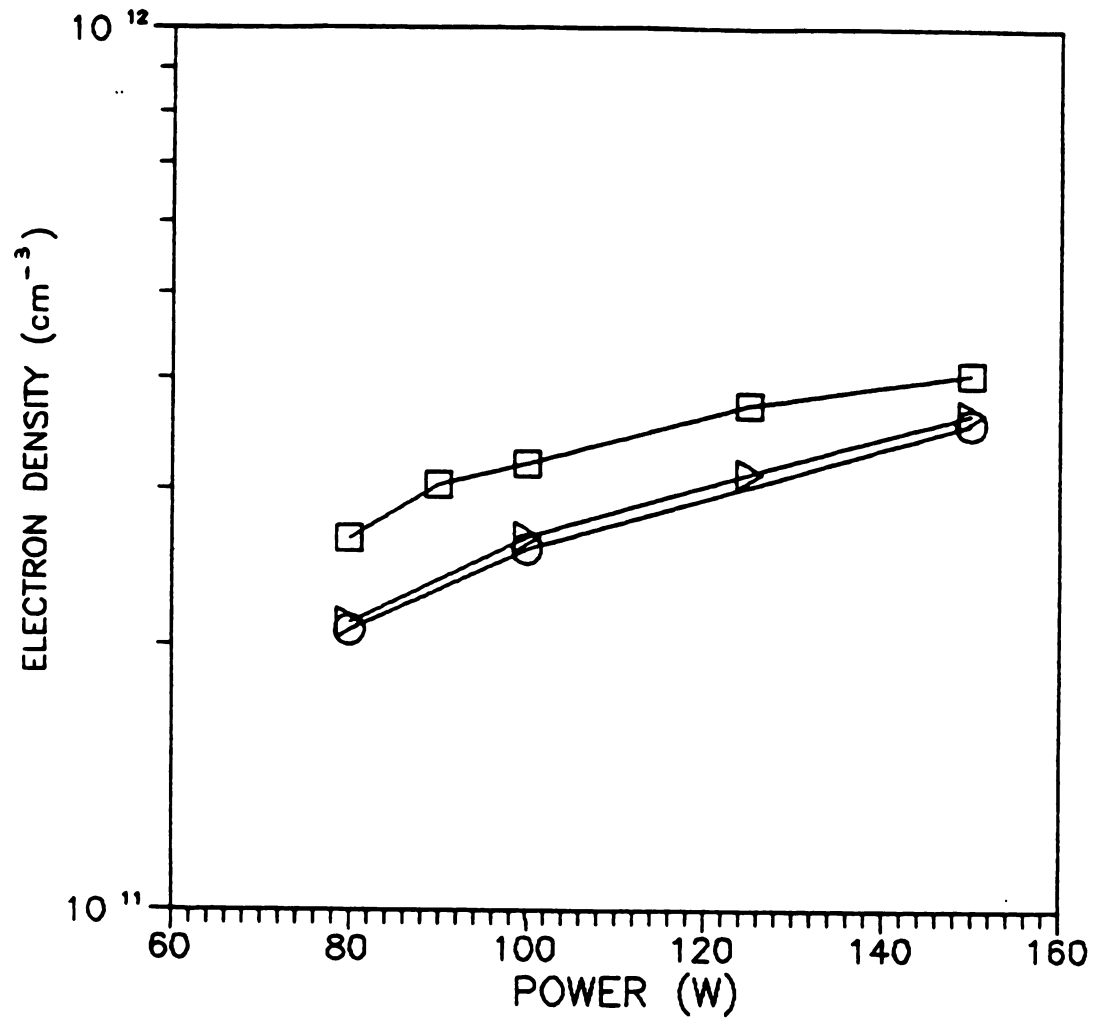
Figure 5.1 Electron Density Versus Discharge Pressure



Gas - Argon
Applicator I
No Magnets
Power - 100 W

□ - 1.8 cm disk
○ - 4.0 cm disk

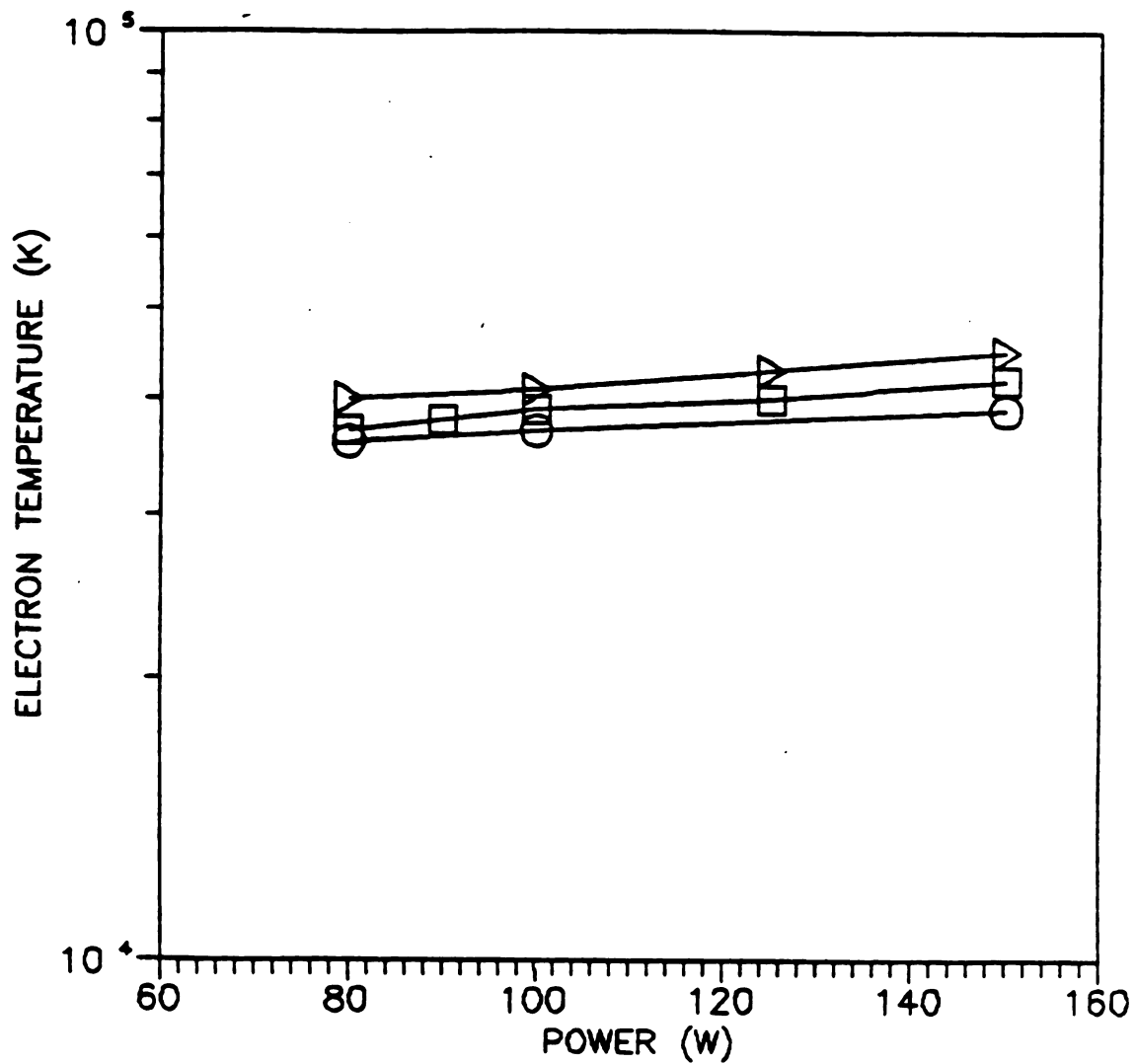
Figure 5.2 Electron Temperature Versus Discharge Pressure For Two Disk Sizes



Gas - Argon
Applicator I
No Magnets
Discharge Pressure = 1.5×10^{-2} Torr

□ - 1.8 cm disk
△ - 0.5 cm disk
○ - 4.0 cm disk

Figure 5.3 Electron Density Versus Input Power For Three Disk Sizes



Gas - Argon
Applicator I
No Magnets
Discharge Pressure - 1.5×10^{-2} Torr

△ - 0.5 cm disk
□ - 1.8 cm disk
○ - 4.0 cm disk

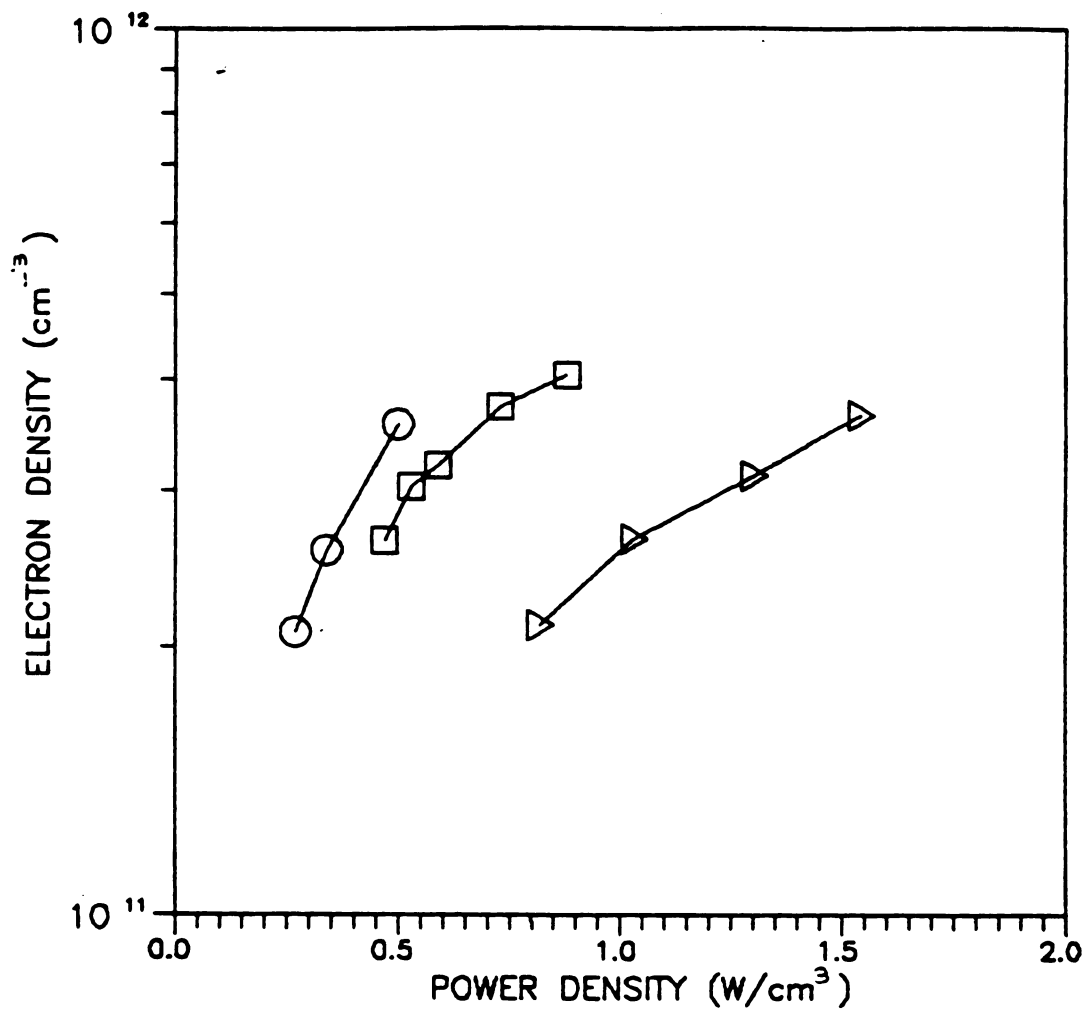
Figure 5.4 Electron Temperature Versus Input Power For Three Disk Sizes

maintained constant at 1.5×10^{-2} Torr and the flow rate was 60 sccm.

Note that an increase of power by a factor of two corresponds to an increase of the electron density by approximately the same factor of two, however the corresponding electron temperature remains relatively unchanged for the same power increase. The smallest disk yields the highest electron temperature but not the highest electron density.

Using the same experimental data shown in Figures 5.3 and 5.4, Figures 5.5 and 5.6 display the electron density and electron temperature versus the microwave input power density for the three quartz disks. The microwave power density is calculated by dividing the input microwave power by the discharge volume in cm^3 .

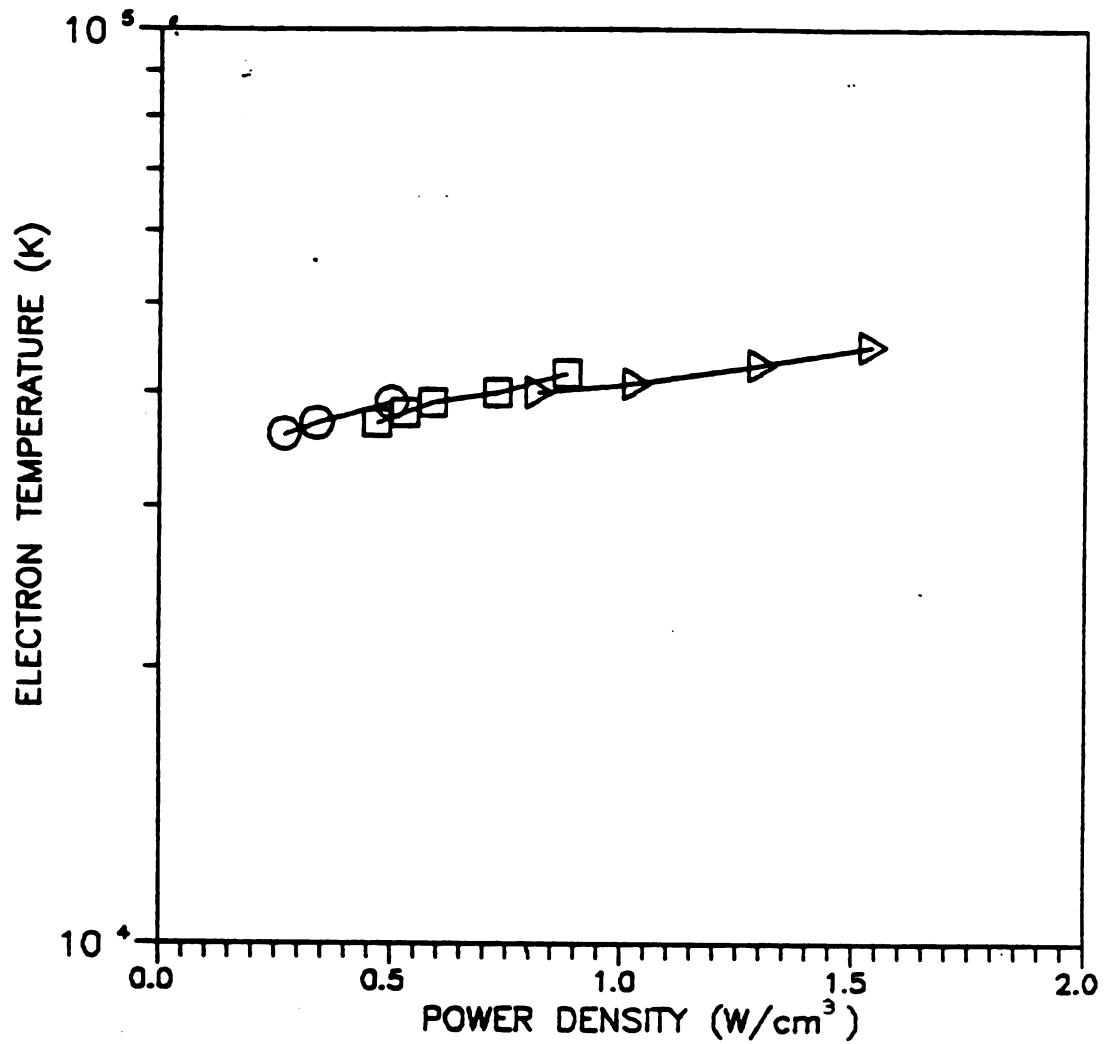
In an attempt to assess the electron density and temperature variation over the cross section of the discharge chamber, a second Langmuir double probe was added to the system. This probe was located 2.5 cm from the cavity axis and centered on the radius passing through the coupling probe axis as shown in Figures 5.7.a and 5.7.b. The plane containing the two tungsten wires of each double probe was oriented perpendicular to the coupling probe axis minimizing any effect that the microwave fields may have on the measurements. Both double probes were also carefully positioned in the vertical direction to expose the same length of tungsten extremities to the plasma. However, an



Gas - Argon
Applicator I
No Magnets
Discharge Pressure = 1.5×10^{-2} Torr

Δ - 0.5 cm disk
◻ - 1.8 cm disk
○ - 4.0 cm disk

Figure 5.5 Electron Density Versus Input Power Density For Three Disk Sizes



Gas - Argon
 Applicator I
 No Magnets
 Discharge Pressure - 1.5×10^{-2} Torr

Δ - 0.5 cm disk
 \square - 1.8 cm disk
 \circ - 4.0 cm disk

Figure 5.6 Electron Temperature Versus Input Power For Three Disk Sizes

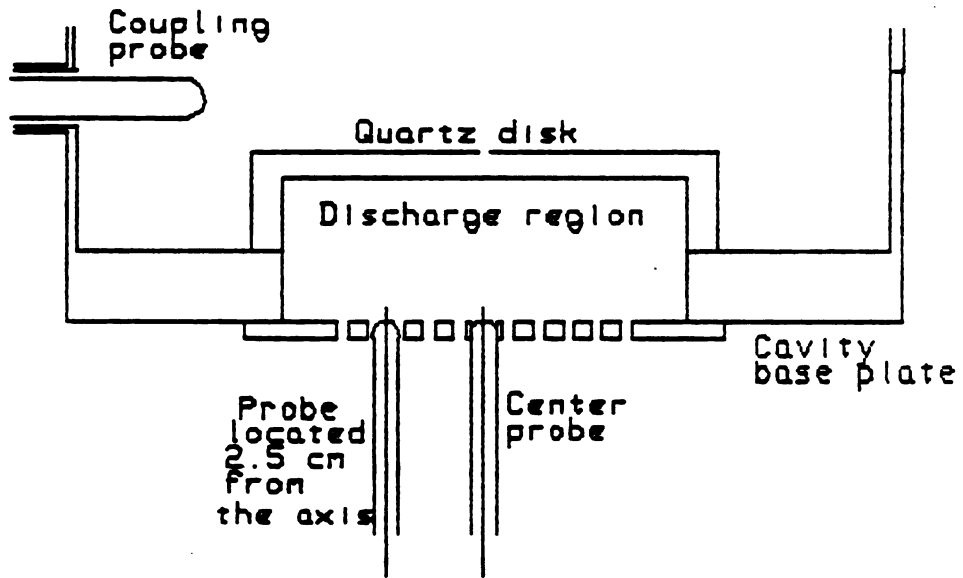


Fig 5.7(a) CROSS SECTIONAL VIEW OF THE TWO DOUBLE PROBES POSITIONS

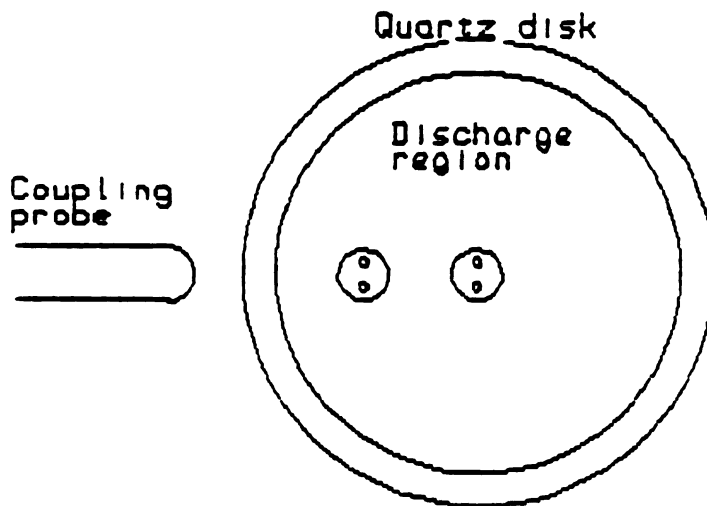
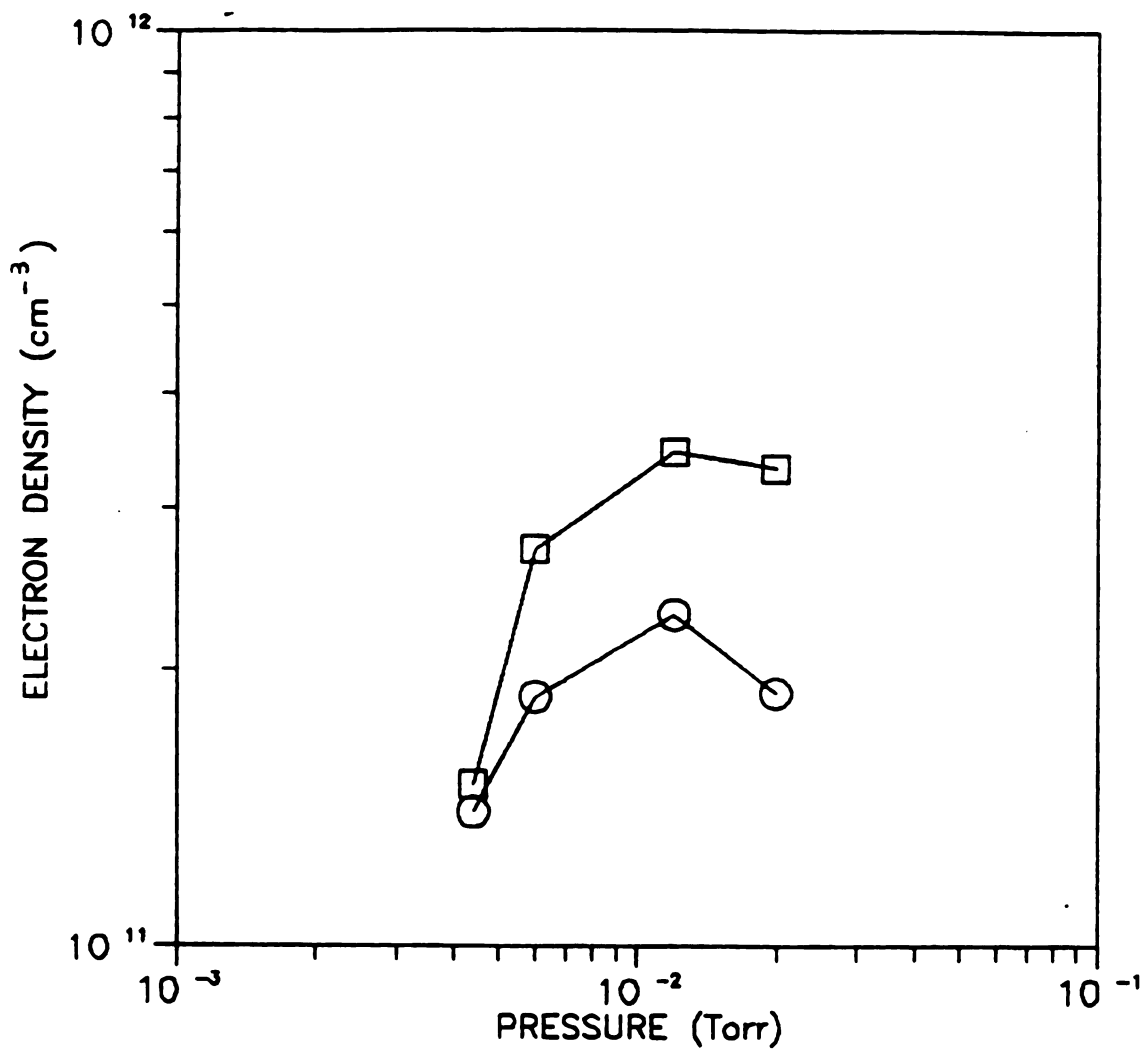


Fig 5.7(b) TOP VIEW SHOWING THE ORIENTATION OF BOTH PROBES RELATIVE TO THE COUPLING ANTENNA

estimated 10% uncertainty in determining the relative position of these probes should be considered due to the systematic errors involved in measuring their exact positions. Here, the plasma is assumed to have the same sheath thickness around both double probes. The same relative uncertainty should be added to the measured electron density since this measured value is proportional to the current collected by each single probe which in turn is proportional to the area of the probes exposed to the plasma.

Experimental measurements obtained with the two double probes are shown in Figures 5.8 and 5.9. The gas used was argon, the input microwave power was 125 W and the quartz dish was 1.8 cm in height. Note that at the higher pressure range the electron density is higher at the center of the discharge, but as the discharge pressure is decreased the measured electron densities converge to approximately the same value. This convergence can be interpreted as a result of longer electron and ion mean free paths at lower pressures and a different diffusion process at lower pressures.

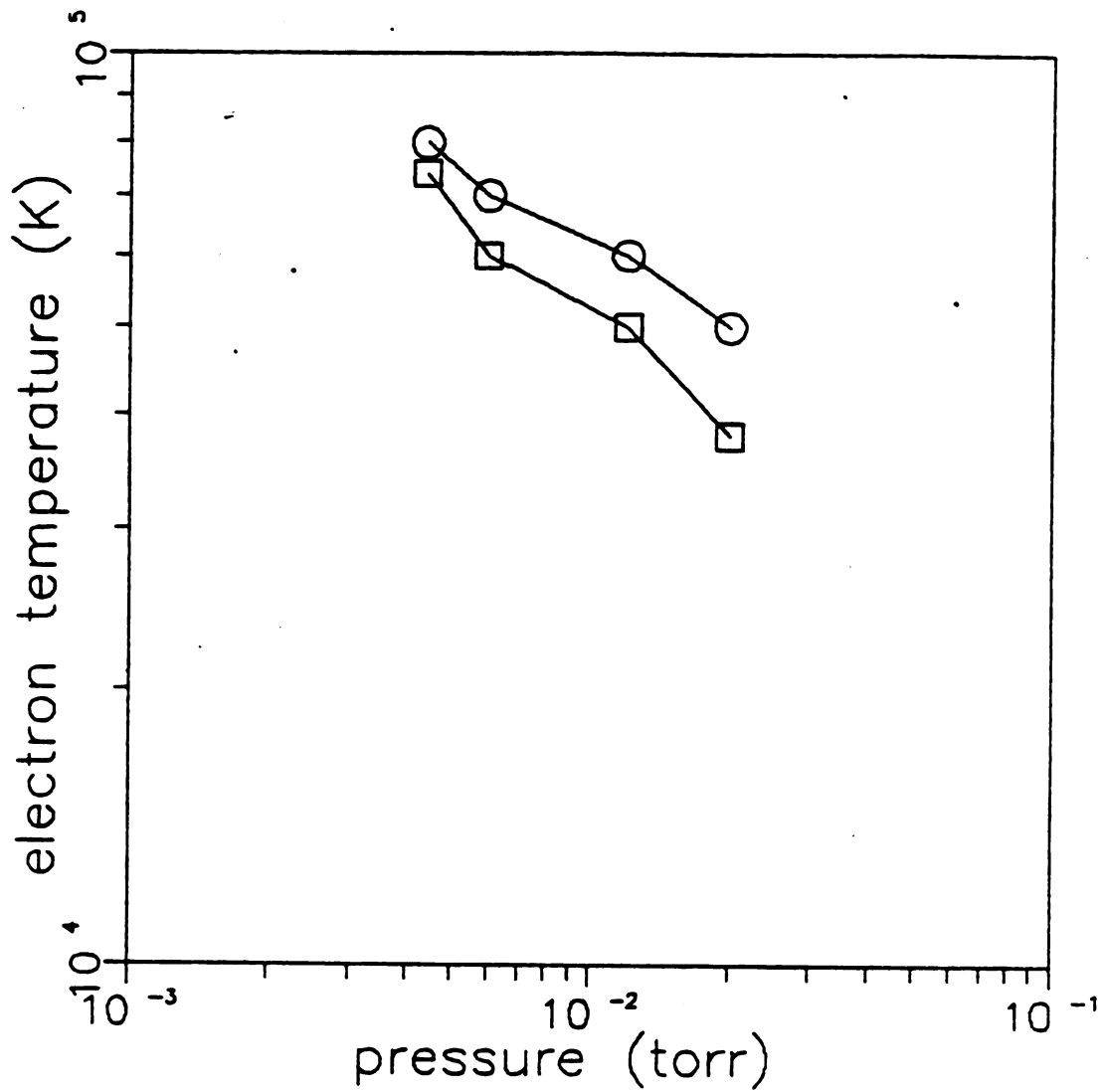
The electron temperature however is lower at the center of the discharge. This can be explained by the fact that the electrons acquire their energy from the electric fields which are higher near the the plasma surface exposed to the microwave cavity through the quartz disk. The amplitude of the electric field is decreased as it penetrate the



Gas - Argon
Applicator I
No Magnets
Power - 125 W
Disk - 1.8 cm

□ - Center Of Discharge
○ - 2.5 cm From Center

Figure 5.8 Electron Density Versus Discharge Pressure In Two Probe Locations



Gas - Argon
Applicator I
No Magnets
Disk - 1.8 cm
Power - 125 W

□ - Center Of Discharge
○ - 2.5 cm From Discharge

Figure 5.9 Electron Temperature Versus Discharge Pressure For Two Probe Locations

discharge since the plasma frequency is higher than the excitation frequency.

The electron plasma frequency ω_{pe} is defined as

$$\omega_{pe}^2 = e^2 N_e / m_e \epsilon_0$$

where e , N_e , m_e are the electron charge, density and mass respectively, ϵ_0 is the vacuum dielectric constant. If N_e is expressed in m^{-3} , the electron plasma frequency becomes

$$\omega_{pe} = 56.4(N_e)^{1/2} \text{ radians/second}$$

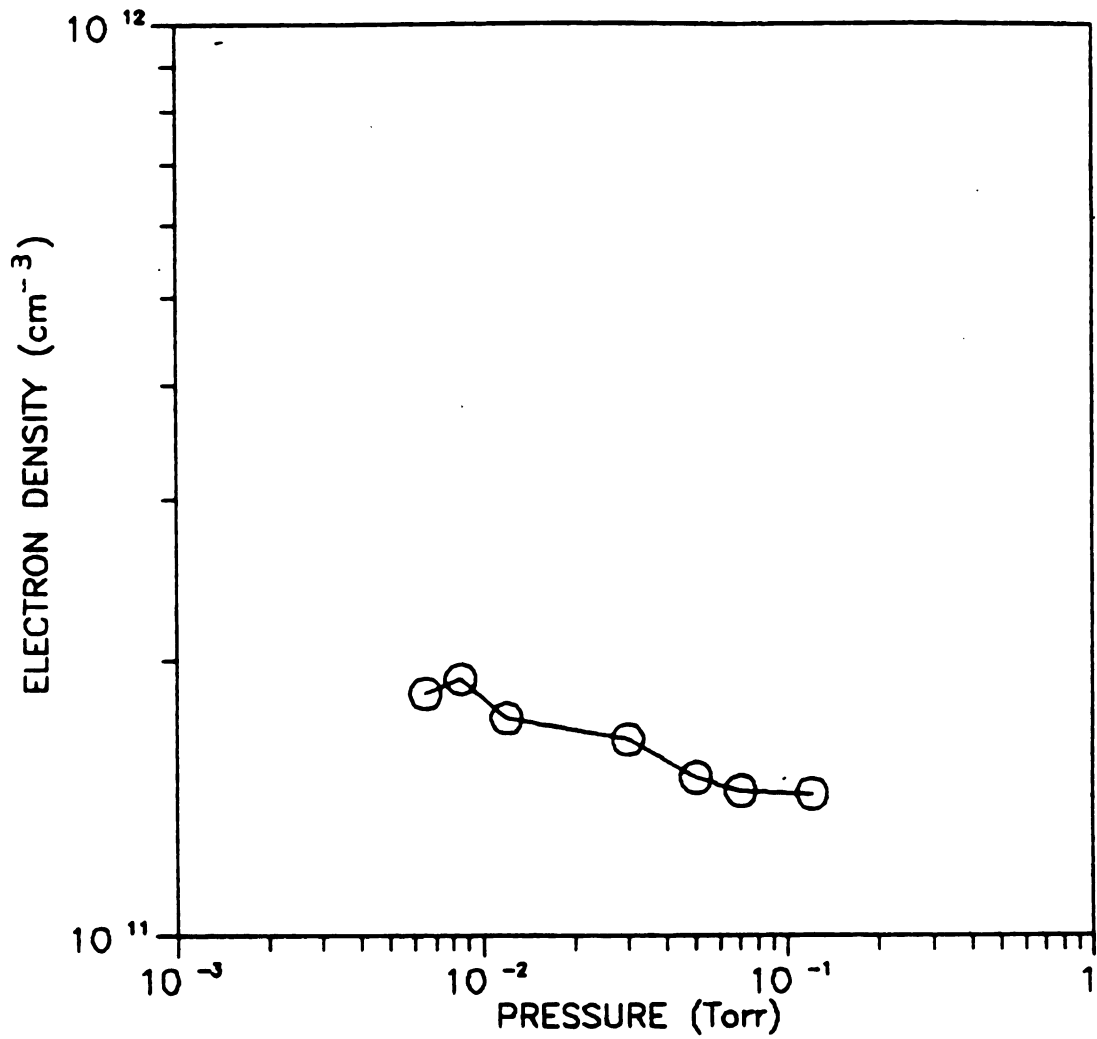
For an electron density of $2 \times 10^{11} \text{ cm}^{-3}$,

$$\omega_{pe} = 2.52 \times 10^{10} \text{ radians/second}$$

or $f_{pe} = 3.98 \times 10^9 \text{ Hz}$

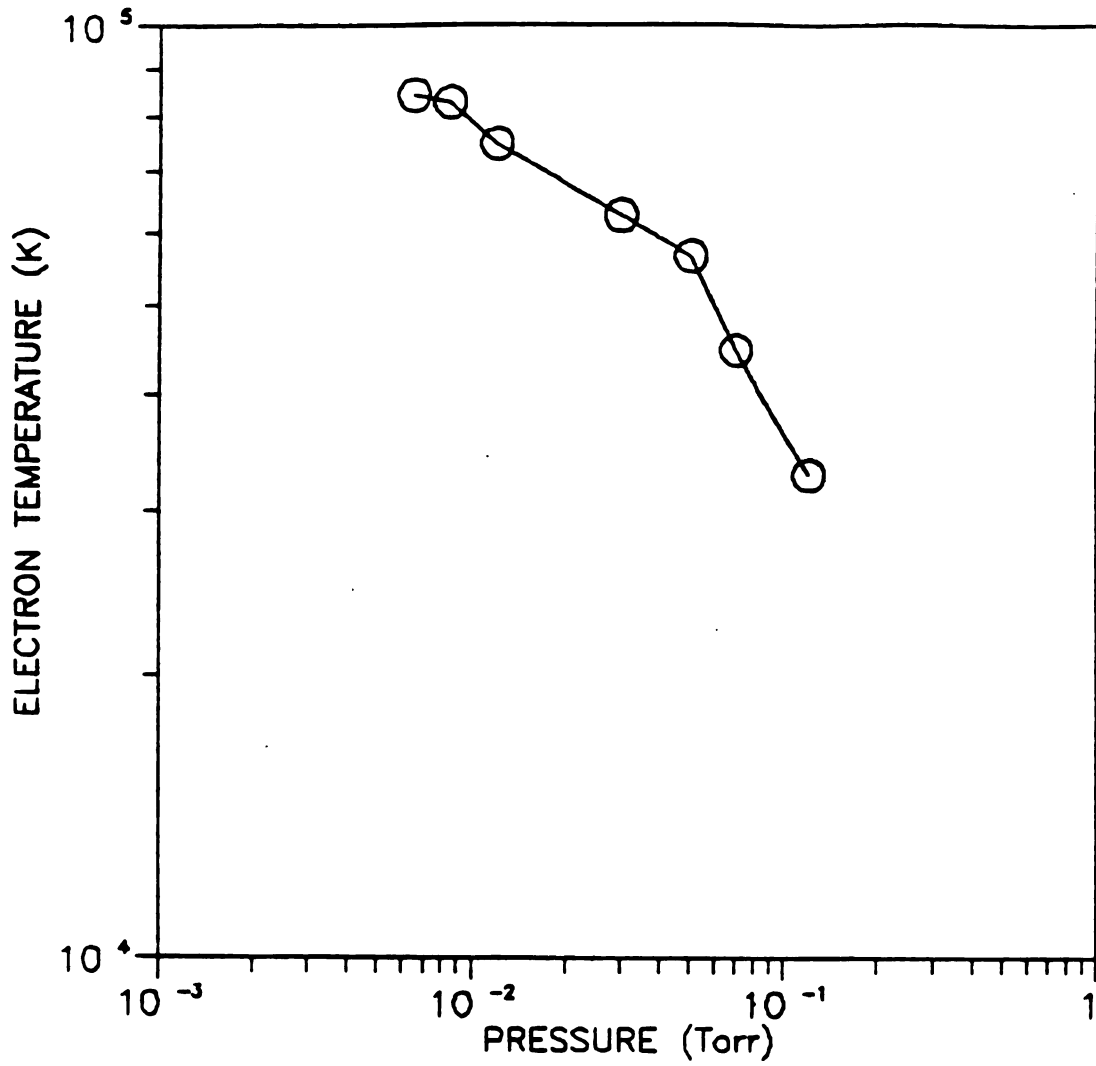
which is higher than the 2.45 GHz excitation frequency.

Oxygen gas was also used in this experiment to characterize an oxygen microwave discharge used for oxide growth on a silicon substrate⁶³ and to also demonstrate the capability to produce an oxygen ion beam with a microwave applicator. The measured electron density and electron temperature are shown in Figures 5.10 and 5.11. Here again the 1.8 cm high quartz disk was used. The microwave power was held constant at 200 W. The bell-jar pressure was varied from 2×10^{-4} Torr to 0.1 Torr and the gas flow ranged from 30 sccm to 130 sccm.



Gas - Oxygen
Applicator I
No Magnets
Disk - 1.8 cm
Power - 200 W

Figure 5.10 Electron Density Versus Discharge Pressure For Oxygen Gas



Gas - Oxygen
Applicator I
No Magnets

Disk - 1.8 cm
Power - 200 W

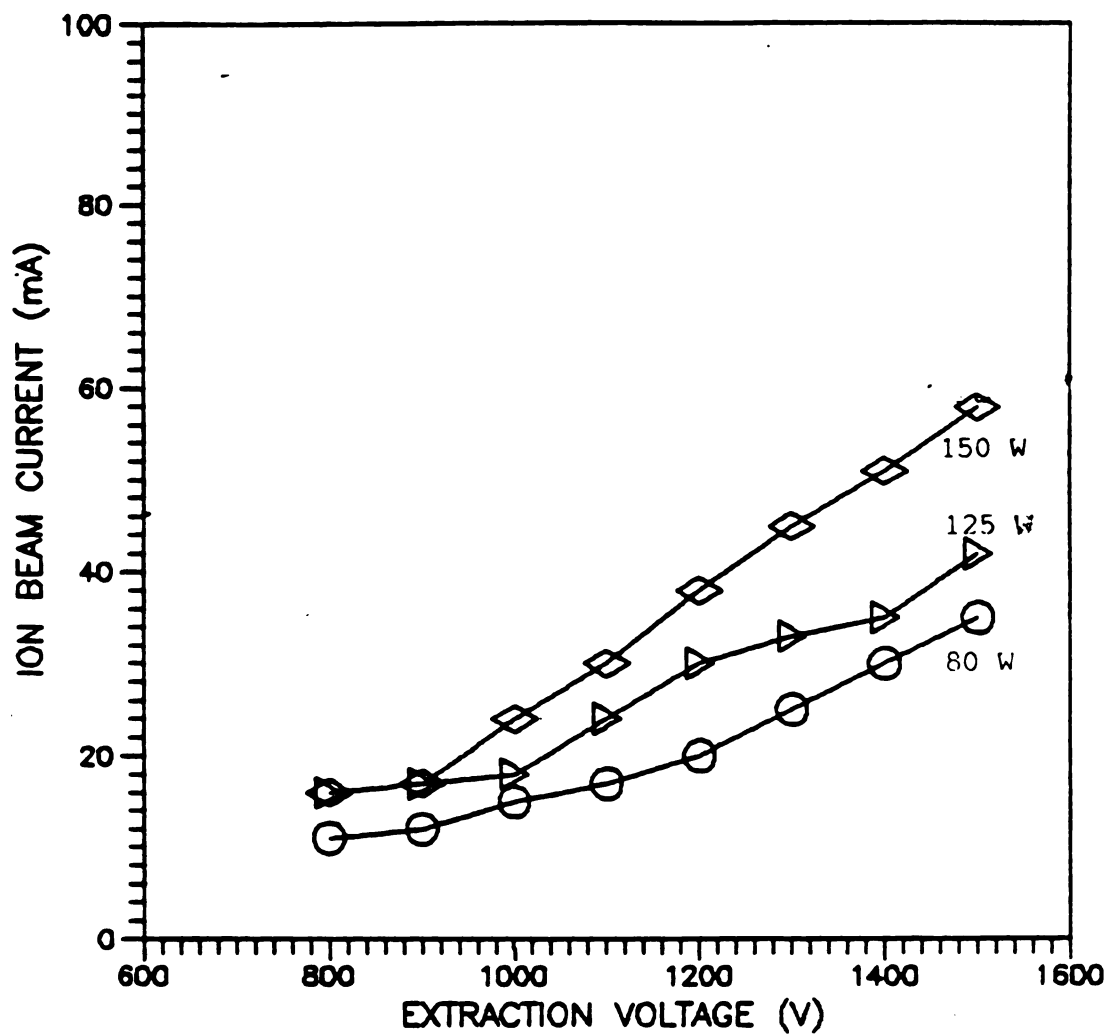
Figure 5.11 Electron Temperature Versus Discharge Pressure for Oxygen Gas

5.2.3 ION BEAM EXTRACTION.

5.2.3.1 SINGLE GRID.

Ion beam extraction using applicator I without magnets and the single grid was performed for argon gas. The extraction grid system and procedure are described in Chapter 4, Figures 4.16 and 4.20. Figure 5.12 shows the ion beam current versus extraction voltage obtained with the 1.8 cm high quartz disk versus different constant input microwave powers. The extraction voltage is defined as the sum of the voltages V_+ and V_- applied between the cavity base plate and the single extraction grid. The bell-jar pressure was 4×10^{-4} Torr corresponding to a discharge pressure of 7×10^{-3} Torr, the argon flow rate was 20 sccm. Each curve in Figure 5.12 was obtained for a constant input power, while the extraction voltage was varied from 800 V to 1500 V in 100 V increments.

The irregularities observed on the curves of Figure 5.12 can be attributed to the fact that the conditions for matching the microwave power to the cavity-plasma system do change for each extraction voltage increment. When the extraction voltage is increased, more ions are extracted from the discharge resulting in a reduction of the discharge pressure which causes a change in the ion density in the discharge. Since the plasma dielectric constant is a function of the electron density, a change in the ion



Gas - Argon
 Applicator I
 No Magnets
 Single Grid
 Mode TE_{211}

Gas Flow = 20 sccm
 Discharge Pressure = 7×10^{-3} Torr
 Disk = 1.8 cm
 $L_g = 7.7$ cm
 $L_p = +0.65$ cm

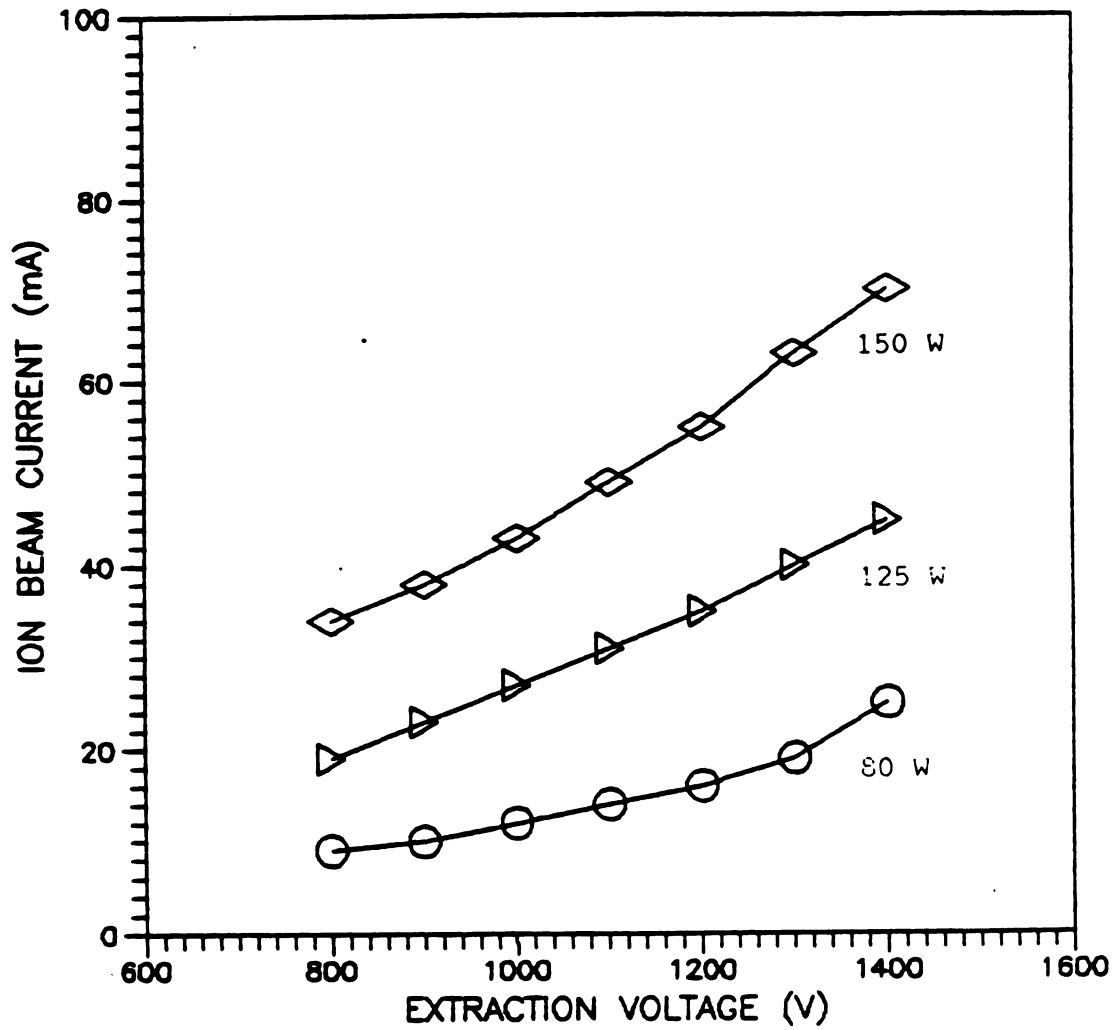
Figure 5.12 Ion Beam Extraction Versus Extraction Voltage For Different Powers

density will result in a change in the electrical properties of the plasma.

To compensate for these changes, the cavity has to be retuned for each voltage increment. This was done in practice by readjusting the sliding short position which was driven by a small electric motor. This motor is controlled by a separate unit which is electrically isolated from the high voltages applied to the cavity.

When the 1.8 cm quartz disk is used, the process of tuning the cavity was very sensitive to the sliding short displacements. When the 4.0 cm high quartz disk was used under the same conditions of pressure and flow, the plasma became much more stable under all extraction conditions. The results of the beam current versus the extraction voltage for the 4.0 cm quartz disk are shown in Figure 5.13. In this case the power matching conditions became less sensitive to the extraction voltage variations and to the sliding short displacements. This reduced sensitivity can be attributed in part to the fact that a larger plasma volume inside the cavity will absorb more microwave power, thus reducing the quality factor of the cavity for resonance.

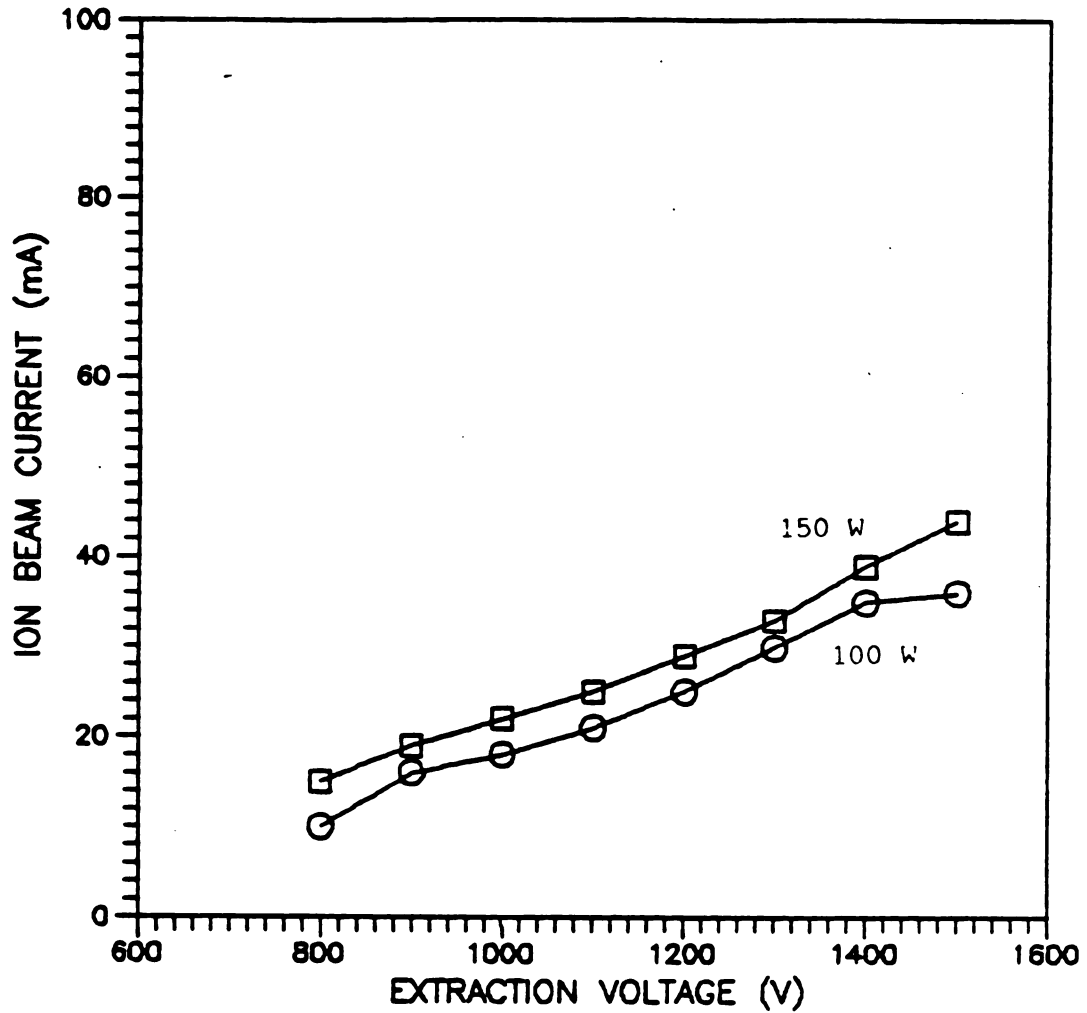
Figure 5.14 illustrates the reduced sensitivity of the tuning parameters by showing that an ion beam can still be extracted when the sliding short position L_S has been reduced by 4 mm and the coupling probe position L_P has been reduced by 1.25 cm simultaneously from the previous values.



Gas - Argon
Applicator I
No Magnets
Single Grid
Mode $TE_{2,11}$

Gas Flow = 20 sccm
Discharge Pressure = 7×10^{-3} Torr
Disk = 4.0 cm
 $L_s = 7.9$ cm
 $L_p = +1.9$ cm

Figure 5.13 Ion Beam Current Versus Extraction Voltage With The 4.0 Cm Disk



Gas - Argon
 Applicator I
 No Magnets
 Single Grid
 Mode TE₂₁₁

Gas Flow - 20 sccm
 Discharge Pressure - 7×10^{-3} Torr
 Disk - 4.0 cm
 $L_s = 7.5$ cm
 $L_p = +0.65$ cm

Figure 5.14 Ion Current Versus Extraction Voltage when The Cavity is Not Perfectly Tuned

In this case however a critical power match was not achieved and the ion beam intensity is lower than the one obtained earlier for the same discharge conditions of pressure and input power.

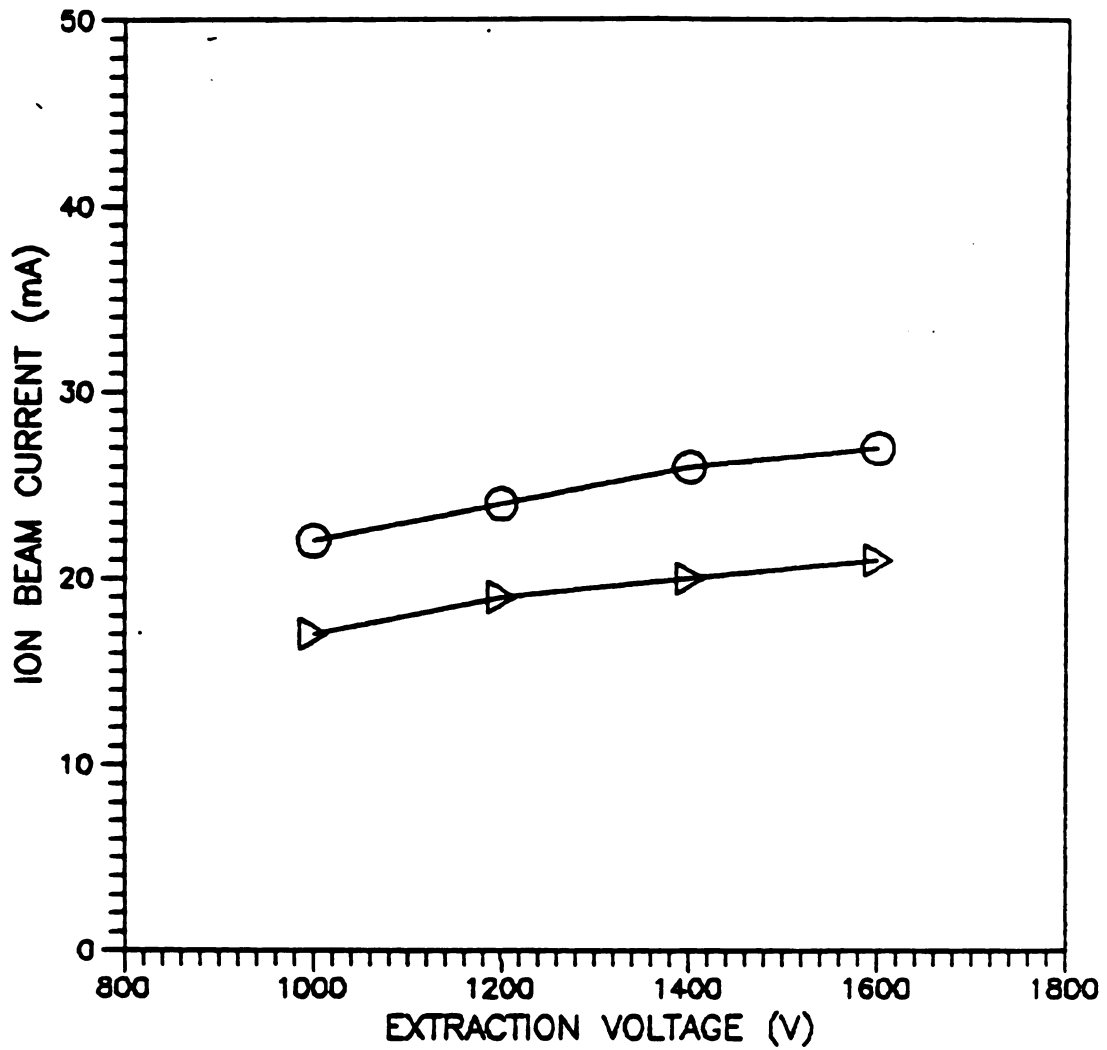
5.2.3.2 DOUBLE GRIDS.

Applicator I was also used for ion beam extraction with the double grids described in Chapter 4 and shown in Figure 4.17. The total area of the screen grid holes is equal to 3.8 cm^2 which is 86% of the 4.42 cm^2 total area of the single grid holes. The difference in geometry between the two types of grids is that the single grid has its extraction holes distributed over a total area of 24 cm^2 whereas the double grids have their extraction holes distributed over an area of only 4.9 cm^2 . Also the double grids provide a better collimation of the ion beam. Because the double grid system has a smaller grid hole area, the discharge can be operated at lower gas flow rates.

When the double grids are used, the acceleration voltage V_+ has to be more carefully adjusted since it has a direct effect on the ion beam optics. Moreover, when the absolute value of V_+ is too small, electrons from the bell-jar can possibly backstream and reach the positively biased screen grid. On the other hand, if the absolute value of V_+

is too large the acceleration grid will attract and collect a large percentage of ions from the beam.

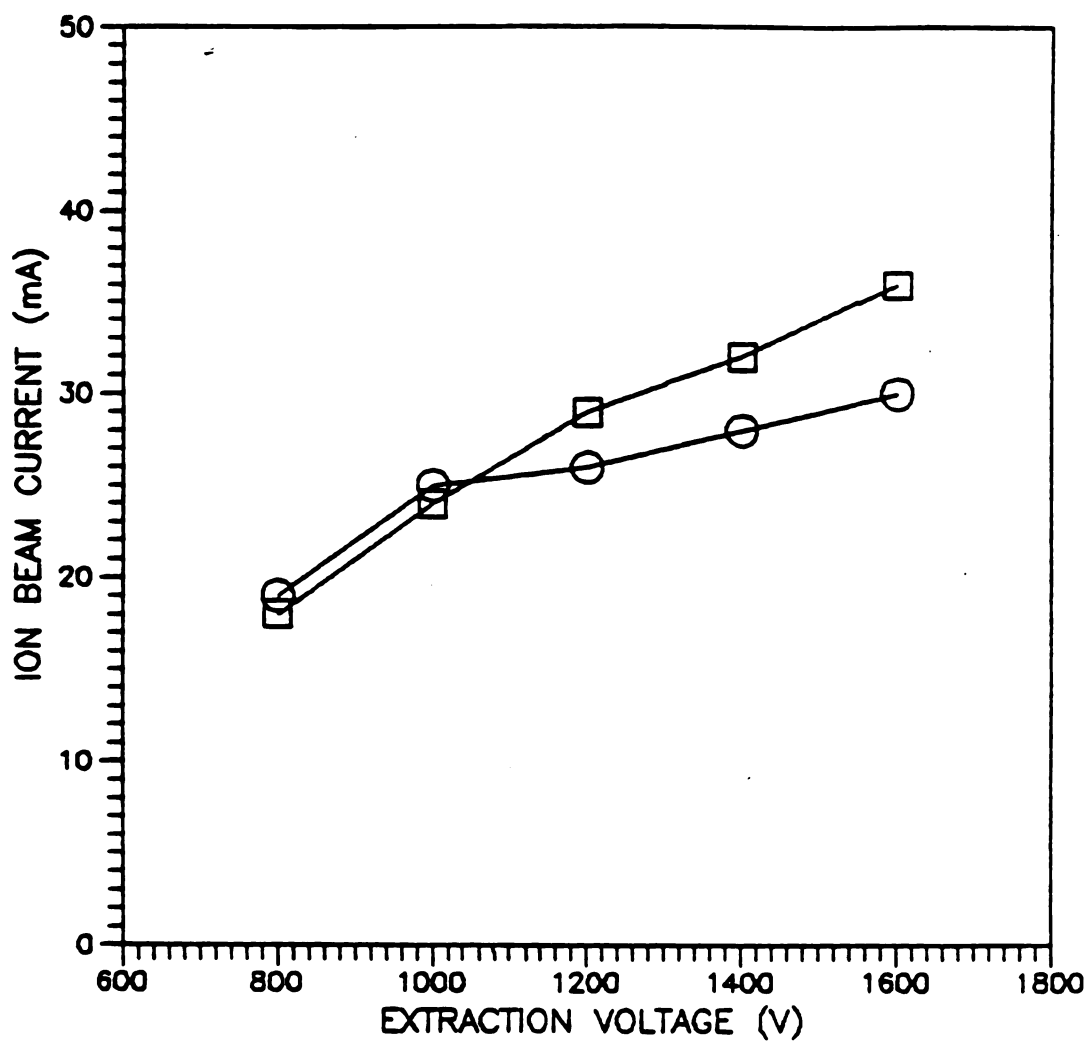
The effect of varying the acceleration grid voltage is illustrated in Figure 5.15 where argon gas is used for the same conditions of flow, pressure and input power but the acceleration grid voltage is varied from -3.5 V to -100 V. Note that the ion beam current appears higher when the acceleration voltage is low, but this result is somehow erroneous, because as explained in Chapter 4, the method used to estimate the ion beam current consists of measuring the electron current falling on the screen grid and cavity base plate and the ion current collected by the acceleration grid. The difference between these two currents is considered to be approximately equal to the ion beam current. However, when the acceleration voltage is not low enough electrons emitted from the neutralizer can possibly backstream to the screen grid over estimating the value of the electron current measured between the screen grid and ground. This problem can be eliminated by applying a higher negative voltage to the acceleration grid but in such a case it was observed that the ion beam was no longer focused. In order to find the optimum value of the accelerating voltage, a Faraday cup (described in Chapter 4) was positioned directly on the beam path to measure the intensity of the beam over a constant cross section. Using the Faraday cup, the acceleration voltage could be adjusted to simultaneously minimize the neutralizer electrons collected by the screen



Gas - Argon
Applicator I
No Magnets
Double Grids
Mode $TE_{2,11}$
Power = 250 W

Disk = 1.8 cm
Gas Flow = 6.0 sccm
○ - Acceleration Voltage = -3.5 V
△ - Acceleration Voltage = -100 V

Figure 5.15 Ion Current Versus Extraction Voltage For Different Acceleration Voltages



Gas - Argon
Applicator I
No Magnets
Double Grids
Mode TE_{2,11}

Disk - 1.8 cm
□ - Gas Flow Rate = 3.5 sccm
Power = 200 W
○ - Gas Flow Rate = 2 sccm
Power = 240 W

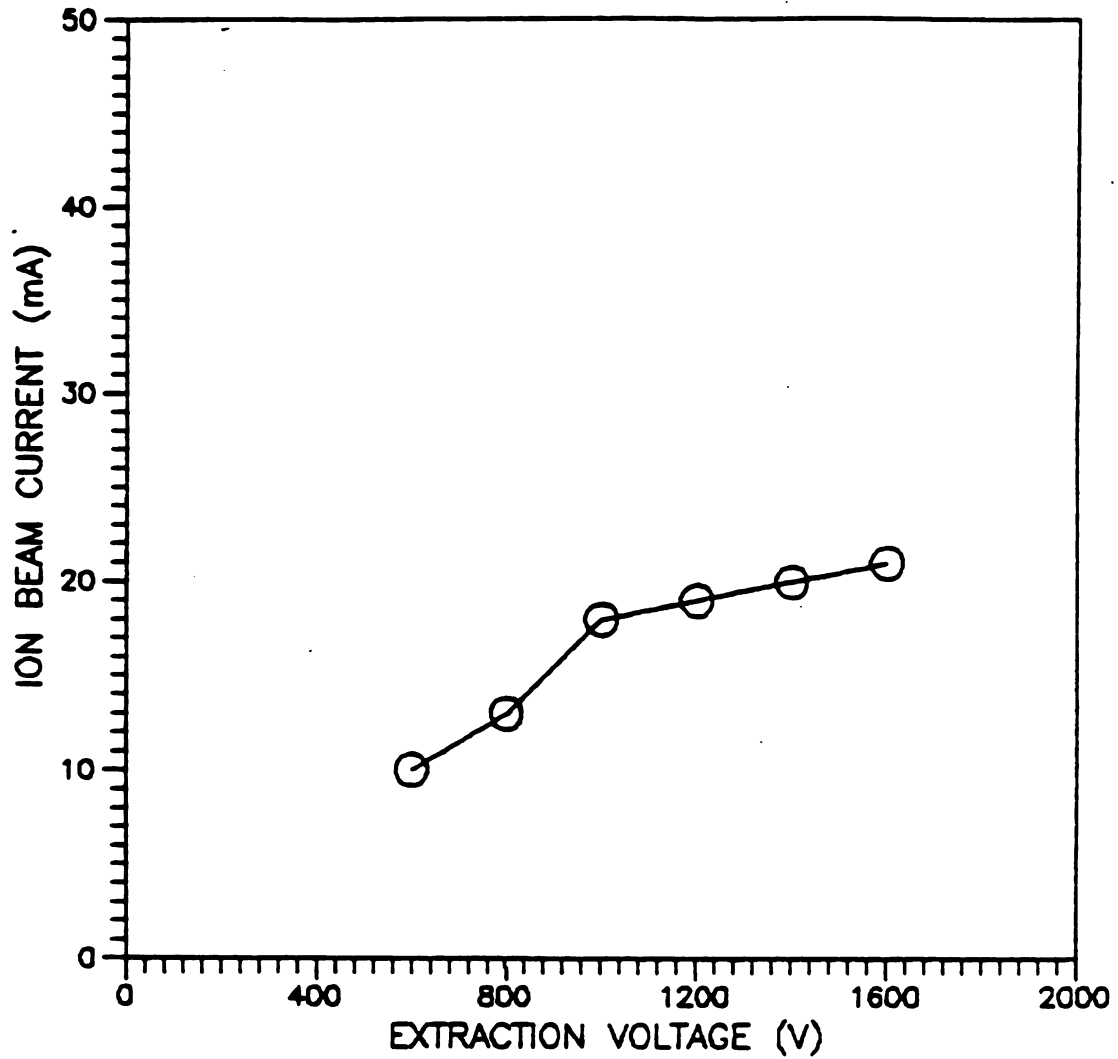
Figure 5.16 Ion Current Versus Extraction Voltage For Low Gas Flow Rates

grid and optimize the beam focusing. It was found that the optimum value for the acceleration voltage was approximately -50 V. The value of this voltage could vary by about 10% depending on the discharge conditions and the screen grid voltage.

Figure 5.16 shows ion beam currents obtained for very low argon flow rates and low discharge pressures. The quartz disk used was 1.8 cm high. One curve is obtained for a flow rate of 3.5 sccm, a discharge pressure of 1.5×10^{-3} Torr and an input power of 200 W. The second curve is obtained for a flow rate of 2 sccm, a discharge pressure of 8.7×10^{-4} Torr and an input power of 240 W. In such a pressure range the discharge was unstable and very sensitive to the gas flow adjustments. In order to maintain the discharge, the input microwave power had to be increased as the gas flow was progressively reduced to 2 sccm. The discharge could not be maintained at lower pressures with this applicator.

5.2.3.3 OXYGEN ION BEAM EXTRACTION.

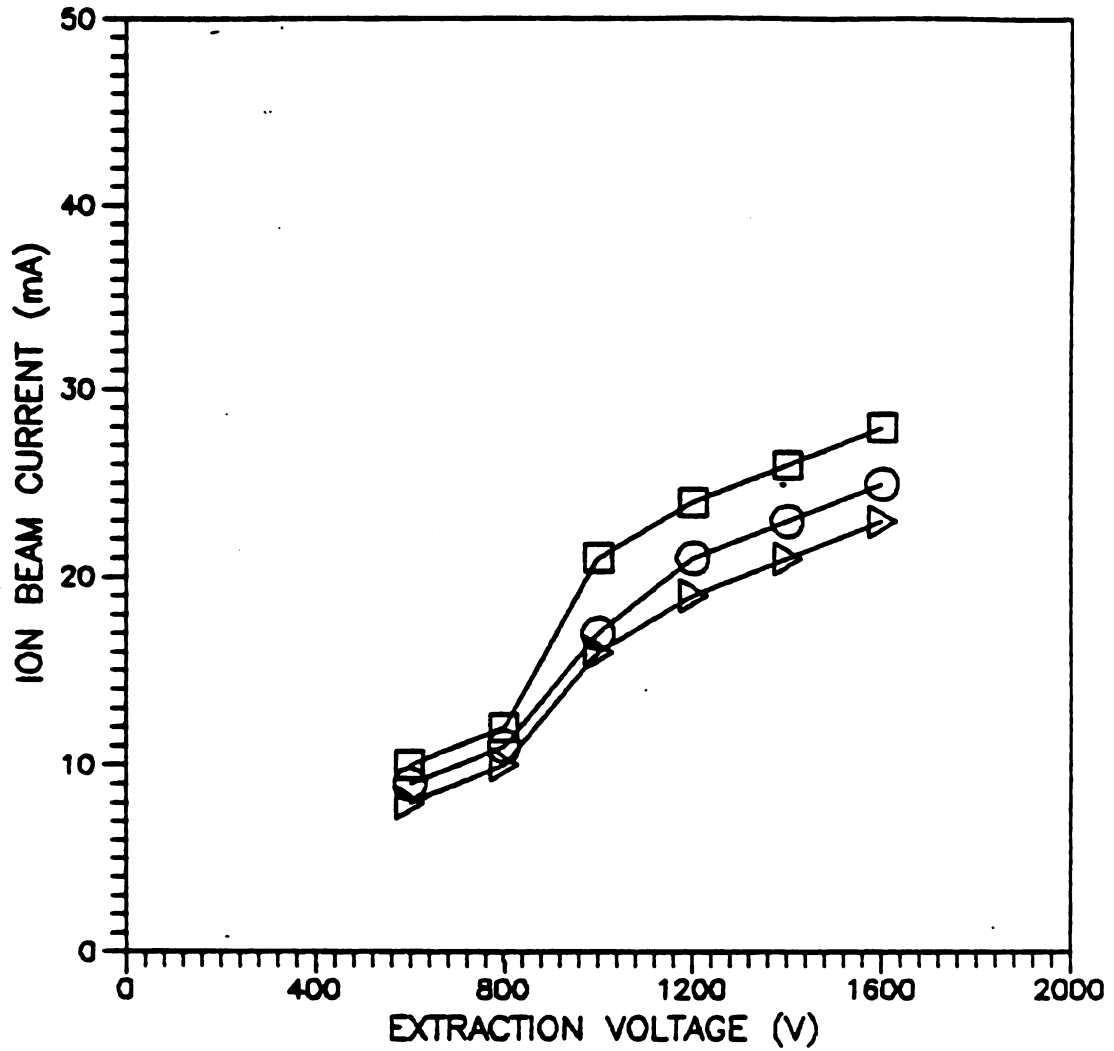
An oxygen ion beam was extracted using applicator I and the double grids. Figures 5.17 and 5.18 show the results obtained with the 1.8 cm quartz disk. The gas flow rates range from 15 sccm down to 3.4 sccm corresponding to discharge pressures between 5.3×10^{-3} Torr and 1.2×10^{-3} Torr.



Gas - Oxygen
Applicator I
No Magnets
Double Grids
Mode TE₂₁₁
Disk - 1.8 cm

Power - 156 W
Gas Flow - 15 sccm
Discharge Pressure -
7.2 × 10⁻² Torr

Figure 5.17 Ion Current Versus Extraction Voltage For Oxygen Gas



Gas - Oxygen
 Applicator I
 No Magnets
 Double Grids
 Mode TE_{211}
 Disk - 1.8 cm

△ - Flow = 6 sccm
 Power = 200 W

○ - Flow = 4 sccm
 Power = 250 W

□ - Flow = 3.4 sccm
 Power = 290 W

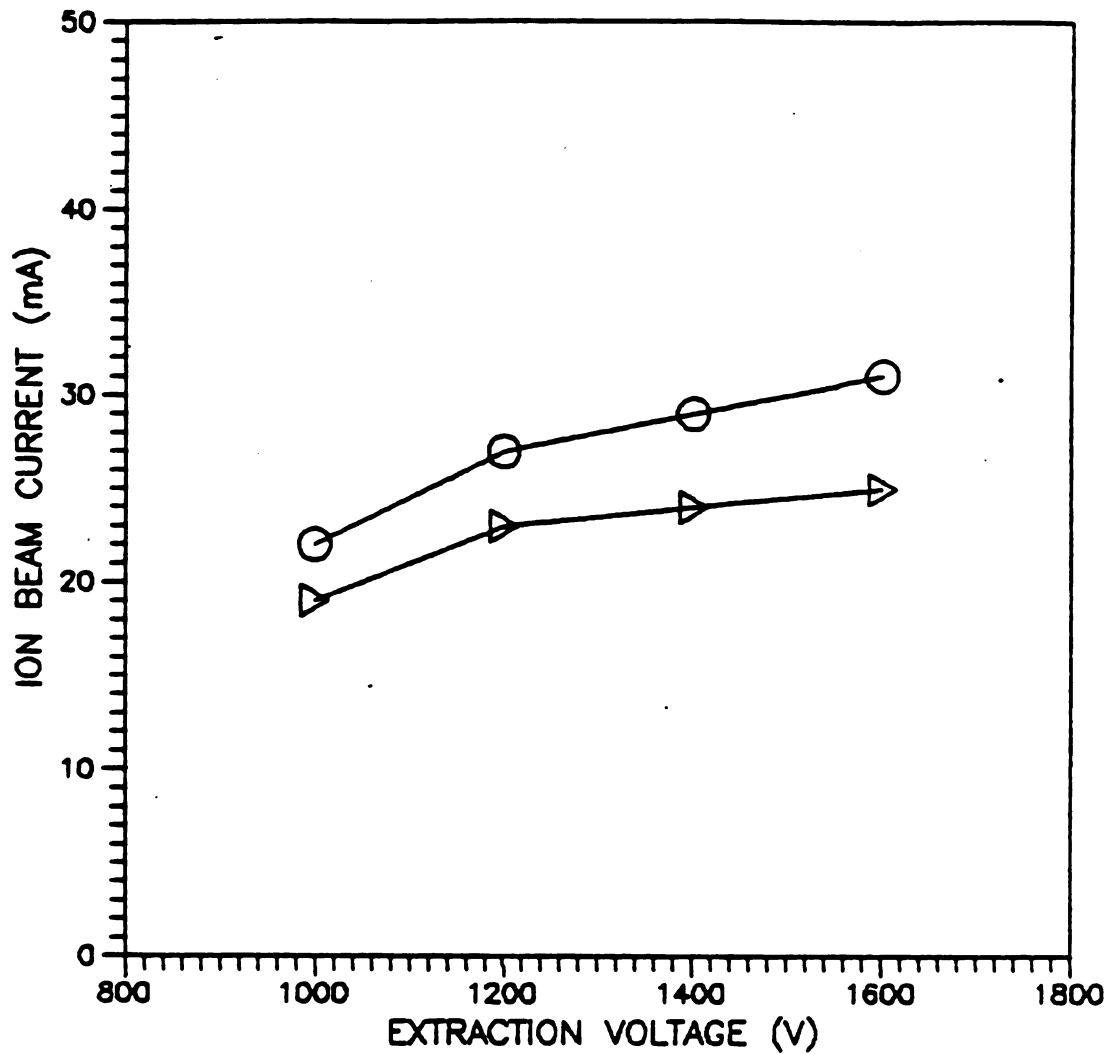
Figure 5.18 Ion Current Versus Extraction Voltage For Oxygen At Low Flow Rates

The input microwave power was varied from 150 W to 290 W in order to maintain the discharge when the flow was decreased. The 4.0 cm quartz disk was also used and the results for an oxygen flow rate of 2 sccm are shown in Figure 5.19.

In all these measurement an abrupt increase of the ion beam current is observed as the extraction voltage is progressively changed from 800 V to 1000 V. This transition is also observed when argon gas is used for ion beam extraction. The transition has been visually confirmed during the experiment. When the extraction voltage is lower than 800 V the ion beam cannot be seen but rather a diffuse glow fills the whole bell-jar. When the extraction voltage reaches a threshold value, a well collimated beam suddenly appears downstream from the grids. The threshold voltage varies between 800 V and 1000 V depending on the operating discharge conditions. The change in the beam behavior could be explained by the fact that for lower screen grid voltages the plasma sheath near the screen grid holes does not reach an optimum configuration to allow for an optimum ion optics focusing between the two grids.

5.3 APPLICATOR I RETROFITTED.

Electron density and electron temperature measurements were not possible when the samarium-cobalt magnets were added inside the cavity. The multicusp static magnetic



Gas - Oxygen
Applicator I
No Magnets
Double Grids
Mode TE_{2,11}
Disk - 4.0 cm

Gas Flow - 2 sccm
Discharge Pressure - 1×10^{-3} Torr
 Δ - Power - 200 W
O - Power - 300 W

Figure 5.19 Ion Current Versus Extraction Voltage For Oxygen With The 4.0 cm Disk

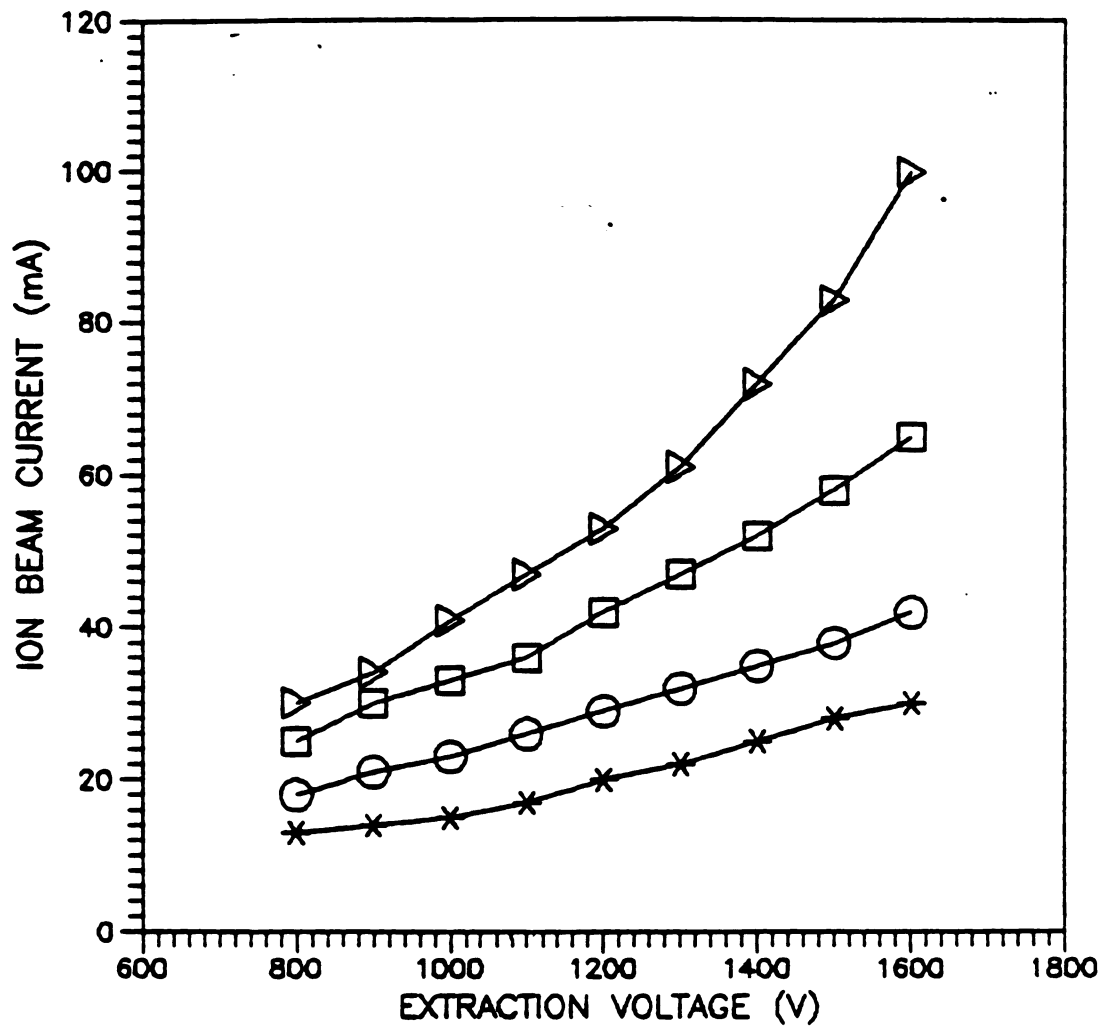
fields were measured to be non zero around the Langmuir probe position.

A magnetic field applied in the probe region will disturb the plasma in that region by forcing the electrons to follow the field lines in a specific pattern. This electron trajectory disturbance will adversely affect the probe measurements since the method is based on sampling thermal electrons.

Ion beam extraction measurements were taken for argon gas using the single grid. The 4.0 cm high quartz disk was chosen for this experiment because the 8 rare earth magnets located around the discharge region as described in Chapter 4, produce a conducting shield preventing part of the resonant electric fields from reaching the discharge region. When the 1.8 cm disk was used the plasma manifested instabilities and an ion beam could not be extracted. The 4.0 cm quartz disk was high enough to expose a larger discharge surface to the resonant field for more stability.

Figure 5.20 shows results of ion beam extraction when only 8 magnets were positioned around the discharge area. The argon flow rate was 20 sccm and the discharge pressure was 5.1×10^{-3} Torr, the microwave input power was varied from 80 W to 150 W. The discharge was stable under all conditions.

A comparison of these results with the case where no magnets are present (Fig. 5.13) shows that the beam intensities obtained are comparable for the same discharge



Gas - Argon
 Applicator I
 Single Grid
 Mode TE_{211}
 Flow - 20 sccm
 Disk - 4.0 cm

Discharge Pressure - 7×10^{-3} Torr

Δ - 150 W
 \square - 125 W
 \circ - 100 W
 $*$ - 80 W

Figure 5.20 Ion Extraction Applicator I Retrofitted With Only 8 Magnets Surrounding The Discharge

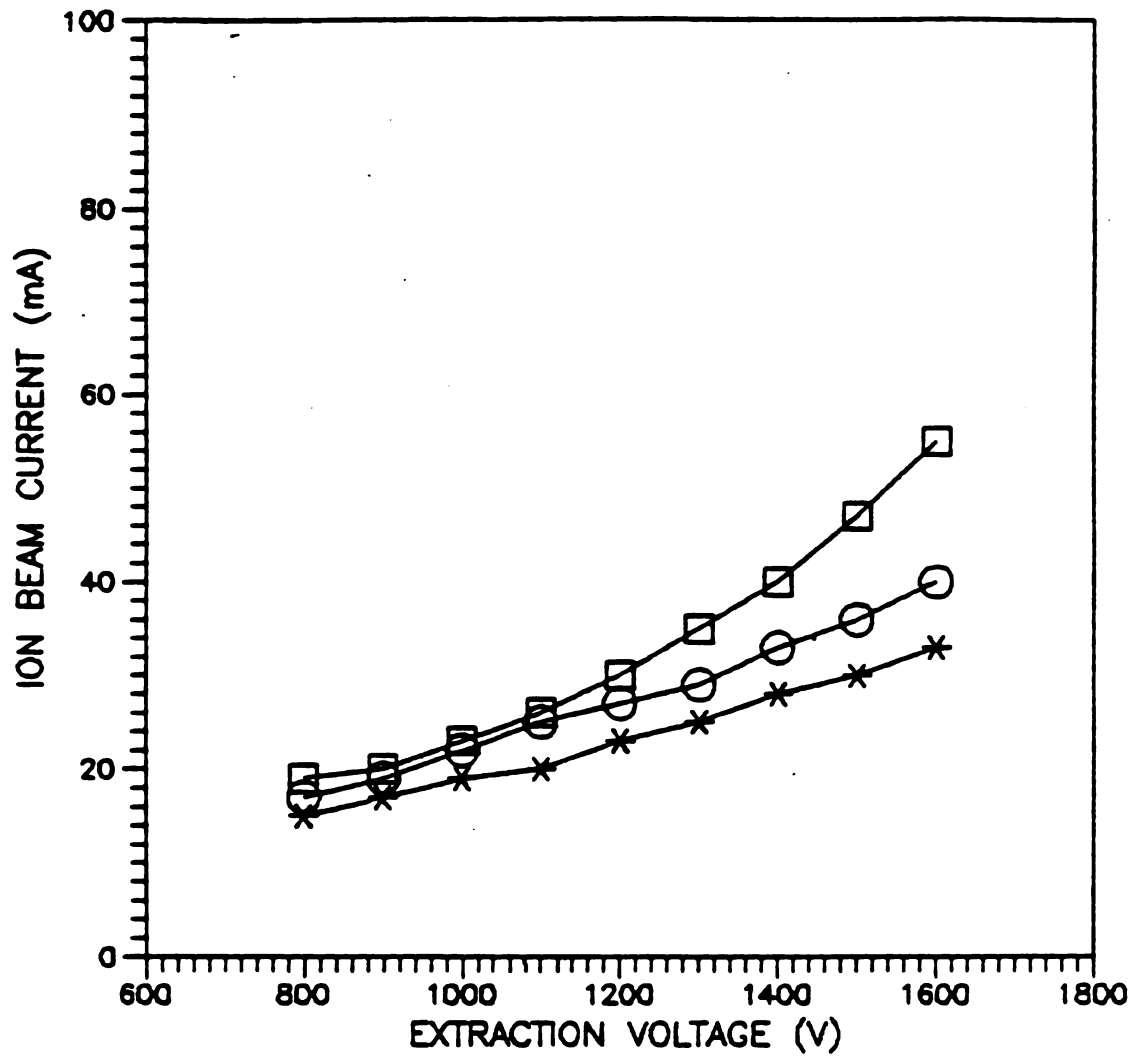
conditions. The stability of the discharge however, has been considerably improved.

Figure 5.21 shows the results of ion beam extraction when the nine magnets array was added in the cavity. These 9 magnets were positioned on the sliding short as described in Chapter 4. For the same discharge conditions as the preceding case, extracted ion beam currents were substantially decreased. This ion beam reduction can be explained by the fact that the nine magnets array causes an important disturbance of the resonant cavity electromagnetic fields even when these magnets were covered with an aluminum foil sheath.

5.4 ECR APPLICATOR.

5.4.1 PRELIMINARY CALIBRATIONS.

The cavity resonant modes were investigated using a frequency sweep generator and microwave circuit described elsewhere¹³. The resonant modes obtained with an excitation frequency of 2.45 GHz are characterized by the sliding short positions and the coupling probe positions. The results are displayed in Table 5.1 for the empty cavity and the cavity loaded with three different quartz disk sizes. These modes could not easily be identified with the resonant modes



Gas - Argon
Applicator I
Single Grid
Disk - 4.0 cm

Flow - 20 sccm
Discharge Pressure - 7×10^{-3} Torr

□ - 150 W
○ - 125 W
* - 100 W

Figure 5.21 Ion Extraction With Applicator I Retrofitted With 17 Magnets

Table 5.1 ECR Applicator Tuning Parameters

SLIDING SHORT LENGTHS L_S AND COUPLING
 PROBE POSITIONS L_P CORRESPONDING TO
 DIFFERENT RESONANT MODES FOR THE
 ECR APPLICATOR

EMPTY CAVITY

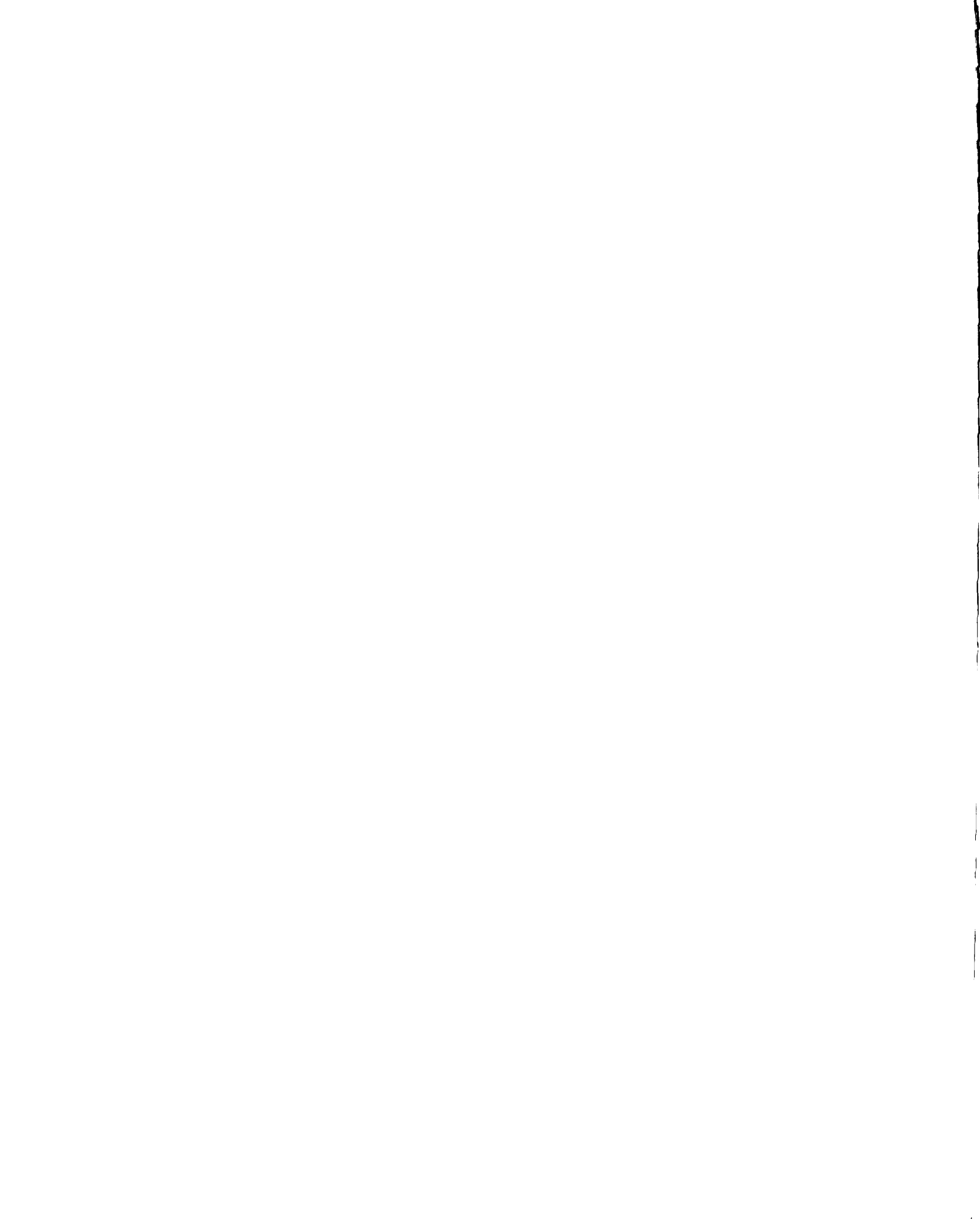
L_S (cm)	7.3	7.65	7.7	9.05
L_P (cm)	+0.7	+0.95	+0.3	+0.50

CAVITY WITH THE 1.8 cm DISK

L_S (cm)	7.0	8.0	12.5
L_P (cm)	+1.15	+0.37	+0.8

CAVITY WITH THE 4.0 cm DISK

L_S (cm)	6.85	8.48	8.5	10.75	11.95	11.98
L_P (cm)	+0.7	+0.35	+0.5	+0.65	+0.2	+1.35

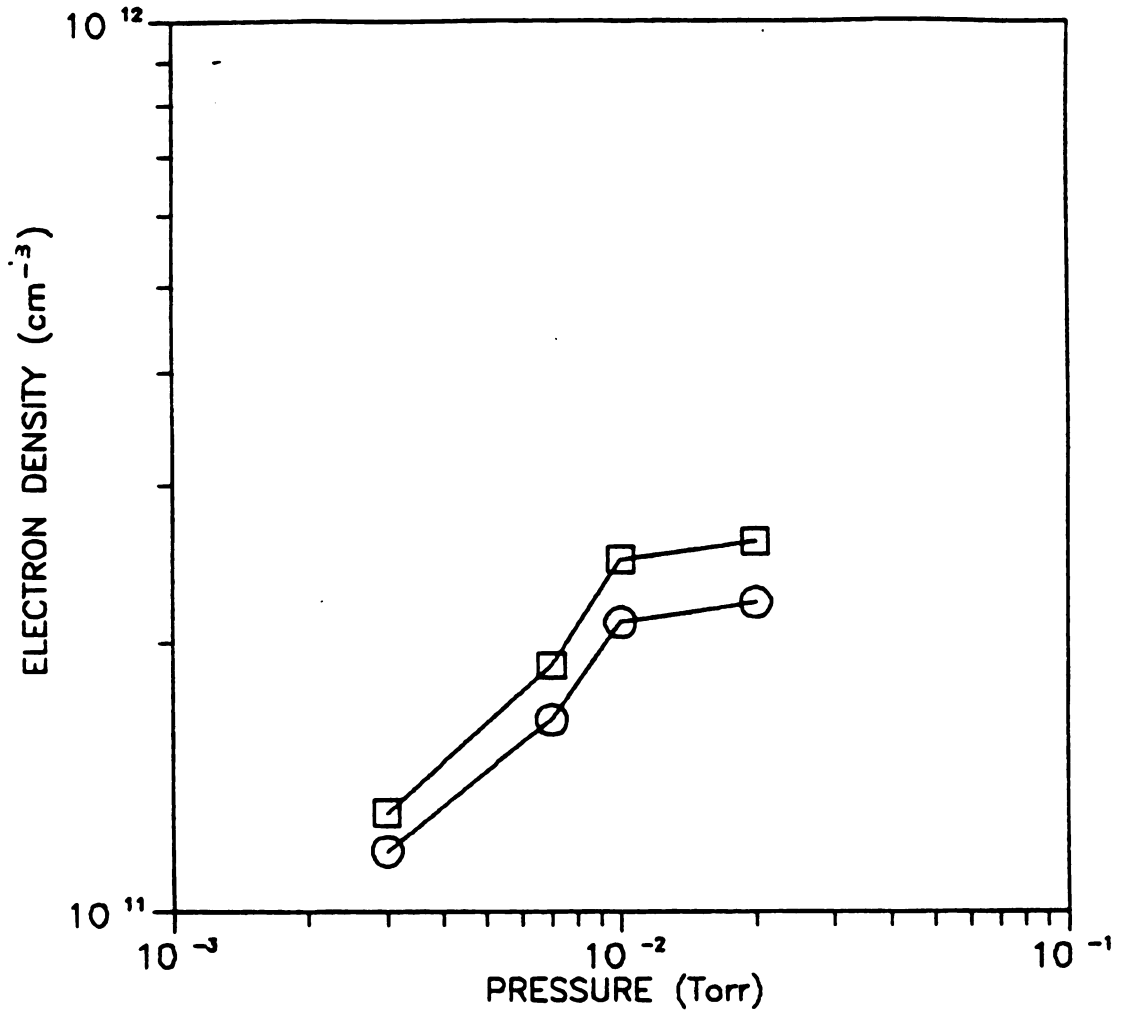


5.4.2 ELECTRON DENSITY AND TEMPERATURE MEASUREMENTS.

Electron density and electron temperature measurements were performed using a set of two Langmuir double probes positioned as described earlier. All the magnets had to be removed from the applicator in order to make these measurements because the magnetic fields were found to interfere with the accuracy of the results. The interference from the magnetic field was apparent when the probes current versus voltage curves were plotted. The current versus voltage curves showed a relatively high asymmetry between the currents collected by each individual probe. The results of electron density and electron temperature measurements obtained with no static magnetic field for argon gas at different pressures and a constant input microwave power, are shown in Figures 5.22 and 5.23.

5.4.3 ION BEAM EXTRACTION.

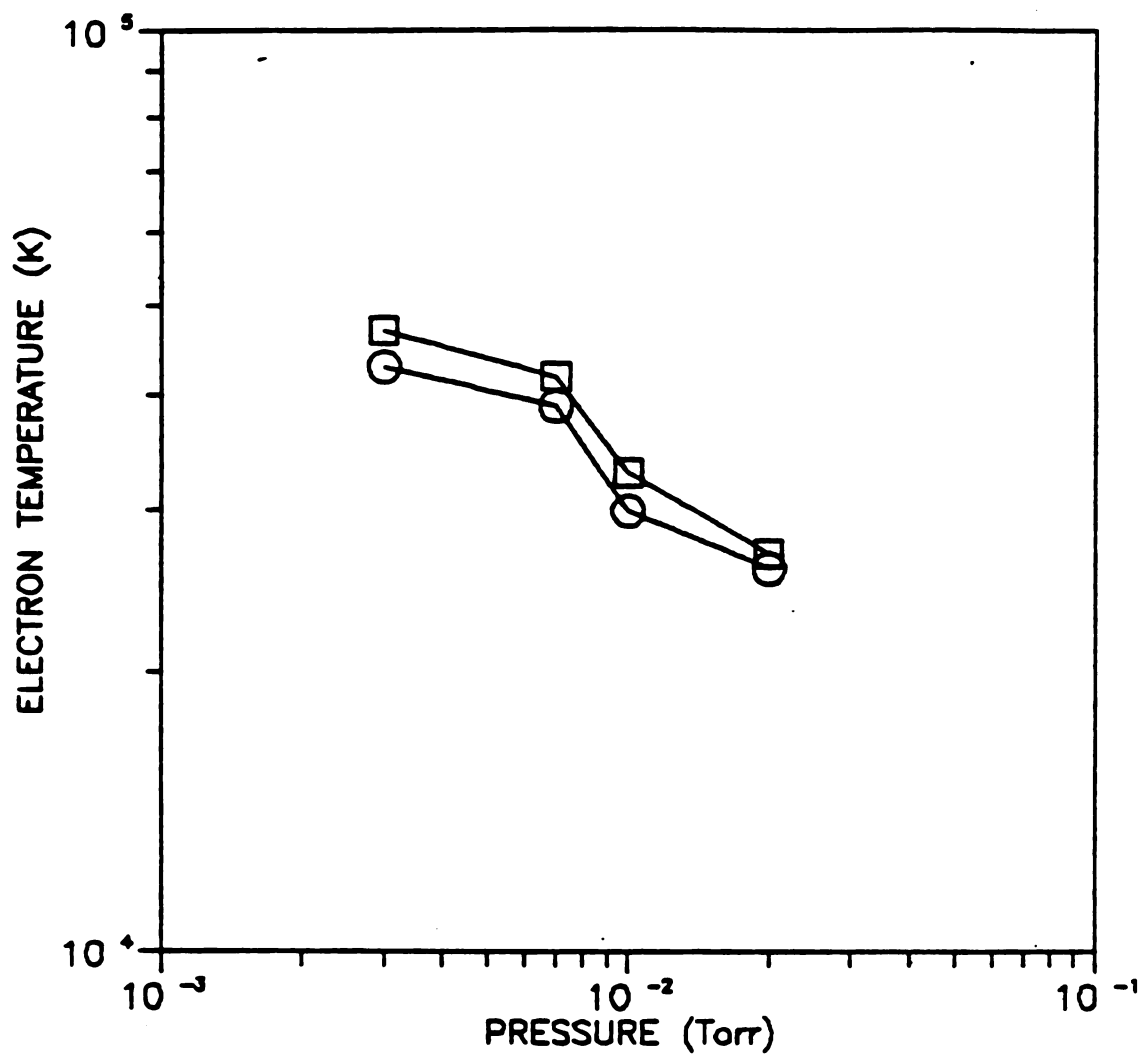
Argon ion beams were extracted using the double grids. Figure 5.24 shows the ion beam current for two different gas flows 5.6 sccm and 4.5 sccm corresponding to discharge pressures of 2.4×10^{-3} Torr and 1.9×10^{-3} Torr respectively. The microwave input power was held constant at 200 W. These measurements were taken with all the magnets removed from



Gas - Argon
 Power - 150 W
 ECR Applicator
 No Magnets

Disk = 4.0 cm, $\lambda = 1.42$ cm
 □ - Probe Position At Center
 ○ - Probe At 2.5 cm From Center

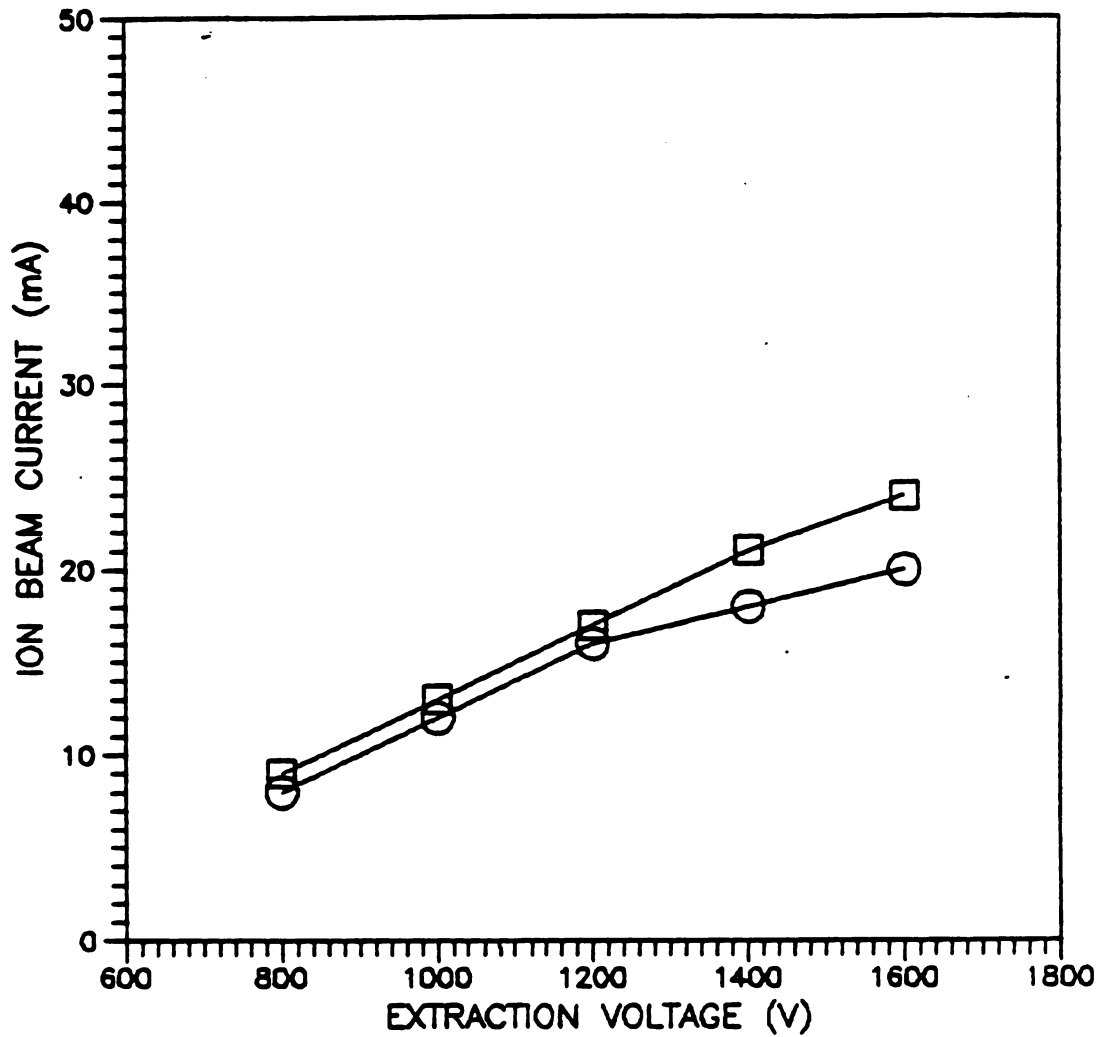
Figure 5.22 Electron Density Versus Discharge Pressure For ECR Applicator



Gas - Argon
ECR Applicator
Power - 150 W
No Magnets

Disk - 4.0 cm λ - 1.42 cm
□ - Probe At Center of
Discharge
○ - Probe At 2.5 cm From
Center

Figure 5.23 Electron Temperature Versus Discharge Pressure For ECR Applicator



Gas - Argon
Double Grids
No Magnets
Power - 200 w

○ - Flow = 5.6 sccm
Discharge Pressure = 3×10^{-3} Torr
□ - Flow = 4.5 sccm
Discharge Pressure = 2.5×10^{-3} Torr

Figure 5.24 Ion Extraction For ECR Applicator Without Magnets

calculated theoretically for an ideal resonant cavity with the same size. A positive identification of the experimental modes would require the use of a micro-coaxial electric field probe to provide a mapping of the electric field pattern near the cavity walls. This method requires a number of holes to be drilled across the cavity walls, and the results would be useful if the exact solution for the theoretical resonant modes was known for this particular geometry. This applicator differs from an ideal cylindrical cavity by the fact that the base plate has a relatively large opening in the lower part of the discharge chamber. This cylindrical opening has a height of 2.54 cm and cannot be treated as a cavity perturbation because of its large size relative to the cavity dimensions.

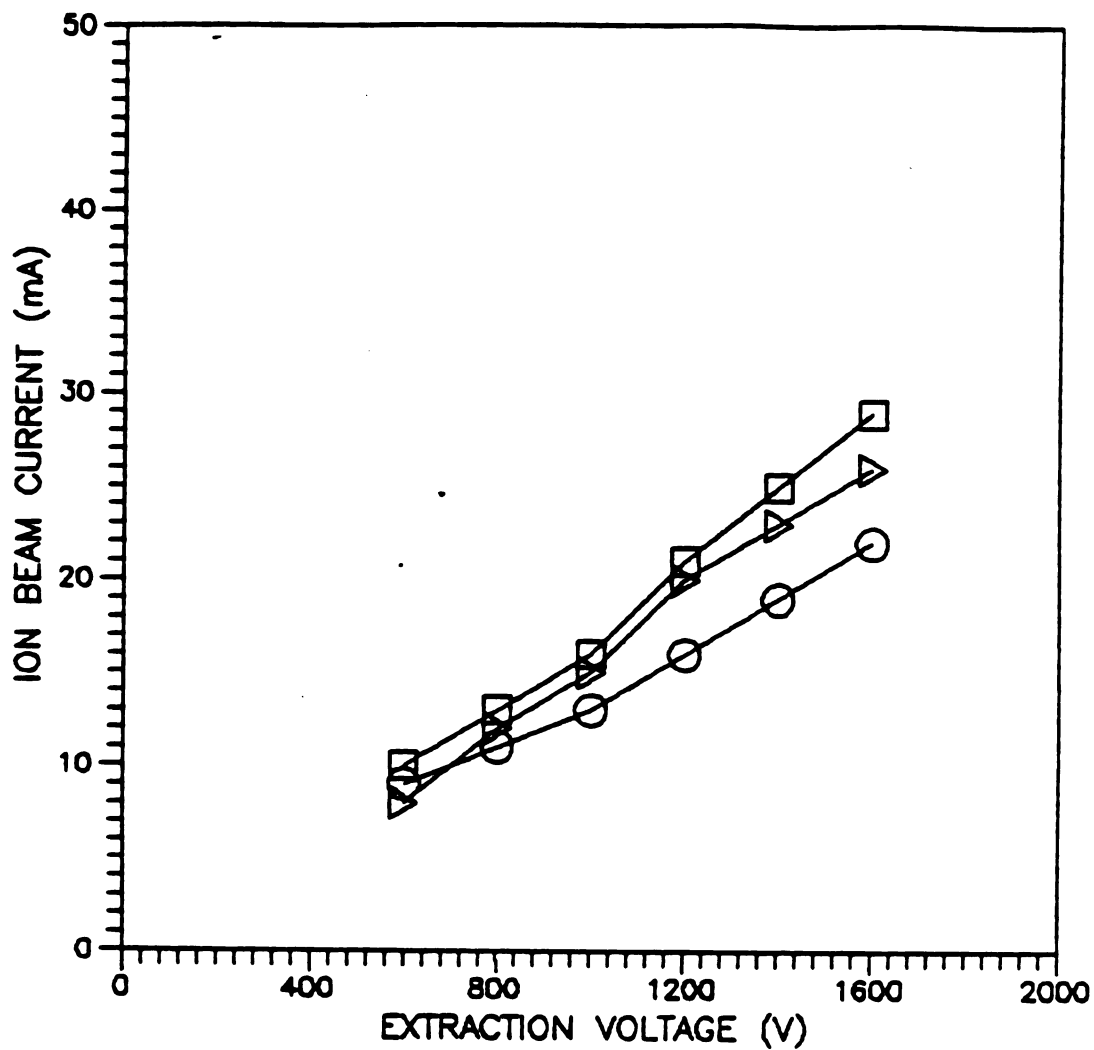
After these calibrations were completed argon discharges were obtained with each of the three quartz disks. The discharge obtained with the 1.8 cm quartz disk was observed to be unstable at low pressure conditions. Because of the geometry of this applicator, the 1.8 cm disk allows only 0.5 cm of the discharge height to be directly exposed to the cavity region. The 4.0 cm disk was found to have the optimum size.

the applicator so that the results can be compared to the case where the magnets are in place.

Figure 5.25 shows the results of ion beam extraction with all magnets in position. In this case a stable discharge was obtained with a gas flow as low as 0.86 sccm. This configuration worked very well at the very low pressures and flow rates conditions.

Figure 5.26 shows measurements of the extracted ion beam current when the argon flow rate was varied from 0.86 sccm to 24 sccm while the power was maintained constant at 250 W. Figure 5.27 displays the extracted ion beam current versus microwave input power. In this experiment the argon flow rate was 2.4 sccm corresponding to a discharge pressure of 1.3×10^{-3} Torr.

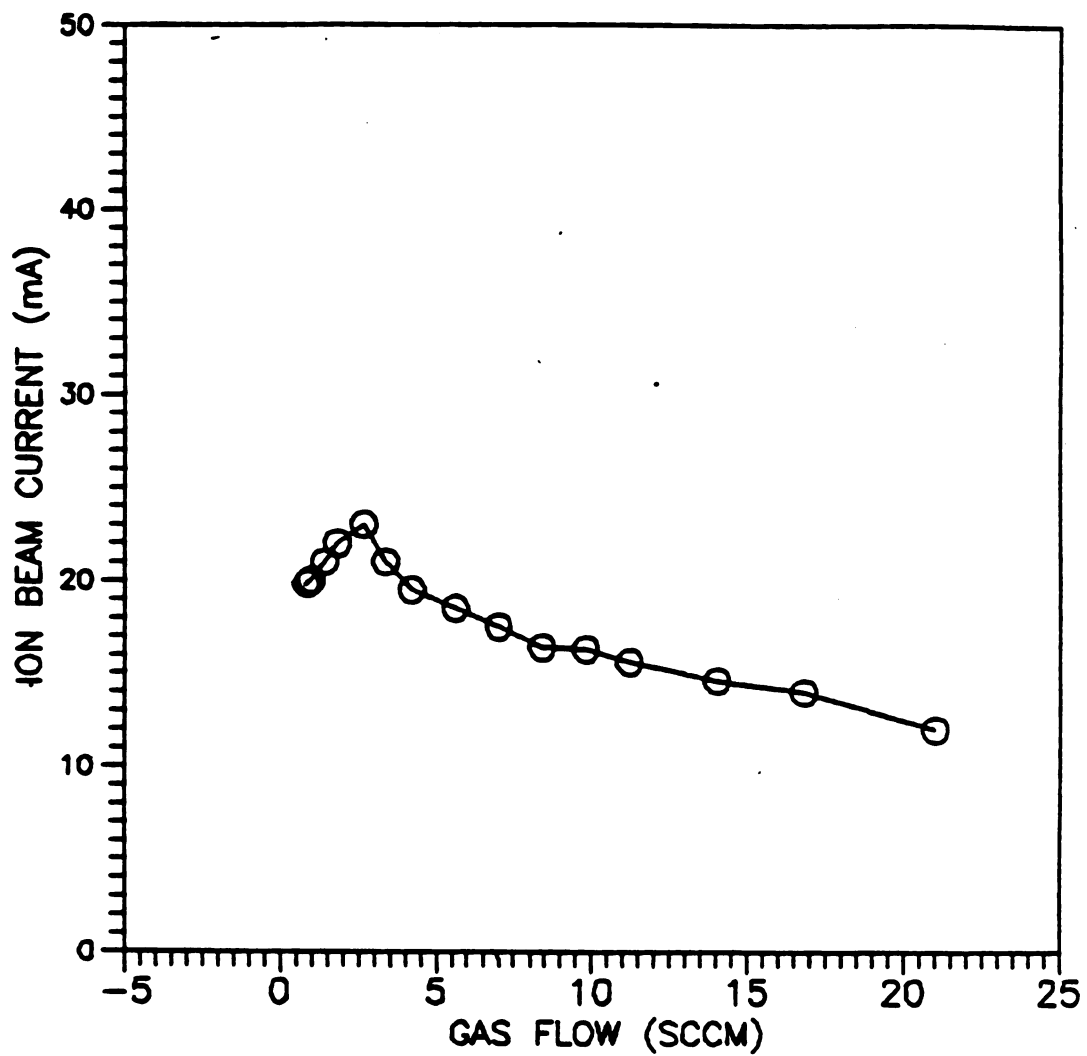
Note that the beam extraction appears to vary with power in a manner similar to the electron density. Maximum beam extraction at constant input power occurs at a gas flow of approximately 3.6 sccm, here again we note a similarity between the curves representing beam extraction and electron density versus discharge pressure. Comparing the ion beam extraction results obtained with the ECR applicator and applicator I, we note that modest improvements in ion beam extraction were obtained. However, important improvements in ease of operation were achieved with the ECR applicator.



Gas - Argon
ECR Applicator
Double Grids
Disk - 4.0 cm
Power - 200 w

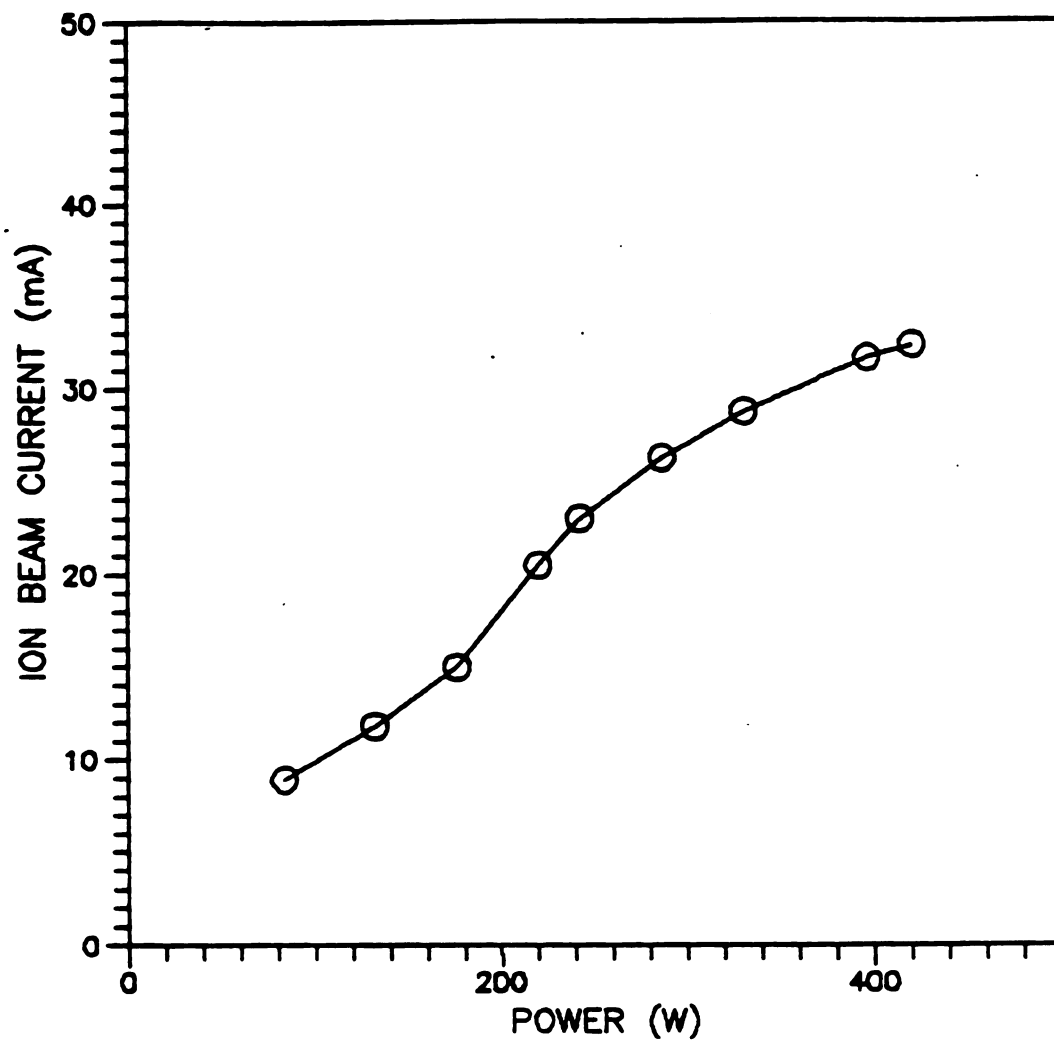
○ - Flow = 2.5 sccm
□ - Flow = 3.5 sccm
△ - Flow = 5.6 sccm

Figure 5.25 Ion Beam Extraction with ECR Applicator with All Magnets



Gas - Argon
ECR Applicator
With All Magnets
Disk - 4.0 cm
Power - 200 W

Figure 5.26 Ion Extraction versus Gas Flow



Gas - Argon
ECR Applicator
with All Magnets
Disk - 4.0 cm

Flow - 2.4 sccm
Discharge Pressure -
 1.3×10^{-3} Torr

Figure 5.27 Ion Current Versus Power

CHAPTER VI

COMPARISON OF THE EXPERIMENTAL RESULTS WITH THE THEORETICAL DISCHARGE MODEL

6.1 INTRODUCTION

This chapter presents a comparison of the experimental measurements with the results of the corresponding predictions obtained with the simple model developed in Chapter 3. In the first section, a list of the quantities that were directly measured is reviewed along with the plasma parameters calculated using the measured data. The experimental measurements such as electron temperature and ion current available for beam extraction are compared to their corresponding theoretical values in the following sections using argon as the working gas.

6.2 MEASURED QUANTITIES

The methods used in this thesis, for measuring and calculating the plasma parameters, are summarized in this section. The quantities that were directly measured with

the equipment available were:

1. The environmental (or bell jar) pressure.
2. The gas flow.
3. The cavity length.
4. The microwave coupling probe position.
5. The microwave input power.
6. The microwave reflected power.
7. The discharge wall temperature.
8. The discharge chamber dimensions.
9. The voltage and current collected by the Langmuir probes.
10. The different currents and voltages involved in the ion beam extraction.
11. The excitation frequency.

From combinations of these measured values and in some cases with the proper assumptions, plasma parameters were calculated. For instance, the discharge pressure is obtained by using the bell jar pressure along with a thermodynamic calculation. This calculation involves the geometry of the aperture used as the limiting boundary between the discharge region and the vacuum chamber. The assumption used here is that of an ideal gas conditions. This method along with the other calculation methods used in this thesis are described in Chapter 4.

The plasma parameters that were directly calculated are:

- a. The ion temperature.
- b. The discharge pressure.
- c. The plasma density.
- d. The electron temperature.
- e. The extracted ion beam current.
- f. The power absorbed by the cavity-discharge system.
- g. The power density.
- h. The degree of ionization.
- i. The mass utilization.
- j. The diffusion length of the discharge.

These quantities are then used to determine some additional parameters.

6.3 CALCULATION OF THE DISCHARGE ELECTRIC FIELD

As mentioned earlier in Chapter 3, a value for the electric field inside the discharge is required in order to have an estimate of the ion mobility. In the case of a microwave discharge, and in particular for the geometry of a discharge partially filling a resonant cavity, it is very hard to measure or calculate the exact value of the electric field inside the gas discharge. In order to do so, one

would have to solve the Boltzmann equation coupled with a set of Maxwell's equations. The coupling of these equations appears explicitly in the momentum transfer equation for the electrons (or ions) as shown in equations (3.22) and (3.24) where F is the Lorentz force applied on the charged particles

$$\bar{F} = q (\bar{E} + \bar{v} \times \bar{B})$$

where \bar{E} is the applied electric field and \bar{B} is a static magnetic field ($\bar{B}=0$ in this case).

Even with the assumption that the plasma parameters are known, it is still very hard, if not impossible, to find the exact solution for the electric field. The reason for such a difficulty is that the geometry of this particular problem is relatively complicated, in the sense that it involves a large number of boundaries.

One alternative to this direct approach is to work out a relatively simple model first. If this simple model is in reasonable agreement with the experiment, the results from this model could be used to make some justified simplifying assumptions that would make the direct approach within reach.

In the present model we assume that quantities such as the electric field, the electron collision frequency for momentum transfer and the electron temperature are uniform within the discharge. In doing so we are limiting the model to the prediction of the macroscopic properties of the discharge.

The average electric field over the plasma volume can be calculated if the effective electron-neutral collision frequency for momentum transfer ν_e and the discharge absorbed power density are known. The expressions for these two quantities are shown in equations (3.49) and (3.58) respectively.

ν_e is calculated using a numerical integration of equation (3.49) and plotted data for the electron collision frequency for argon⁵⁵. The values used for T_e were obtained from the langmuir probe measurements. The results are shown in Figure 6.1 where ν_e is plotted versus the discharge pressure.

The expression for the total microwave power absorbed by the plasma is

$$P_{\text{abs}} = \frac{1}{2} R_e \int_v \sigma E^2 dv \quad (6.1)$$

Using equation (3.56) for σ and the assumption that E and N_e are uniform throughout the discharge.

$$P_{\text{abs}} = \frac{e^2 \nu_e E^2}{2m_e(\nu_e^2 + \omega^2)} \int_v N_e(r,z) dv \quad (6.2)$$

where ω is the excitation frequency, e is the electron charge, m_e is the electron mass, E is the average electric field in the discharge and $N_e(r,z)$ is the electron density distribution.

Substituting expression (3.80) for $N_e(r,z)$ and integrating

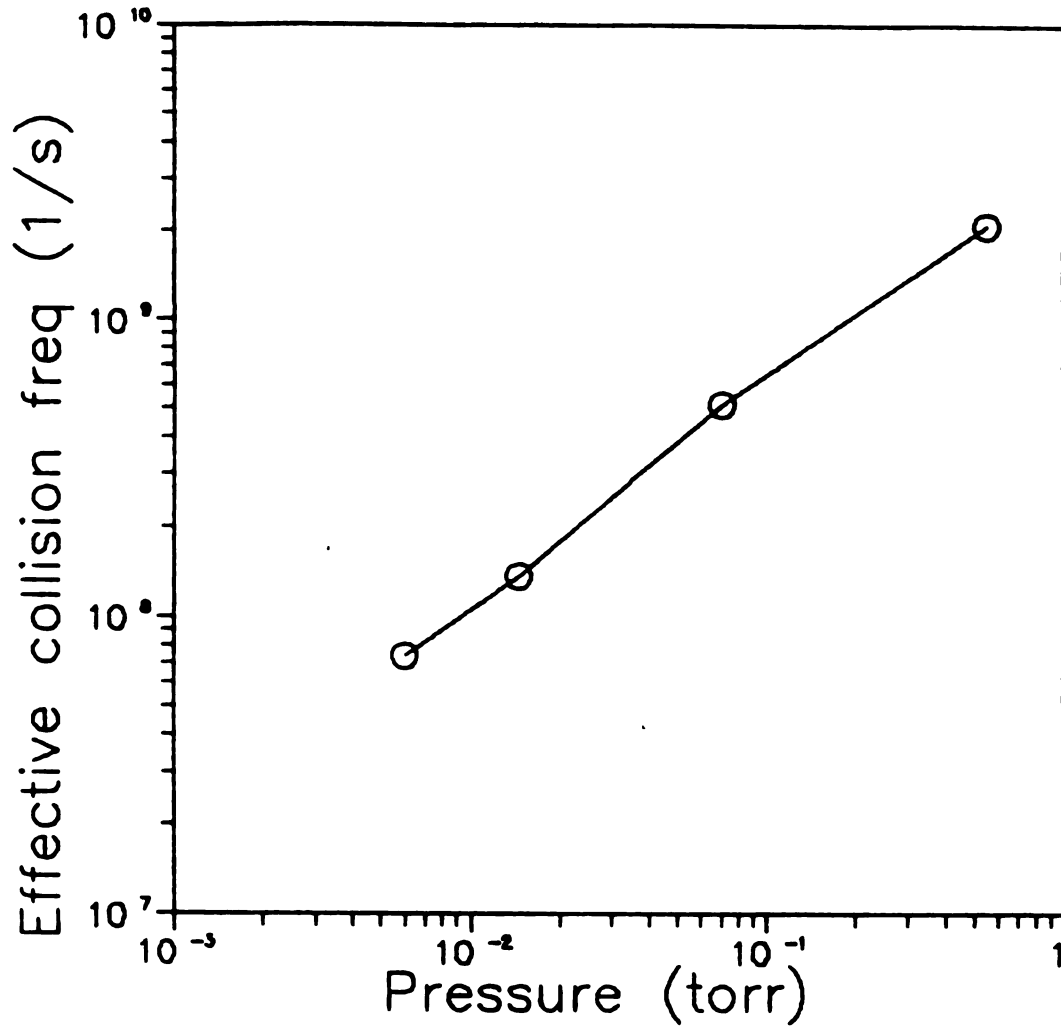


Figure 6.1 Calculated Electron-Neutral Effective Collision Frequency Versus Discharge Pressure

over the discharge volume yields

$$P_{\text{abs}} = \frac{e^2 E^2 \nu_e}{2m_e(\nu_e^2 + \omega^2)} N_0 L R^2 (0.865) \quad (6.3)$$

where N_0 is the electron density at the center of the discharge, L and R are the discharge chamber dimensions. From this expression we can calculate the value of the electric field using the previously measured values for N_0 , L , R , P_{abs} and the calculated ν_e .

$$E = \left[\frac{2P_{\text{abs}} m_e (\nu_e^2 + \omega^2)}{e^2 \nu_e N_0 L R^2 (0.865)} \right]^{\frac{1}{2}} \quad (6.4)$$

The value used for P_{abs} is approximated by the incident microwave power minus the reflected power ($P_i - P_R$). In this approximation it is assumed that all the microwave energy in the resonant cavity is absorbed by the discharge. This is obviously an over estimation of P_{abs} . This approximation is justified by the fact that microwave discharges are very efficient in general. Rogers¹³ measured the power absorbed by an Argon plasma column positioned along the axis of a microwave cylindrical resonant cavity similar to the one used in this thesis. The experimental conditions were as follows; the resonant mode was the TM_{012} , the tube radius was 13mm, the discharge pressure ranged between 0.01 and 1 Torr and the electron density was between 10^{11} cm^{-3} to 10^{12} cm^{-3} . He found that the microwave coupling efficiency

defined as

$$E_{\text{effic}} = \frac{\text{Power absorbed by the discharge}}{\text{Power stored in the cavity}}$$

varies from 85% to 98%. The highest efficiency corresponds to the higher pressure range which is where he measured the largest electron density. He also found that the largest tube size had the best coupling efficiency.

In our case, the cavity is excited with the TE_{211} mode and the plasma is disk shaped. The electron density measured ranges between $8 \times 10^{10} \text{ cm}^{-3}$ and $6 \times 10^{11} \text{ cm}^{-3}$. This comparison seems to indicate that the assumption of a high coupling efficiency is reasonable for the purpose of this simple model. A further investigation of the coupling efficiency for the particular geometry used in this thesis is necessary for more accurate calculations.

The other assumption made here, is that N_0 is considered to be equal to the plasma density measured in the lower region of the discharge.

Using the calculated value for ν_e we can determine E from equation (6.4). The results obtained from these calculations are displayed in Figure 6.2 where E is plotted versus the product of the discharge pressure p and the diffusion length Λ . These calculations correspond to an argon discharge in applicator I with a constant input microwave power of 100 W and three diffusion length 0.43 cm, 0.79 cm and 1.22 cm. In Figure 6.3, $E/p \cdot \Lambda$ is plotted against $p \cdot \Lambda$.

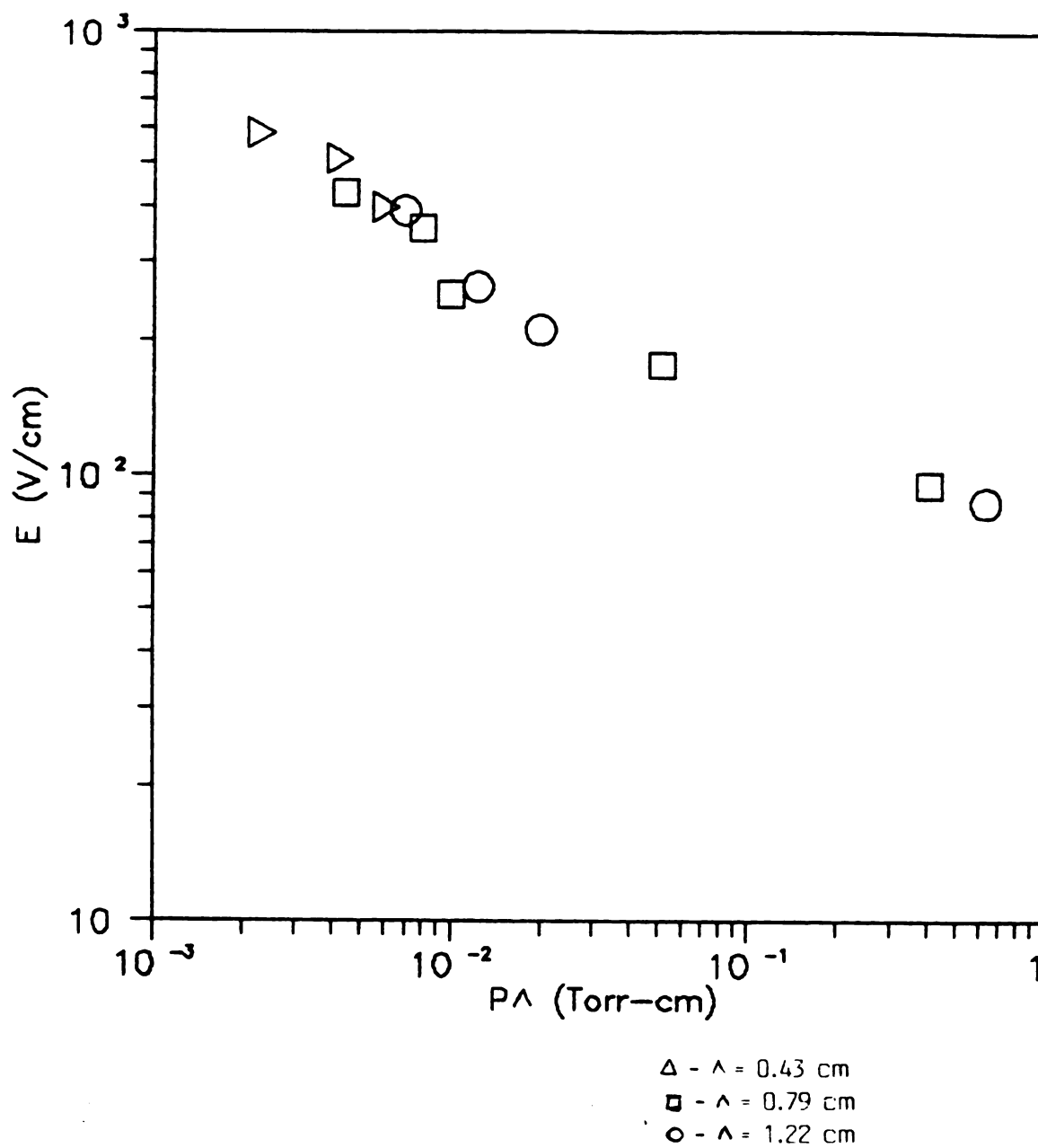
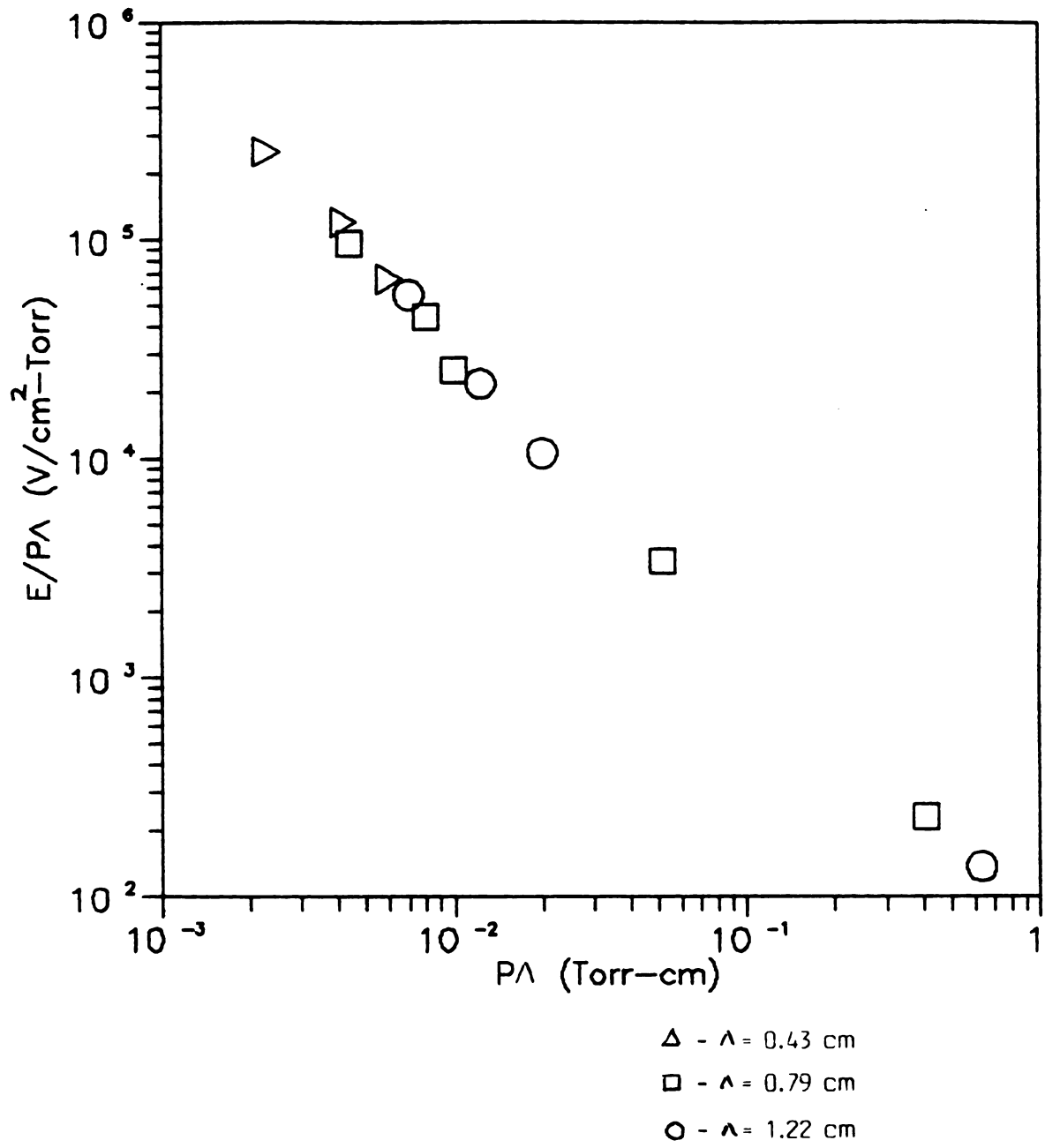


Figure 6.2 Calculated Average Electric Field Versus Discharge Pressure Diffusion Length Product

Figure 6.3 Calculated $E/p\Lambda$ Versus $P\Lambda$

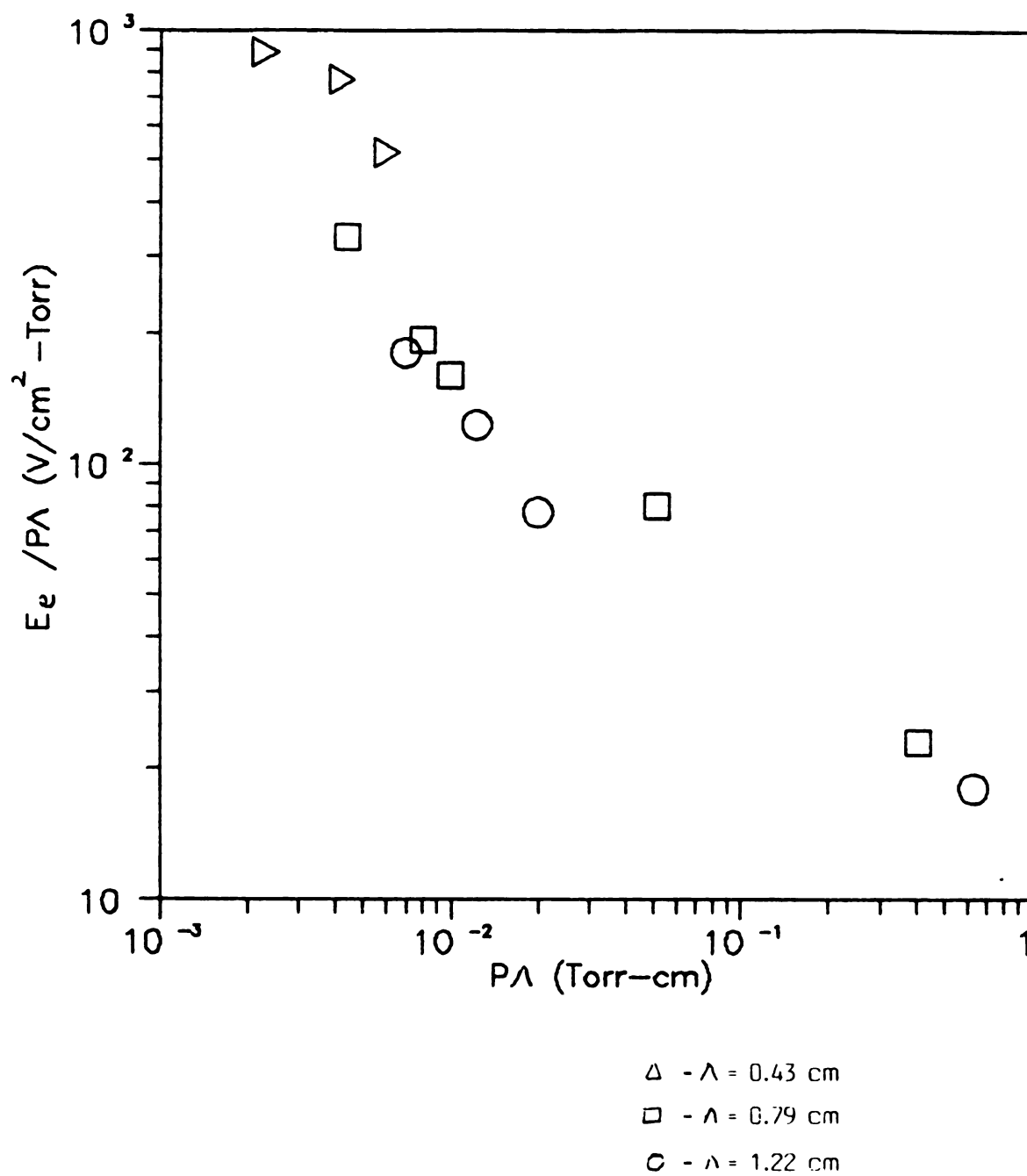


Figure 6.4 Calculated Average Effective Electric Field

The average effective electric field E_e is defined as

$$E_e^2 = \frac{E^2 \nu_e^2}{2(\nu_e^2 + \omega^2)} \quad (6.5)$$

It represents the effective value of the electric field for a microwave discharge. This effective field term is comparable to the electric field of a DC discharge. Note that the term

$$P_e = \frac{e^2}{m_e \nu_e} \frac{E^2 \nu_e^2}{2(\nu_e^2 + \omega^2)}$$

represents the average power density transferred to the electrons from the electric field between two collisions. This power is proportional to E_e^2 . E_e is calculated for the measured experimental conditions, and plotted as $E_e/p \Delta$ versus $p \Delta$ in Figure 6.4.

6.4 ION MOBILITY.

Knowing the average electric field E , the ion mobility can be calculated from equation (3.104). It should be noted that equation (3.104) was derived empirically for a DC argon discharge⁵⁰ and that an equivalent expression for an RF discharge was not available. The effect of an RF field can be included in equation (3.104) provided the electric field in the equation is replaced by the effective electric field described earlier. The results for the calculated ion

mobility are plotted against the discharge pressure p for argon in Figure 6.5. For a comparison, this figure includes two curves, curve 1 represents the ion mobility without E field correction, curve 2 includes the average effective electric field correction.

6.5 ELECTRON TEMPERATURE

We have seen, in Chapter 3 that the electron temperature is independent of the plasma density, but varies with the product $Cp \Lambda$. An expression for C was obtained in Chapter 3 equation (3.92)

$$C^2 = \frac{4e\sqrt{2}}{\sqrt{\pi m_e}} \frac{a_i \sqrt{\epsilon_i}}{N_n \mu_i} \frac{1}{(kT_n)^2} \quad (6.6)$$

where a_i is the slope of ionization cross section versus electron energy curve described in Chapter 3, ϵ_i is the ionization threshold energy, N_n and T_n are the neutral particles density and temperature respectively. In all experimental measurements the measured value for the gas temperature was found to vary from approximately 400 $^{\circ}\text{K}$ to 480 $^{\circ}\text{K}$.

The results of the theoretical calculations for kT_e / ϵ_i versus $Cp \Lambda$ using equation (6.6) are shown in Figure 6.6 (solid curve). In Figure 6.6, the results from the experimental measurements using the ion mobility corrected with the effective electric field, are compared to the

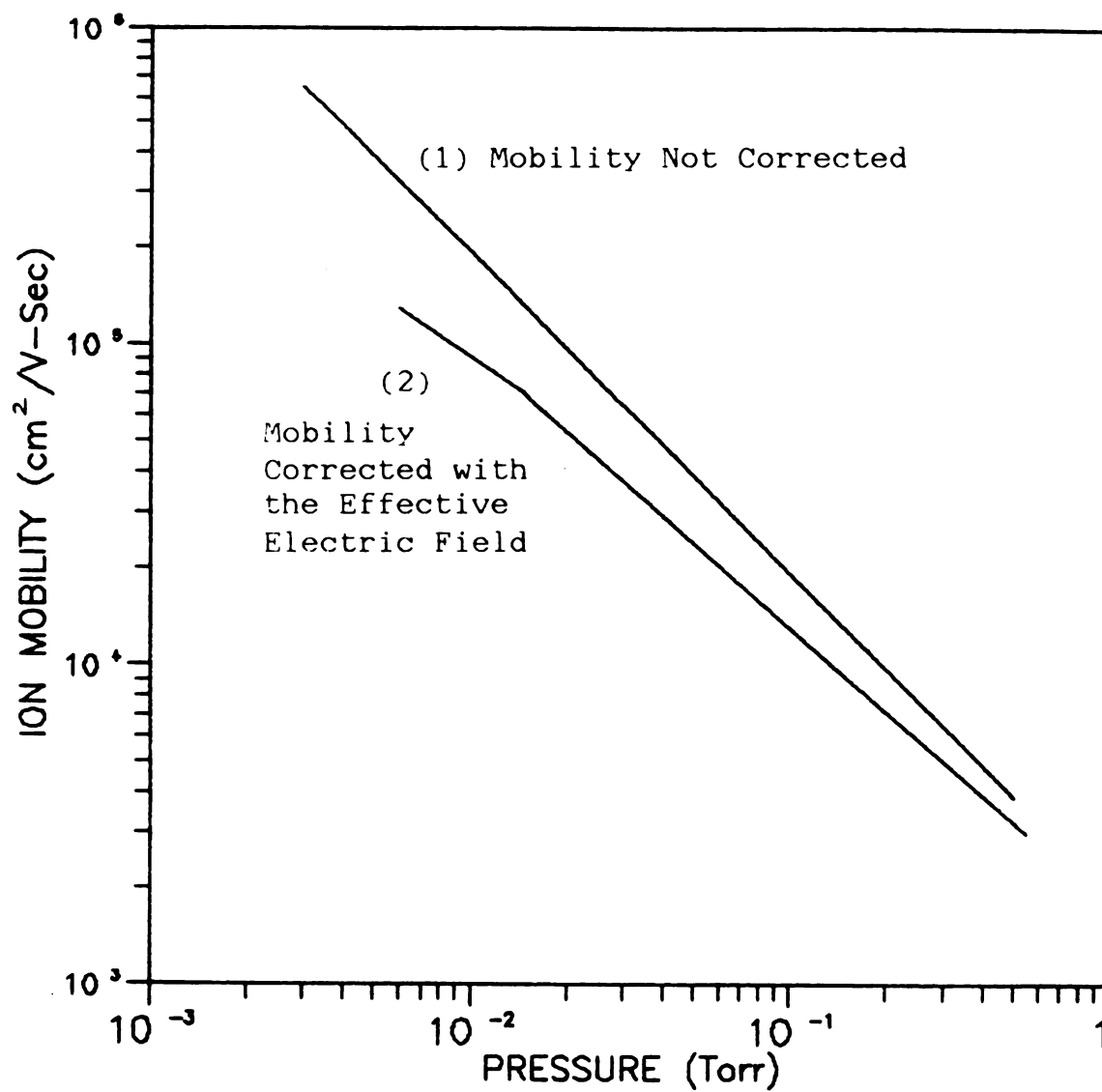


Figure 6.5 Calculated Ion Mobility

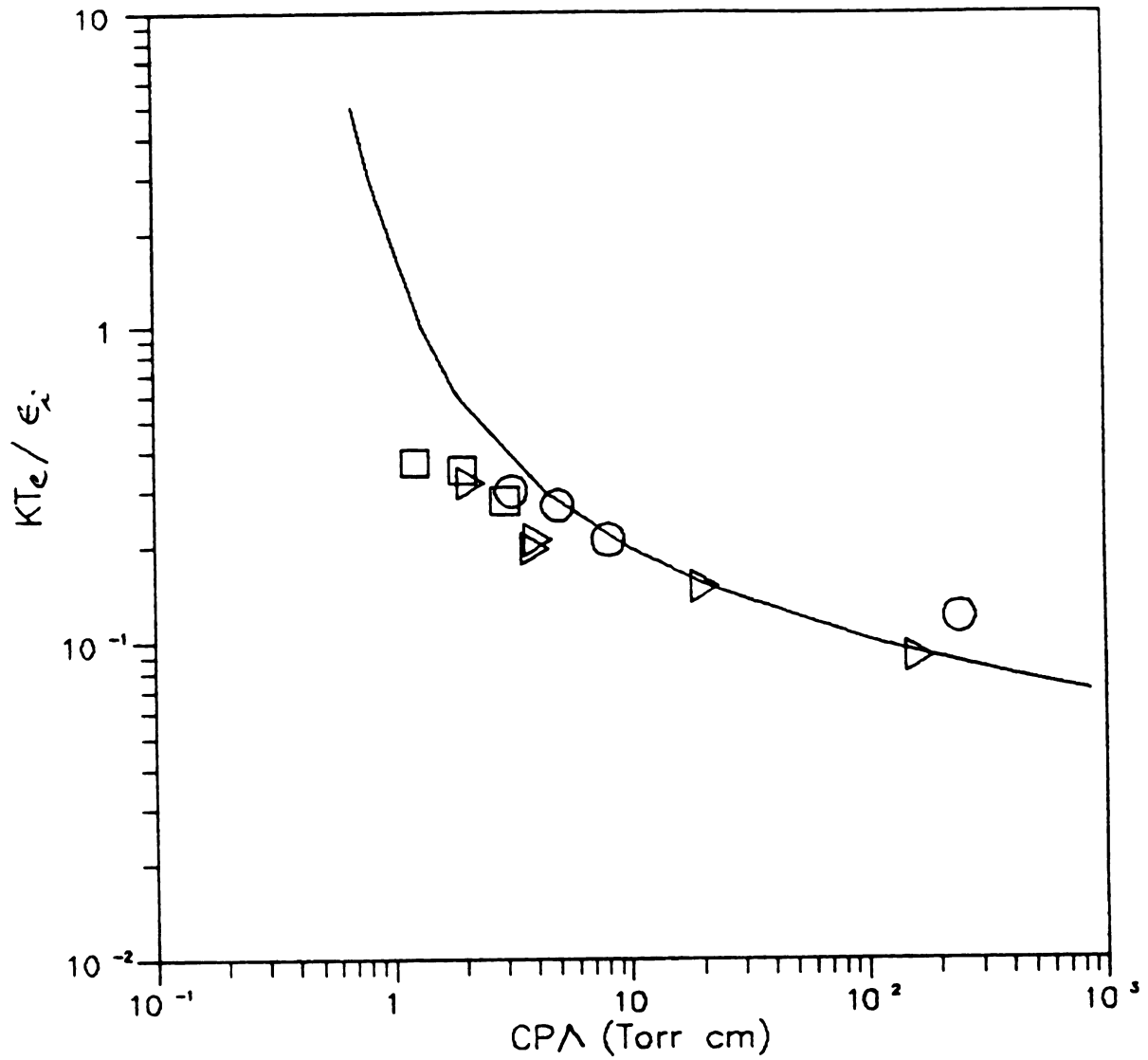


Figure 6.6 Comparison Between Experimental Measurements and Theoretical calculations of the Electron Temperature

theoretical curve. The experimental data correspond to an argon discharge in applicator I for a constant microwave input power of 100 W and three diffusion lengths 0.43 cm, 0.79 cm and 1.22 cm. The constant a_i and μ_i were calculated from published data for the ionization cross section for argon gas⁴⁹. Note that the experimental results of the electron temperature measurements are in fairly good agreement with the predictions of this simple model for the higher pressure range. In the low pressure region however, the experimental data do not match with the theoretical curve. This can be interpreted as the domain of transition from ambipolar to free fall diffusion⁴⁸.

6.6 ION CURRENT AVAILABLE FOR BEAM EXTRACTION

An expression for the ion current available for beam extraction can be derived from equation (3.100) in Chapter 3. In this case however the ion flux has to be integrated over the total area of the extraction apertures of the extraction grids. Since these extraction holes are distributed over a circular area defined as the grid extraction area (see Figure 4.16), the ion flux has to be integrated over this extraction area and then multiplied by the geometric transparency of the extraction grid in order to obtain the ion current falling on the extraction holes

area. The expression for this ion current is

$$I_{ex} = 2 \pi^2 k T_e \frac{N_0}{L} \mu_i \int_0^{R_{ex}} J_0\left(2.405 \frac{r}{R}\right) r dr \quad (6.7)$$

where R_{ex} is the extraction area radius, R is the discharge chamber radius and L is the discharge chamber height.

Using the identity

$$\frac{d J_n(x)}{dx} = J_{n-1}(x) - \frac{n}{x} J_n(x)$$

and integrating by parts, I_{ex} becomes

$$I_{ex} = 2\pi^2 k T_e \mu_i \frac{N_0 R^2}{2.405 L} J_1\left(2.405 \frac{R_{ex}}{R}\right) \left(\frac{R_{ex}}{R}\right) T_{GE} \quad (6.8)$$

where μ_i is the ion mobility, k is the Boltzmann constant, T_e is the electron temperature, N_0 is the ion density at the center of the discharge and T_{GE} is the grid geometric transparency.

For the case of the double grids the extraction area has a radius of 1.25 cm and a geometric transparency of 77%. the results of the calculated ion current available for extraction obtained for the case of the ECR applicator (when the magnets were removed) with the 4.0 cm quartz disk and an input power of 200 W, are shown in Figure 6.7. This figure displays the results of the calculated ion current available for extraction for the case where the ion mobility is corrected with the effective electric term. Figure 6.7 also includes the measured ion beam currents obtained with the double grids using the ECR applicator with the 4.0 cm quartz

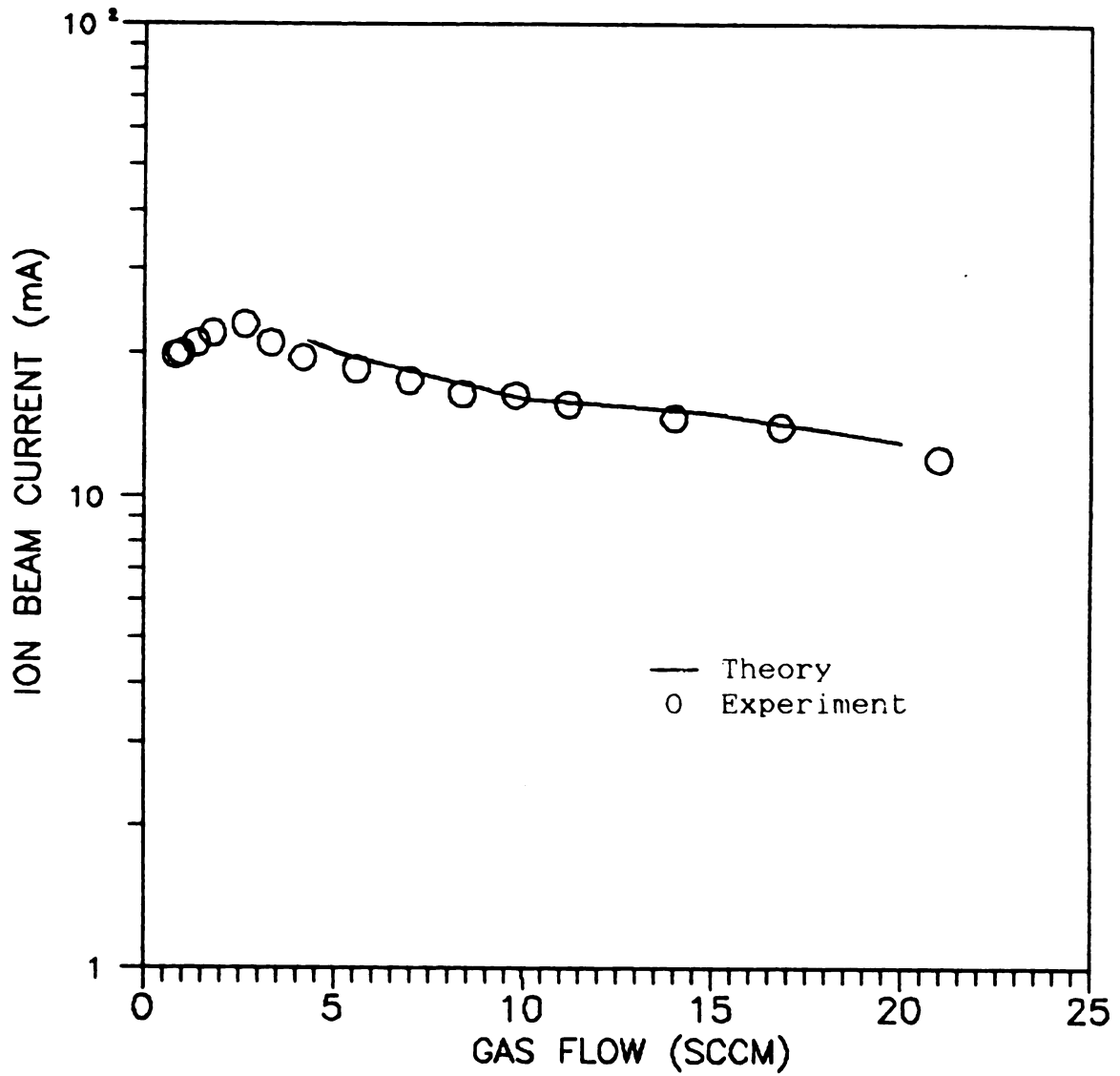


Figure 6.7 Comparison Between Experimental Measurements and Theoretical Calculations of Extracted Ion Beam Currents

disk and an input microwave power of 200 W. In this experiment the argon flow rate was varied from 0.85 sccm to 22 sccm corresponding to a discharge pressure variation of 5×10^{-4} Torr to 1.5×10^{-2} Torr. The theoretical curves were obtained by using the previously measured values for the electron density and the electron temperature corresponding to each data point.

Figure 6.7 shows that the calculated ion current available for extraction corresponds almost exactly to the experimental measurements when the ion mobility term is corrected with the calculated average effective electric field. It should be reminded that in the theoretical calculations, measured values for the electron density and electron temperature were used. These measurements could not be performed when the ion beam was being extracted, however they were performed under similar gas flow conditions. This method of measuring the electron density and electron temperature could induce some errors since the ion beam extraction can result in a discharge pressure drop due to this forced ion extraction. This uncertainty in the discharge pressure evaluation could be resolved by measuring directly the discharge pressure with a transducer located in the discharge chamber.

CHAPTER VII

SUMMARY AND CONCLUSIONS

7.1 INTRODUCTION

In the experiments described in this dissertation, three microwave applicators were successfully tested as plasma and ion sources. All three applicators were capable of producing high density plasmas, with densities in excess of $5 \times 10^{11} \text{ cm}^{-3}$ at discharge pressures of less than 5×10^{-3} Torr. Applicator I and applicator I retrofitted with rare earth magnets were tested as ion sources and yielded ion beam currents that were comparable to other RF and microwave ion sources in the literature^{36,37,38,39,40}. The ECR applicator was also tested as an ion and plasma source. The extracted ion beam currents obtained with the ECR applicator did not show any substantial improvements in extracted ion beam current and power cost over the performances of the first two applicators. However, the new ECR applicator design allowed easy operation as a plasma and ion source at very low discharge pressures and gas flow rates. For example. An ion beam was extracted with argon gas flow rates as low as 0.84 sccm under very stable plasma

co

wa

7.

TH

ap

ex

ex

Th

be

pr

si

wi

va

fr

is

si

gr

Wit

App

100

4.1

conditions. The discharge pressure at these low flow rates was calculated to be approximately 3×10^{-4} Torr.

7.2 COMPARISON BETWEEN THE THREE APPLICATORS TESTED IN THIS THESIS

The performance and figures of merit of the three applicators tested are summarized in Table 7.1. The experimental data displayed in Table 7.1 was taken at an excitation frequency of 2.45 GHz for argon gas discharges. The results are shown for different discharge conditions because each applicator had a different low discharge pressure limitation. Applicator I was tested with both single and double grids and the ECR applicator was tested with only the double grids. The input microwave power varied from 150 W to 350 W and the extraction voltage varied from 1400 V to 1600 V. Note that the grid extraction area is different for the single and double grid systems, The single grid has a 24 cm^2 extraction area while the double grid has a 5 cm^2 extraction area.

Applicator I and Applicator I retrofitted were tested with the single grid, for the same discharge conditions. Applicator I retrofitted produced the highest ion current of 100 mA corresponding to a beam current density of 4.17 mA/cm^2 with a power cost of 1500 W per beam Amp.

Table 7.1 Comparison of the Three Ion Sources Tested in this Thesis

GRIDS	FREQUENCY	DISCHARGE	FLOW	POWER	GRID	EXTRACTION	BEAM	BEAM	POWER	MASS
	GHZ	PRESSURE	SCCM	WATTS	EXTRACTION	VOLTAGE	CURRENT	CURRENT	COST	UTILIZATION
		mTORR			AREA	kV	mA	DENSITY	W/A	%
					cm ²			mA/cm ²		
APPLICATOR	SINGLE	7	20	150	24	1.4	72	3.0	2000	5
I	DOUBLE	1	2	240	5	1.6	29	5.8	8300	20
APPLICATOR	SINGLE	7	20	150	24	1.6	100	4.17	1500	7
I	RETROFITED									
E.C.R.	DOUBLE	1.0	2	250	5	1.6	30	6	8300	21
APPLICATOR	DOUBLE	0.3	0.84	350	5	1.5	20	4	1700	34

When the double grids were used the ECR applicator produced a slightly higher beam than applicator I at the same power cost of 8300 W/A. A maximum mass utilization efficiency of 34% was obtained with the ECR applicator at the very low gas flow rate of 0.84 sccm. However, the corresponding power cost was a relatively high 17,000 W/A.

Higher currents could be extracted with applicator I and applicator I retrofitted but when the gas flow was reduced below 10 sccm the plasma became very instable for beam extraction applications. Low gas flow discharges could be obtained with these two applicators but only for experimental purposes. The discharge was too unstable to allow these applicators to be used in low pressure ($<1 \times 10^{-3}$ Torr) commercial applications. On the other hand, the ECR applicator produces very stable discharges and ion beams at very low pressures and flow rates. Also, the ECR applicator resulted in a plasma and ion source that is very easy to use and operate. It can be ignited by just switching the microwave power on when the cavity is pretuned to the right resonant mode. Thus the use of a Tesla coil became unnecessary for igniting the plasma.

Note that for all the applicators tested in Table 7.1, the beam current and the mass utilization could be improved simply by making the grid extraction area larger. For example, this grid extraction area could be made as large as 69 cm^2 if the extraction apertures were to fill the entire lower end of the discharge chamber. Assuming a uniform ion

beam such a grid system would be able to extract an ion beam of approximately 300 mA with the same applicator design, this would reduce the power cost to 800 W/A. These calculations are only an approximation since the beam would not really be uniform over the larger extraction grids and the larger opening of the extraction grids would have an effect on the operating discharge pressure. However, they do demonstrate the potential for significant improved performance by redesign.

7.3 COMPARISON OF THE THREE APPLICATORS AND OTHER RF AND MICROWAVE ION SOURCES

A comparison of the microwave ion source performance described in this thesis and other RF and microwave ion sources can be made by referring to tables 7.1 and 2.1.

A comparison of different ion sources is in general difficult to achieve since each ion source is designed for a specific purpose. Some ion sources are designed for low energy ion beams while others are designed for extracting high ion beam currents. In addition different ion sources have different grid types and sizes, varying discharge chamber sizes, different ion beam extraction voltages, etc.

In the experiments described in this thesis, an objective was to obtain a high ion beam current density at moderate extraction voltages (<2000 eV). Grid sets that had

an extraction diameter much smaller than the 9.4 cm diameter of the discharge were used. Thus this is an inefficient ion source design. Any comparison should keep this fact in mind. However, a comparison based on the ion beam current density can be made. Data in Tables 2.1 and 7.1 indicate that microwave ion sources are capable of high ion current densities. Our ECR applicator yield a maximum ion current density of 6 mA/cm^2 which is comparable to the results of Sakudo's 7 mA/cm^2 obtained with an extraction voltage of 7000 V and a power cost of 4200 W/A, our results were obtained with an extraction voltage of 1600 V and a power cost of 8300 W/A. The other ion sources had lower ion beam current densities, Nakanishi produced an ion beam density of 2 mA/cm^2 with a power cost as low as 750 W/A.

As far as the mass utilization efficiency is concerned the results of 34% obtained with our ECR ion source are comparable to the results obtained by the RIT 10 ion source and by Nakanishi but our power cost was considerably higher. Thus the ion source concept demonstrated in this thesis compares favorably with other designs and since the experimental work reported here must be considered to be exploratory, it is expected that further improvements in performance with this concept can be made. In particular, keeping the discharge diameter constant at 9.4 cm and increasing the grid extraction diameter should greatly improve the power cost efficiency.

7.4 CONCLUSIONS

The theoretical modeling and the measurements of discharge properties yielded important understanding of the microwave discharges. The measured electron densities, electron temperatures and input powers were combined with the effective electric field calculations and an ambipolar diffusion model of the discharge. These measurements indicated that the electron temperature followed the classical C_p curve developed for the DC positive column discharges except at very low pressures where the transition from ambipolar to free fall diffusion is expected to become important. The effective electric field was used to calculate the ion mobility as a function of pressure. These mobility calculations were then combined with the ambipolar diffusion model to yield the flux of electrons and ions impinging on the extraction grids. This flux is a function of the electron density, the electron temperature, the effective electric field and the pressure. Taking into account the grids transparency the calculated ion current density impinging on the grids extraction area agreed very well with the measured extracted ion beam current densities under the same experimental conditions. This agreement between theory and experiment provided better insights and understanding of low pressure microwave discharges. It is

expected that this understanding could be used to design more efficient microwave ion sources. This modeling effort and experimental measurements represent a good reference point to further improve and refine theoretical modeling of microwave discharges.

7.5 FURTHER RESEARCH

The work described in this thesis could be considered as a preliminary ground for further improvements and developments of this type of microwave ion source. The improvements needed are in the following areas;

a) Concepts improvements

i) Ion extraction system. The present double grids

were limited by ion beam impingement of the accelerator grid. Extraction grids should be specifically designed for these microwave ion sources.

ii) The effect of varying the discharge size should be further investigated.

- iii) Improve the magnetic confinement and production of ion with ECR by finding an optimum static magnetic field configuration.
- b) Theory improvements. The theory developed in this thesis makes use of a number of approximations. This model should be improved by relaxing these approximations.
- c) Further experiments should include
- i) Testing of different extraction grid systems, specifically, larger extraction area.
 - ii) A spectroscopic study of these microwave discharges should be made to acquire a better understanding of the discharge chemistry.
 - iii) Measurement of the ion beam profile and uniformity.

APPENDIX

APPENDIX A

STATIC MAGNETIC FIELD MAPPING

INTRODUCTION.

For the ECR applicator, knowledge of the multicusp static magnetic field pattern was necessary in order to insure that charged particles near the grid extraction area were exposed to a minimum B field region. The use of a Hall-effect magnetic field probe alone would not be sufficiently accurate because of the high curvatures of the magnetic field lines around the cusps. A method for recording detailed permanent maps of the static magnetic fields in the discharge region was used. Once the field pattern was known, it was easier to use a magnetic field probe to measure the fields strength throughout the discharge region.

DESCRIPTION OF THE METHOD

The method utilized to map the static magnetic field pattern in the discharge region used iron filings suspended in an acrylic cement between two plexiglas plates. It was

found that common #20 iron filings were the most suitable to obtain a clear picture of the fields. The cement used was "Weld-on 40" produced by the Industrial Polychemical Services Corporation of Gardena California. The application of the method was somewhat complicated by the strength and gradient of the samarium-cobalt magnets because the iron filings positioned in the immediate proximity of the magnets tend to respond to the magnetic attraction much faster than the iron filings positioned further toward the center of the discharge region. After a period of experimentation, field maps of reasonable resolution were obtained.

The final process involving a number of steps is described as follows:

- 1) Cut two identical pieces of plexiglas to fit into the plane of the discharge region to be mapped.

- 2) Mix the Weld-on 40 cement with the hardener component with a volume ratio of 20-to-1, stirring slowly to avoid the formation of air bubbles. Use a wax cup.

- 3) Wait 10 minutes for the cement to thicken.

- 4) Spread the cement mix on one of the two plexiglas plates. The thickness of the cement should be approximately 50% larger at the center of the plate than around the edges to allow more mobility for the iron filings that will be located in the center of the discharge region relatively far from the magnets.

- 5) Evenly spread iron filings over the cement covered plate. It was found that a shaker-dispenser was the most

effective. This must be done promptly, as host of problems can arise if a dry skin forms on the cement.

6) Quickly put the other plexiglas plate on top of the filings.

7) Remove air pockets and irregularities by applying pressure to the top plate.

8) Wait several minutes for the cement to set. This time is variable, depending on the fields strength, room temperature, etc. This prevents a very fluid cement from allowing too much iron filing migration near the plates edges.

9) Set the plates in the fields in question.

10) Very quickly remove the plates from the fields region. Leaving them too long will result in an uneven iron filing migration toward the magnets.

11) Wait several minutes for the cement to harden around the plates edges.

12) Reset the plates in exactly the same position as in step (9) to allow the iron filings in the center of the plates to respond to the weaker fields. This time the plates can be left longer in this position since the iron filings near the edges are practically unaffected in the hard cement.

13) When a clear pattern of the field maps is visible and satisfactory, remove the plates and allow the cement to cure in a magnetic field free environment.

Finally the the cemented plexiglas plates holding the magnetic field maps can be photocopied for a permanent record.

LIST OF REFERENCES

LIST OF REFERENCES

1. J. Asmussen and J. Root, Appl. Phys. Lett. 44, 396 (1984)
2. J. Asmussen and J. Root, "Ion Generation Apparatus and Method for the Use of", U.S. Patent No. 4 507 588, Mar. 26, (1985)
3. J. Root and J. Asmussen, Rev. Sci. Instrum. 56, 154 (1985)
4. J. Asmussen and M. Dahimene, J. Vac. Sci. Tech. B4, Jan/Feb (1987)
5. T. Roppel, D.K. Reinhard and J. Asmussen, J. Vac. Sci. Tech. B4, Jan/Feb (1986)
6. J. Hopwood, M. Dahimene, D.K Reinhard and J. Asmussen, "Plasma Etching with a Microwave Cavity Plasma Disk Source," Presented at the 31st International Symposium on Electron, Ion and Photon Beams, May (1987) CA
7. M. Dahimene and J. Asmussen, J. Vac. Sci. Tech. B4, Jan/Feb (1986)
8. J. Asmussen and M. Dahimene, "The Experimental Test of a Microwave Ion Source", Presented at the 30th International Symposium on Electron, Ion and Photon Beams, May (1986), Boston MA.
9. M. Dahimene, J. Root, L. Mahoney and J. Asmussen, "Characterization of a Microwave Generated Plasma" IEEE International Conference on Plasma Science, May (1986), Saskatoon, Canada.
10. M. Dahimene, L. Mahoney and J. Asmussen, "An Electron Cyclotron Resonance Multicusp Magnetic Field Microwave Plasma Source for Electric Propulsion", Presented at the 19th AIAA/DGLR/JSASS International Electric Propulsion Conference, Colorado, May (1987)

11. R. Fredericks, "An Experimental and Theoretical Study of a Resonantly Sustained Plasma in Microwave Cavities," Ph.D. Dissertation, Michigan State University, (1971)
12. R. Mallavarpu, "An Investigation of the Electromagnetic Behavior of a Microwave Plasma Source Over a Wide Range of Pressures and Flow Rates," Ph.D. Dissertation, Michigan State University, (1976)
13. J. Rogers, "Properties of Steady-State, High Pressure Argon Discharges," Ph.D. Dissertation, Michigan State University, (1982)
14. S. Whitehair, "Experimental Development of a Microwave Electrothermal Thruster," Ph.D. Dissertation, Michigan State University, (1986)
15. H.R. Kaufman, J.J. Cuomo and J.M.E. Harper, J. Vac. Sci. Techn., 21, 3, (1982).
16. H.R. Kaufman, NASA Tech. Note TND-585, Jan. (1961).
17. H.R. Kaufman and R.S. Robinson, AIAA. J. 20, 245, (1976).
18. R.S. Robinson, J. Vac. Sci. Techn. 15, 277, (1978).
19. H.R. Kaufman, J.M.E. Harper, and J.J. Cuomo, Patent Application.
20. R.C. Knechtli, G.R. Brewer, M.R. Currie, "Plasma Physics in Theory and Application", Edited by W.B. Kunkel, McGraw-Hill, NY. (1966).
21. E.R. Harrison, J. Electron. Control. 5, 319, (1958).
22. J. Taillet, Am. J. Phys., 37, 423, (1969).
23. R. Geller, C. R. Acad. Sc., Paris, 249, 2749 (1959).
24. A.J. Hatch, Proc. Fourth. Inter. Conf. on Ionization Phenomena in Gases, Uppsala, (North-Holland Publ. Co, Amsterdam) Vol. I, p. 314, (1959).
25. P.E. Vandenplas, "Electron Waves and Resonances in Bounded Plasmas", J. Wiley, NY, (1968).
26. B. Chapman, "Glow Discharge Processes", J. Wiley, NY, (1980).

27. A.D. MacDonald and S.J. Tetenbaum, "Gaseous Electronics", J. Wiley, vol 1. (1960).
28. H.U. Eckert, High Temperature Science, 6, 99, (1974).
29. M.I. Boulos, Pure and Applied Chemistry, Vol 57, No. 9, 1321, (1985).
30. M. Moisan, C. Beaudry, and P. Leprince, IEEE Trans. Plasma Sci., PS-3, Vol. 55, (1975).
31. M. Moisan, C. Beaudry, L. Bertrand, E. Bloyet, J. M. Gagne, P. Leprince, J. Marec, G. Mitchell, A. Ricard, and Z. Zakrzewski, IEEE. Cont. Pub. Vol. 143, p. 382, (1976).
32. A. Trivelpiece, and R. Gould, J. Appl. Phys. Vol 30, p. 1784, (1959).
33. J. Rogers, and J. Asmussen, IEEE. Trans. Plasma. Sci. Vol. PS-10, No 1, (1982).
34. J. Asmussen, R. Mallavarpu J. Hamann, and C. Park, Proc. IEEE, 62(1), 109-107, (1974).
35. M. Miyamura, O. Tsukakoshi, and S. Komiya, J. Vac. Sci. Technol., 20(4), April (1982).
36. K. Tokiguchi, N. Sakudo, and H. Koike, Rev. Sci. Instrum. 57(8), August (1986).
37. C. Leleune, J.P. Grandchamp, O. Kessi and J.P. Gilles, International Conference on Low Energy Ion Beams-4, April (1986), Brighton, G.B.
38. K.H. Groh, H.W. Loeb and H.W. Velten, "Performance Data Comparison of the Inert Gas RIT 10.", AIAA/JSASS/DGLR 16th International Propulsion Conference, (1982).
39. S. Nakanishi, "Parallel Plate Radiofrequency Ion Thruster.", NASA Report, (1983).
40. R.Q. Lee and S. Nakanishi, "Recent Work on an RF Ion Thruster.", Nasa Report, (1982).
41. R. Lossy and J. Engemann, "RF-Broad-Beam Ion Source for Reactive Sputtering", Universitet Wuppertal, West Germany.

42. B.E. Cherrington, "Gaseous Electronics and Gas Lasers" Pergamon Press, (1980).
43. G.Ecker, O. Zoller, Phys. Fluids, 7, 1996, (1964).
44. Y.M. Kagan, R.I. Lyagushchenko, Sov. Phys. Tech. Phys., 9, 1445, (1965).
45. A.V. Eletskaa, B.M. Smirnov, Sov. Phys. Tech. Phys., 15, 1308, (1971).
46. H.J. Oskam and V.R. Mitteltadt, Phys. Rev., 132, 1435 (1963).
47. Yu.M. Kagan, R.L. Lyagushchenko, Sov. Phys. Tech. Phys. Vol.7, No.2, pp.134, (1962).
48. R.A. Gerber and J.B. Gerardo, Phys. Rev. A, Vol.7, No.2 pp741 (1973).
49. E.W. McDaniel, "Collision Phenomena in Ionized Gases", J. Wiley , N.Y, (1964).
50. L.S. Frost, Phys. Rev., 105, 354, (1957).
51. L. Vriens, J. Appl. Phys., Vol 44, 3980, (1973).
52. L. Vriens, J. Appl. Phys., Vol.45, 1191, (1974).
53. S. Whitehair, J. Asmussen, AIAA. Journal of Propulsion and Power, Vol 3, No 2, (1987).
54. J. Asmussen, H. Lin, B. Manring, R. Fritz, Rev. Sci. Instrum., To be published
55. S.C. Brown, "Introduction to Electrical Discharges in Gases", J. Wiley, (1966).
56. V. Atta, "Vacuum Science and Engineering", Mc Graw-Hill, (1965).
57. E.O. Johnson and L. Malter, Physical Review, Vol. 80, No. 1, (1950).
58. W. Lochte-Holtgreven, "Plasma Diagnostics", North Holland, pub. Amsterdam, (1968).

59. G. Aston, H. R. Kaufman and P. J. Wilbur, AIAA Journal, Vol. 16, No. 5, (1978).
60. G. Aston and H. R. Kaufman, AIAA Journal, Vol. 17 No. 1, (1979).
61. H.R. Kaufman, AIAA Journal, Vol. 15, No. 7, (1977).
62. G. R. Nudd and K. Amboss, AIAA Journal, Vol. 8, No. 4, (1970).
63. T. Roppel, "Anodic Oxidation of Silicon in a Microwave Plasma Disk Reactor", Ph.D. Dissertation, Michigan State University, (1986).

MICHIGAN STATE UNIVERSITY LIBRARIES



3 1293 10730 0224